Investigation of Recrystallization via *in-situ* Electrical Resistivity Measurements

Investigation of Recrystallization via *in-situ* Electrical Resistivity Measurements

By

Sanjay Kumar Vajpai

(B.Eng., M.Tech.)

A Thesis
Submitted to the School of Graduate Studies
in Partial Fulfillment of the Requirements
for the Degree of
Master of Applied Science

McMaster University

MASTER OF APPLIED SCIENCE (2006) McMaster University

(Materials Science & Engineering) Hamilton, Ontario

TITLE Investigation of Recrystallization via *in-situ* Electrical Resistivity Measurements

AUTHOR Sanjay Kumar Vajpai.

B.Eng., Metallurgical Engineering, Indian Institute of Technology Roorkee, Roorkee, INDIA, 1998.

M.Tech., Materials and Metallurgical Engineering, Indian Institute of Technology Kanpur, Kanpur, INDIA, 2003.

SUPERVISOR Dr. Dmitri V. Malakhov

NUMBER OF PAGES: xii, 117

ABSTRACT

Recrystallization of aluminum alloys, which affects their mechanical properties, was examined by a variety of experimental techniques with electrical resistivity (ER) measurements being one of them. In this work, a new method based on *in-situ* electrical resistivity measurements has been originated and employed for characterization of recrystallization. In contrast to traditional method of resistivity measurements at either room or liquid N_2 temperature on isothermally/isochronally heat-treated samples, a new and simpler approach was proposed. In this work, resistivity of a long sample with a small cross section area (usually, $70\times2\times0.2\,mm^3$ strips were employed) was continuously measured while the sample was heated from room temperature to 400°C. In this case, there are several independent contributions to electrical resistivity including contributions from lattice vibrations, second-phase particles, presence of solutes and defects, etc.

In order to separate precipitation and recrystallization, a new annealing cycle was proposed through thermodynamic modeling. It was demonstrated that for 5xxx Al alloys only contributions from phonons, ρ_T, and dislocations, ρ_d, were important. By analyzing a temperature dependence of ρ, it was intended to separate the effect related to a dislocation density, i.e. to a degree of recrystallization. Since $\rho_T \gg \rho_d$, this effect is elusive. It can only be detected if a robust numerical differentiation is utilized. A novel spline-based method of robust numerical differentiation was developed and employed to reveal these elusive effects from $\rho(T)$ (or $R(T)$) profiles. It was shown that a

characteristic peak of the $d\rho(T)/dT$ curves points to onset and end of "events" taking place in Al alloys and that peaks' positions depend on the degree of deformation and amount of alloying additions such as Fe and Mn. The onset and extent of recrystallization seen in the resistivity measurement experiments were confirmed by optical metallography and hardness measurements. Uniformity of deformation in samples was investigated by micro-hardness measurements followed by a detailed statistical analysis to prove that deformation is uniform throughout cross-section of the materials.

Results suggested that increasing degree of deformation and alloying additions (Fe and Mn) lower the temperature of onset of recrystallization. In addition, it was observed that kinetics of recrystallization was accelerated by the increasing degree of deformation and alloying additions whereas recrystallized grain size decreases with increasing additions of Fe and Mn in Al-3% Mg alloys.

ACKNOWLEDGEMENT

I would take this opportunity to thank Dr. Dmitri V. Malakhov, my supervisor, whose untiring efforts were instrumental in timely completion of this work. It was a great privilege to get an opportunity to work with such a wonderful academician.

I would like to express deep sense of gratitude to Dr. Marek Niewczas for providing all kind of support and facilities to carry out resistivity measurement experiments. Since electrical resistivity measurement is the essence of this work, it would not have been possible to accomplish this task without his guidance.

A special note of thanks to all MSE technical staff and Mr. Chris Butcher for sharing the knowledge and extending their help to carry out experimental activities efficiently. I would also like to thank my colleagues Basab, Rubaiyat, Thevika, Mohammad, Mehdi, and Florent for all their support and companionship.

The financial support of CAMM and McMaster University is gratefully acknowledged.

Last but not the least, I convey my deep regards to my Parents and extend special thanks to my wife Anamika and my son Swarnim. Their unconditional love and support has always been a source of inspiration.

TABLE OF CONTENTS

ABSTRACT.....iii

ACKNOWLEDGEMENTS..... v

TABLE OF CONTENTS.....vi

LIST OF FIGURES..... viii

LIST OF TABLES..... xii

CHAPTER 1 INTRODUCTION.....1

CHAPTER 2. Metallurgy of 5xxx Aluminum alloys and their usage in automotive industry.....5

CHAPTER 3. Recrystallization and related phenomena.....17

CHAPTER 4. Experimental strategies and their basis.....30

4.1 Thermodynamic modeling of the Al-Mg-Mn-Fe system.....31

4.2 Uniformity of deformation.....36

4.3 Electrical resistivity measurements.....43

CHAPTER 5. Spline filtering.....53

CHAPTER 6. R-data and their interpretation.....75

CHAPTER 7. Results and discussion.....84

7.1 Analysis of resistivity measurements for 95% deformed Al-3%Mg alloy.....84

7.2 Analysis of resistivity measurements for 75% deformed Al-3%Mg alloy.....90

7.3 Analysis of resistivity measurements for 95% deformed Al-Mg-Fe-Mn (I5) alloy...95

7.4 Analysis of resistivity measurements for 75% deformed Al-Mg-Fe-Mn (I5) alloy 100

7.5 Discussion..... 106

CHAPTER 8. Conclusions.....112

Bibliography.....114

LIST OF FIGURES

		Page No.
Figure 1.1	Audi A8-A1 space frame and seni materials distribution (AUDI) (www.key-to-metals.com)	1
Figure 2.1	Aluminum parts of the S-class Mercedes (Daimler Chrysler) made of Al-Mg alloys	6
Figure 2.2	Rear axel and subframes, wheels of Al-Mg sheet (BMW 5 and BMW 7-series) – Combination of welded sheets, hydroformed tubes and caste	7
Figure 2.3	Schematic processing route of aluminum alloys for automotive applications	7
Figure 2.4	Strain hardening response of high purity Al and Al-Mg binary alloys during cold rolling	10
Figure 2.5	Al-Mg phase diagram.	11
Figure 4.1	A schematic representation of experimental procedure	30
Figure 4.2	Accumulated amount of intermetallics in alloy I2 during solidification.	32
Figure 4.3	Accumulated amount of intermetallics in alloy I5 during solidification.	32
Figure 4.4	Stability of intermetallics as a function of temperature in alloy I2.	34
Figure 4.5	Stability of intermetallics as a function of temperature in alloy I5.	34
Figure 4.6	L-T section where hardness was measured.	37
Figure 4.7	Position of micro-hardness measurements on cold-rolled samples.	37

Figure 4.8	Mean hardness values as a function of true strain in cold rolled samples.	42
Figure 4.9	Circuit diagram of the experimental set-up for 4-point resistivity measurements.	49
Figure 4.10	Resistivity measuring probe.	51
Figure 4.11	Sample mounting on the probe.	51
Figure 4.12	Furnace loaded with resistivity probe.	51
Figure 4.13	Data acquisition unit including controllers and PC.	52
Figure 4.14	Resistance data collection interface (LabView)	52
Figure 5.1	Simulated experimental results, free of noise.	55
Figure 5.2	Simulated experimental results burdened with Gaussian noise and estimation of their first derivative.	55
Figure 5.3	Estimation of second derivative of simulated noisy data.	56
Figure 5.4	Showing that even with considerable amount of noise in data, number of inflection points and exrema can stiil be deduced	61
Figure 5.5	Effect of variation of smoothing parameter (0.01-0.09).	72
Figure 5.6	Effect of variation of smoothing parameter (0.1-0.9).	72
Figure 5.7	Illustration of procedure for finding suitable smoothing parameter.	74
Figure 6.1	Resistivity variation w.r.t. Temperature for pure Al and Al-1%Mg (CRC handbook of physics and chemistry, 2006).	77
Figure 6.2	Resistivity vs. T profile for 95% deformed Al-3%Mg.	79
Figure 6.3	Differentiation of $R(T)$ vs. T profile without smoothing data.	79
Figure 6.4	Smoothing of experimental data points by splines.	80
Figure 6.5	Robust numerical differentiation of smoothes $R(T)$ data.	82
Figure 6.6	Showing continuous increasing slope of resistivity as a function of temperature	83

Figure 7.1	Change of slope of resistivity curves as a function of temperature for 95% deformed Al-3%Mg alloy.	85
Figure 7.2	Microstructure of 95% deformed Al-3%Mg alloy on L-T section, showing layered structure and deformation bands.	86
Figure 7.3	Microstructure of 95% deformed Al-3%Mg alloy, quenched from 220°C, early stages of recrystallization.	86
Figure 7.4	Microstructure of 95% deformed Al-3%Mg alloy, quenched from 240°C, partial recrystallization.	87
Figure 7.5	Microstructure of 95% deformed Al-3%Mg alloy, quenched from 260°C, complete recrystallization.	87
Figure 7.6	Microstructure of 95% deformed Al-3%Mg alloy, quenched from 300°C, grain growth.	88
Figure 7.7	Micro-hardness as a function of temperature for 95% deformed Al-3%Mg alloy, mean of 50 measurements for each sample.	88
Figure 7.8	Change of slope of resistivity curves as a function of temperature for 75% deformed Al-3%Mg alloy.	90
Figure 7.9	Microstructure of 75% deformed Al-3%Mg.	92
Figure 7.10	Microstructure of 75% deformed Al-3%Mg, annealed and quenched from 175°C.	92
Figure 7.11	Microstructure of 75% deformed Al-3%Mg, annealed and quenched from 225°C.	93
Figure 7.12	Microstructure of 75% deformed Al-3%Mg, annealed and quenched from 250°C.	93
Figure 7.13	Microstructure of 75% deformed Al-3%Mg, annealed and quenched from 300°C.	94
Figure 7.14	Micro-hardness measurements as a function of temperature for 75% deformed Al-3%Mg, mean of 50 measurements for each sample.	94

Figure 7.15	Change of slope of resistivity curve as a function of temperature for 95% deformed Al-Mg-Fe-Mn (I5) alloy.	95
Figure 7.16	Microstructure of 95% deformed Al-Mg-Fe-Mn (I5).	96
Figure 7.17	Microstructure of 95% deformed Al-Mg-Fe-Mn (I5) alloy, annealed and quenched from 175°C.	97
Figure 7.18	Microstructure of 95% deformed Al-Mg-Fe-Mn (I5) alloy, annealed and quenched from 206°C.	97
Figure 7.19	Microstructure of 95% deformed Al-Mg-Fe-Mn (I5) alloy, annealed and quenched from 225°C.	98
Figure 7.20	Micro-hardness measurements as a function of temperature for 95% deformed Al-Mg-Fe-Mn (I5) alloy, mean of 50 measurements for each sample.	98
Figure 7.21	Change of slope of resistivity curve as a function of temperature for 75% deformed Al-Mg-Fe-Mn (I5) alloy.	101
Figure 7.22	Microstructure of 75% deformed Al-Mg-Fe-Mn (I5) alloy.	102
Figure 7.23	Microstructure of 75% deformed Al-Mg-Fe-Mn (I5) alloy, annealed and quenched from 175°C.	102
Figure 7.24	Microstructure of 75% deformed Al-Mg-Fe-Mn (I5) alloy, annealed and quenched from 212°C.	103
Figure 7.25	Microstructure of 75% deformed Al-Mg-Fe-Mn (I5) alloy, annealed and quenched from 225°C.	103
Figure 7.26	Micro-hardness measurements as a function of temperature for 75% deformed Al-Mg-Fe-Mn (I5) alloy, mean of 50 measurements for each sample.	104
Figure 7.27	Comparison of hardness variation during annealing for two samples of Al-3%Mg with different degree of deformation.	109
Figure 7.28	Comparison of hardness variation during annealing for two samples of Al-Mg-Fe-Mn (I5) with different degree of deformation.	109

Figure 7.29 Variation of hardness values as a function of degree of deformation for I2 and I5 alloys. 111

LIST OF TABLES

Page No.

Table 4.1 Composition of alloys investigated. 31

Table 4.2 Sub-lattice model of the phases present in the given alloy system. 33

Table 4.3 Statistical data analysis of micro-hardness data (confidence level = 95%). 41

Table 7.1 Summery of the results obtained from experimental work. 106

Chapter 1: Introduction

The main requirements of new generation vehicles include less fuel consumption, less pollution and luxurious design without compromising safety considerations. To fulfill these demands, thrust has been on developing new category of materials especially Al alloys (Figure 1 1). In particular, 5xxx series (Al-Mg) alloys, have emerged as a promising candidate for application in new age vehicles. The main reasons for wide spread use of 5xxx series aluminum alloys include high formability, good strength, good corrosion resistance, weldability, recyclability and thermal stability As far as application of 5xxx series (especially AA5754) alloys are concerned, they are specifically used to fabricate inner body panel, splash guard, heat shields, air cleaner, trays and covers, structural and weldable parts, load floors and body-in-white structures in vehicles.

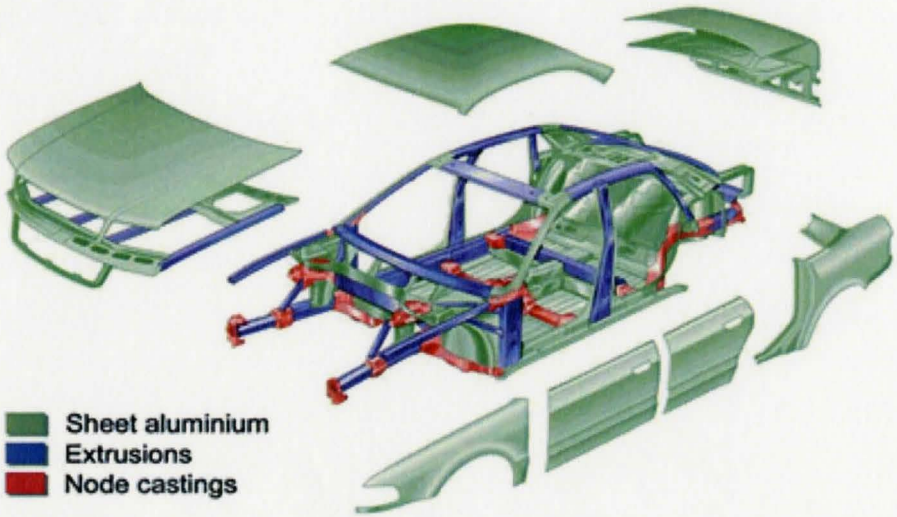

Figure 1.1:Audi A8-Al space frame and semi materials distribution (AUDI) (www.key-to-metals.com)

Cold working and annealing procedures are manipulated to control recrystallization during fabrication to achieve desired combination of mechanical properties in the sheet products (Sanders 1989). Industrial control of recrystallization mainly focuses on control of texture for formability, control of grain size and degree of recrystallization for surface appearance and damage related properties. Such control is achieved by maneuvering nucleation and growth of new grains. Nucleation density and crystallographic orientation of new grains are determined by inhomogeneities of the deformed structure whereas grain boundary mobility is controlled by second phases, which at the correct size will exert a pinning force on the boundary. Additionally, solutes impose a drag on moving grain boundaries. Therefore, the effects of solute atoms and second phase particles (including both fine and coarse particles) on recrystallization kinetics play a key role in deciding the final microstructure and consequently the mechanical properties of 5xxx series Al alloys.

Traditional way to achieve the required structure and properties in the flat-rolled aluminum alloy sheet involves extensive thermo-mechanical processing of as-cast materials produced by a direct-chill (DC) technology predominantly. The traditional multi-stage thermo-mechanical processing operations during fabrication of aluminum alloy sheet account for the major part of the cost of production. Higher processing costs of aluminum alloys make it difficult to reduce the cost of aluminum sheets as compared to steel sheets, which is major competitive material of aluminum alloys in automotive sheet applications. Development of manufacturing technologies with near-net-shape

capabilities have been considered as an efficient way out to cut down the processing costs, continuous strip casting technology being one of them.

Development of new processing techniques with near-net-shape capabilities, such as continuous strip casting, have mainly focused on minimizing the processing steps during sheet forming. It is expected that strips produced by continuous casting can directly be cold rolled to desired thickness and recrystallized in a continuous annealing furnace to manufacture sheets in two steps. Another proposed scheme involves direct hot-rolling of cast strips to produce recrystallized sheets of desired thickness.

However, there are certain technological and scientific issues associated with such kind of processing techniques that need to be investigated. One important issue out of them is to control recrystallization and optimize microstructure during processing to achieve desired mechanical properties. Therefore, development of such processing techniques demand a deep understanding of the microstructural changes in materials (especially recrystallization) during thermomechanical treatment. In addition, it is also requisite to have knowledge about the various factors (i.e. degree of deformation, alloying additions, etc.) affecting the response of the material and the way they influence the response.

In order to study recrystallization a sensitive, reliable and relatively easy method of characterization is required. There are several available methods to study recrystallization namely transmission electron microscopy, scanning electron microscopy, optical metallography, calorimetry (Hohne 2003, Starink 2004), hardness measurements and electrical resistivity measurements. Some of these characterization

techniques are either not *in-situ* in nature or too daunting and laborious. These constraints restrict the efficient use of these methods for the study of recrystallization.

Calorimetry and electrical resistivity measurements are the characterization methods, which are relatively easy to use. Although, electrical resistivity measurement is easy and more sensitive method as compared to calorimetry, yet it has not been used as *in-situ* method so far. In light of the issues mentioned in this section, following objectives have been set for the proposed work:

1. To investigate an applicability of *in-situ* electrical resistivity measurements to reveal the onset of recrystallization and for estimating its extent.
2. To prove by using microstructural characterization and micro hardness measurements that the event observed in electrical resistivity experiments represents with recrystallization.
3. To examine what influence an iron content and strain introduced have upon the recrystallization.
4. To develop a robust spline-based procedure of numerical differentiation and to apply it to extracting useful data from raw $R(T)$ measurements.
5. To employ the methods of computational thermodynamics for finding such a method of samples preparation that the formation of second-phase particles does not interfere with recrystallization.

Chapter 2: Metallurgy of 5xxx Aluminum alloys and their usage in automotive industry

Non heat-treatable alloys can be crudely defined as those alloys that cannot achieve higher strength by heat-treatment i.e. they show no effective precipitation hardening. These alloys achieve higher strength either by strain hardening (e.g. dislocation structures introduced by cold working) or by solid solution strengthening. Major groups of non heat-treatable aluminum alloys include pure Aluminum group (1xxx series), Al-Mn group (3xxx series), Al-Si group (4xxx series) and Al-Mg group (5xxx series). The non heat-treatable alloys are used for flat products i.e. plate, thin sheets and foils. Out of these groups of alloys, Al-Mg (5xxx series) group has found widespread application in automotive industry. Commercial 5xxx series alloys contain Mg in the range of 0.5 to 6.0-wt%.

As far as increasing interest in aluminum alloys for automotive applications is concerned, it has been due to the general need in weight saving resulting in further reduction in fuel consumption. In particular, sheet applications for new lightweight structural parts and body in white construction are attaining prime importance. The focus has been to ensure that the semi-finished products of aluminum alloys meet the following main requirements:

1. Sufficient strength for structural stability and durability, dent resistance and crash worthiness.
2. Good formability for stretching, bending and deep drawing operations.

3. Good weldability and other joining properties.
4. Reasonably good corrosion resistance
5. Recyclability and low material and fabrication costs.

In particular, major applications of 5xxx aluminum alloys in automotive parts include inner body panels, splash guards, heat shields, air cleaner trays and covers, structural and weldable parts, load floors (sheets) and body-in-white structures (Figure 2.1, Figure 2.2). In order to achieve desired mechanical properties, it is necessary to have a deep understanding about the specific material behavior and the underlying metallurgical effects involved. A schematic plot of the processing route for conventional production of aluminum sheet alloys by DC (direct chill) ingot casting, hot and cold rolling and final annealing treatment is shown in Figure 2.3.

Figure 2.1: Aluminum parts of the S-class Mercedes (Daimler Chrysler) made of Al-Mg-Mn alloys (www.key-to-metals.com)

Figure 2.2: Rear axel subframes, wheels of Al-Mg sheet (BMW 5 and BMW 7-series) - Combination of welded sheets, hydroformed tubes and caste (www.key-to-metals.com)

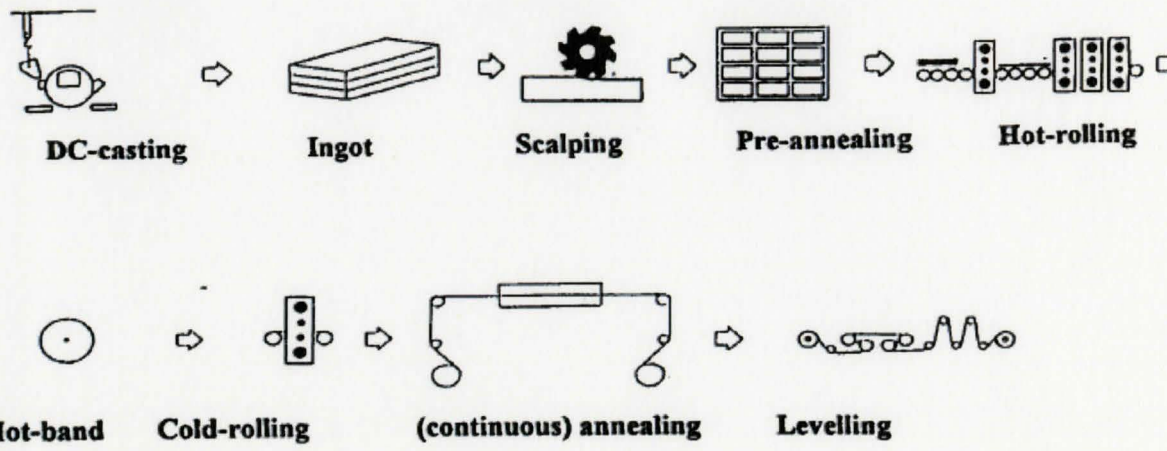

Figure 2.3:Schematic processing route of aluminum alloys for automotive applications (Hirsch 1997)

During processing, structure of the material is transformed from the as cast structure to a fine grained recrystallized structure in different stages of processing by hot and cold rolling and final soft annealing in a continuous annealing furnace. The recrystallized structure is formed during hot rolling stage, however, this is not the last stage. The crucial stage is the continuous annealing after cold rolling. This is the stage where desired microstructure is obtained via controlling recrystallization in order to fabricate sheets with required mechanical properties.

The conventional DC processing technique is a multi-stage process, which makes it difficult to reduce the processing costs of aluminum alloys. In order to curb the manufacturing costs, an alternative promising technique, continuous casting or strip casting, is getting widespread attention. Continuous casting involves solidification of liquid metal directly into strip form. Because of near-net-shape fabrication capabilities, continuous casting technique eliminates the need for the capital-intensive hot-rolling equipment and the associated costs in fabricating large DC ingots to sheets. Further, the as-cast aluminum can directly be fed into in-line rolling mills resulting in less number of rolling-mill passes. Reduction in number of rolling-mill passes will finally result in lower investment costs, higher yields, and shorter processing times. However, CC casting technique is in developmental stage at large and CC cast alloys do not have wide spread usage in automotive industry at the moment.

In case of 5xxx aluminum alloys, sheets are supplied to automotive manufacturer in the fully annealed/recrystallized condition for fabricating vehicle parts by stamping predominantly. During stamping, fabricated vehicle parts derive higher strength from the

strain hardening capability of 5xxx series Al alloys. In order to obtain desired recrystallized structure with specific mechanical properties, optimization of recrystallized structure is required. Such optimization of recrystallized structure can be achieved by maneuvering the parameters such as alloy chemistry and processing route (thermo-mechanical processing). However, optimization of the recrystallized structure to avoid material failure during stamping and obtaining desired mechanical properties is a daunting task. Therefore, understanding the effect of various parameters on recrystallization of 5xxx alloys is a key factor for restricting the sheets processing costs by reducing number of steps, as well as, for optimizing recrystallized structure to get desired mechanical properties.

It is well known that magnesium decreases the density of aluminum, but most importantly, it promotes the strengthening of aluminum through work hardening. In 5xxx alloys, although there is some solution strengthening because of Mg in the solid solution, the major role of Mg is to provide strengthening through its effect on work hardening. The behavior of high purity Al-Mg binary alloys show good agreement with the Holomon equation:

$$\sigma = k \bullet \varepsilon^n \qquad (2.1)$$

As shown in Figure 2.4, an addition of Mg to pure Al results in a decrease in the strain hardening exponent n, but an increase in k. With further increase in Mg content, n remains constant, but k continues to increase, indicating that Mg is increasing the rate of work hardening (Sanders1989, Burger 1995)

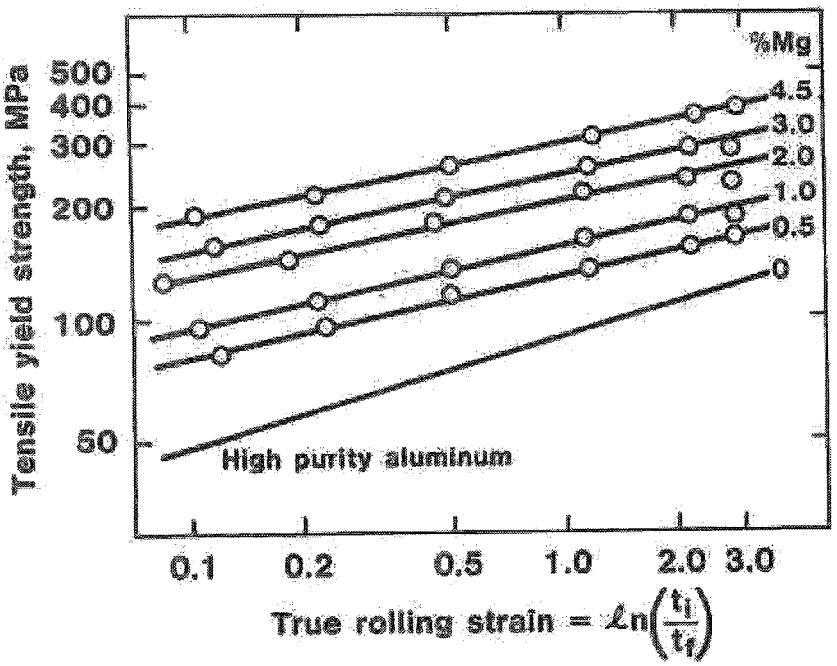

Figure 2.4: Strain hardening response of high purity Al and Al-Mg binary alloys during cold rolling (Sanders 1989)

Magnesium has a very high solid solution solubility in aluminum (up to 15wt%) at 451^{0}C whereas, the solid-solubility of Mg decreases to 1.7-wt% at room temperature (Figure 2.5). It leads to the fact that most of the commercial alloys are produced and used in such a condition that the matrix is supersaturated with Mg. Since the kinetics of decomposition of the supersaturated solid solution is very slow, the Al-Mg solid solution is very stable at room temperature and does not decompose to precipitate out Mg. The 5xxx Al alloys containing less than 5 wt% of Mg are structurally stable at room temperature whereas those with less than 3 wt% of Mg are stable even at elevated temperatures. It has been seen that, in commercially available alloys, essentially all of the

Mg can be retained in solution without incorporating any extraordinary quenching rate (Sanders1989).

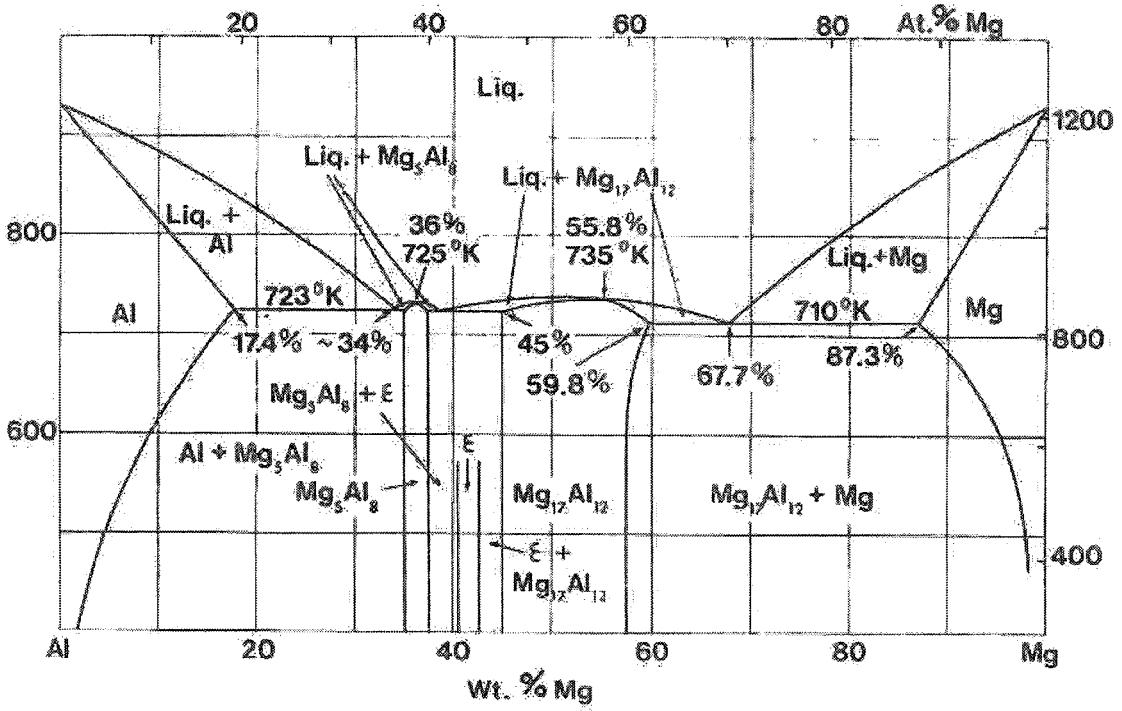

Figure 2.5: Al-Mg phase diagram (Mondolfo 1976)

If the matrix is supersaturated with Mg, there is always a driving force for the precipitation of second phase particles from the solid solution. This is not a big problem in alloys containing less than 3 wt% Mg but alloys containing 4-6 wt% Mg does show some precipitation of Al_8Mg_5 at higher temperatures (approx. above 200°C). This precipitation mostly occurs on gross structural defects i.e. grain boundaries and shear bands. Heterogeneities such as dislocations or grain boundaries are the regions of higher free energy than average free energy. Therefore, when a nucleus forms replacing part of a boundary area or dislocation line the associated free energy is available to drive the reaction. Increase in temperature increases the mobility of solutes resulting in enhanced

kinetics of precipitation. Therefore, Deformation and high temperatures are factors, which accelerate the precipitation.

In age hardening, GP zones form within seconds from the quench in high energy areas (grain boundaries, dislocations, etc.) but they are small (1-1.5 nm diameter) and most of the excess vacancies remain around them as a cloud resulting in little or no strain and no appreciable hardening (Mondolfo 1976). Upon aging for years at room temperature, the zones grow up to 10 nm diameters and tend toward a tetragonal lattice. The critical temperature above which zones do not form is very low (47-67 °C) and above this temperature aging starts with the formation of the β' phase at the grain boundaries. This phase forms first at the grain boundaries producing solute depleted zone around them. The β' phase is coherent with the matrix and it has hexagonal structure (a = 10.02 nm, c = 16.36 nm). At temperatures up to approximately 277 °C, the stable β (Al_8Mg_5) is formed from the β', whereas, the β phase is formed directly from the matrix with loss of coherency above 277 °C (Mondolfo 1976).

Since Al has high stacking fault energy, it makes dislocation cross slip easy resulting in faster recovery processes during both deformation and low temperature annealing. The evidence of mutual dislocation annihilation and extensive rearrangement of dislocations into cells and subgrains can easily be seen in deformed pure Aluminum. The amount of retained lattice strain after deformation is increased with the addition of Mg to Al. For a given amount of deformation, there is a more rapid increment in lattice strain and amount of retained strain with the higher contents of Mg. It is well established that Mg decreases the tendency for dynamic recovery and dislocation rearrangement into

lower energy configurations by lowering stacking fault energy and restricting dislocation mobility (Sanders 1989). Thus, addition of Mg to Al increases the amount of dislocations in the alloy. The overall effect of Mg addition is that by suppressing recovery, Mg increases both the dislocation multiplication and amount of stored dislocations resulting in increased strength (Sanders 1989).

The deformation microstructure evolution is a very complex process in case of Al-Mg alloys. It has been observed that Al-3wt%Mg alloy undergoes inhomogeneous plastic deformation. At medium to large strains ($\varepsilon \geq 0.5$), formation of grain scale shear bands is a characteristic feature of the deformed microstructure. This mode of deformation can be attributed to Mg atoms in solid solution. The Mg atoms in solid solution impede matrix dislocations and inhibit the homogeneous dynamic recovery processes that are normally operated in pure Al (Korbel 1986).

It has been shown that at low strains ($\varepsilon \leq 0.35$), the deformation microstructure consists of dense dislocation tangles and diffused cells. On further deformation, micro-band clusters and layered dislocation structures are developed in the microstructure (Nakayama 1987). It has been indicated that there are inherent internal stresses in a layered dislocation structure (Mughrabi 1983) and a combination of these internal stresses with the applied stress destabilizes the microstructure. The destabilization of deformed microstructure eventually results in the fragmentation of micro-band clusters and shear band nucleation (Korbel 1986, Morri 1985, Nakayama 1987).

Growth of a shear band occurs along its shear direction by accommodation of strain at the tip (Nakayama 1987). Since the stress concentration at the ends of a shear

band is dependent on its length, large shear bands develop at lower strains in a material with larger grain size (Korbel 1986). Therefore, shear bands may be confined to the interior of the grains during rolling reductions in a fine-grained material. Their further growth may only be expected at very high strains. In a recent study on AA5754 alloy (Azari 2004), it has been reported that the homogenized material with a large initial grain size (of the order of 150 μ-m), contains a higher frequency of longer shear bands as compared to the materials with smaller grain sizes.

Because of their high local dislocation density and large misorientation with respect to the surrounding matrix, shear bands have been indicated as the favored recrystallization nucleation sites in Al-Mg (>3wt% Mg) alloys. It was also shown that Particle-stimulated nucleation (PSN) competes with both shear band and transition band nucleation in commercial Al-Mg (AA5754) alloys (Azari 2004).

As discussed above, the Mg is very effective in bringing about high strength via its effect on solid solution strengthening and strain hardening. However, there are certain practical problems, which restrict the exploitation of this effect of Mg with increasing Mg content in producing commercial wrought products. These problems include fabrication difficulties such as alligatoring and edge cracking during rolling and susceptibility of high-Mg alloys to intergranular corrosion or stress corrosion cracking. In order to overcome these problems, other solid solution elements are added to achieve higher strengths. It is very important to ensure that the element is able to provide additional work hardening but will not chemically interact with Mg and remove it from solid

solution. Mn is such an element, which is added to 5xxx alloys to provide them additional strengthening at lower Mg contents.

In wrought alloys ,Al- Mg-Mn system has high strength in the work-hardened condition, high resistance to corrosion, and good welding characteristics. Mn increases strength either in solid solution or through the formation of finely precipitated intermetallic phase. It has been observed that even small additions of Mn to a Al-3.5 wt% Mg binary alloy is more efficient in enhancing strengthening than further Mg additions. It does not affect corrosion resistance adversely. Solid solubility of Mn in Al is very limited in the presence of normal impurities but it remains in solid solution in as cast alloys when chill cast. Due to this property, most of the Mn added is retained in solid solution even in large ingots. It has been seen that Mn is primarily retained in solid solution in 5xxx alloys to strengthen them via solution hardening.

Iron is mostly present as impurity in aluminum. Fe has a high solubility in molten Al but its solubility decreases to very low levels in the solid states (~ 0.04 wt%). Therefore, when in solid state, most of the Fe present in Al above 0.04 wt% appears as second phase particles in combination with Al and other elements. Depending upon the composition of the alloy, presence of constituent phases containing Fe, Mn, and Si (usually present as impurity) include $Al_{12}(Fe,Mn)_3Si$, $Al_6(Fe,Mn)$, $Al_{13}Fe_4$, or $Al_{16}(Fe,Mn)_4Si_3$ (Sanders1989). Commercial alloys can contain up to 1%Mn. When Mn is precipitated during preheating it forms dispersiods with other elements, the $Al_6(Mn,Fe)$ phase is favored since the Si is already tied up with Mg as Mg_2Si (Sanders 1989).

In particular case of AA5754, presence of large constituent particles such as $Al_6(Mn,Fe)$, Mg_2Si and sub-micron size $Al_6(Fe,Mn)$ and Al_6Mn dispersoids have been indicated (Azari 2004). Fe-rich constituent particles generally form during solidification. Intermetallics containing Fe and Mn are usually very stable thermodynamically. They do not disappear during solutionizing treatment whereas Mg_2Si dissolve at 560°C (Azari 2004). These second phase particles do not contribute much to the strength of alloy via precipitation hardening but they affect the recrystallization. The insoluble coarse intermetallics (>1 microns in size) may act as nucleation sites and influence the rate of recrystallization and recrystallization onset temperature.

If the finer sub-micron size dispersoid are present in sufficient amount, they are extremely effective in pinning matrix dislocations and interfere with the normal development of a deformation substructure. These dispersoids are believed to be efficient in interfering with both the homogeneous and inhomogeneous recovery processes. It is expected that if the volume fraction of fine dispersoids in matrix is high enough, they may totally suppress inhomogeneous recovery processes resulting in shear band formation. Since the Mn rich dispersoids precipitate during homogenization at high temperature (~560°C), the homogenized material is expected to have high a higher volume fraction of sub-micron size particles as compared to the materials with other heat-treatment procedures.

Chapter 3: Recrystallization and related phenomena

When a crystalline material is deformed, its free energy is increased due to the generation and accumulation of dislocations and interfaces. The increase in dislocation density is due to the continued trapping of newly created mobile dislocations by existing dislocations and their incorporation into the various microstructural features (e.g. shear bands, deformation bands, boundaries of cells or subgrains etc.) that are characteristic of the deformed state. It has been observed that the stored energy of cold work increases linearly with strain, until a saturation value is reached (Baker and Martin 1983). It was also found that the addition of particles raises the stored energy and the increase is greater for a larger number of particles, for a given strain. The increase in stored energy owing to particles increases with increasing strain.

However, it is worth mentioning that the most of the energy absorbed during the deformation process is converted as heat and a very small portion of this energy (1-10 %) is stored in the deformed structure as either elastic energy or strain energy. The stored energy in terms of accumulated dislocation density can be represented by the following expression:

$$E_D = \frac{1}{2}\rho G b^2 \tag{3.1}$$

where, $\rho = \rho(\varepsilon)$ = dislocation density, G = shear modulus of the material, b = Burgers vector

In deformed and thermodynamically unstable material, these defects do not vanish at low temperature because of the lack of necessary atomistic mechanisms at low

temperatures resulting in the retention of unstable defect structures after deformation (Humphreys and Hatherly 2004). The amount of stored energy is dependent on both deformation parameters (mode of deformation, strain, strain rate, temperature) and material characteristics (lattice structure, stacking fault energy, solute content, grain size, dispersed second phase content and its distribution). The strain path by which the material is deformed affects the flow stress, deformation texture, recrystallization kinetics and recrystallized grain size (Higginson 2002, Lindh 1993, Bacroix 1995, Baczynski 1996).

The stored energy provides the source for all the property changes that are typical of deformed metals. In the common case of deformation at room temperature, almost all of the stored energy is derived from the accumulation of dislocations and the essential differences between the deformed and the annealed states lie in the dislocation content and arrangement. When the deformed material is heated to a high temperature, the defects may be removed or arranged in configurations of low energy due to the effect of thermally activated processes, such as solid-state diffusion that provides the mechanism for such process. During annealing, the microstructure and the properties are partially restored to their original values by a process called recovery in which annihilation and rearrangement of the dislocation occurs.

During recovery, the microstructural changes are relatively homogeneous and the boundaries between the deformed grains are not affected much. Only partial restoration of properties is observed during recovery as the dislocation structure is not completely removed and it reaches a metastable state. A further restoration process called

recrystallization may occur in which new dislocation-free grains are formed within the deformed or recovered structure. The newly formed dislocation-free grains then grow and old grains are consumed resulting in a new grain structure with a low dislocation density (Humphreys and Hatherly 2004).

For controlling recrystallization effectively, it is very important to understand the mechanisms of nucleation and the parameters that control this process (Humphreys and Hatherly 2004, Humphreys 2004). It has been observed that recrystallization originates at inhomogeneities in the deformed microstructure. The typical nucleation sites having high local misorientations, include pre-existing high angle grain boundaries, transition bands, highly misoriented deformation zones around large second phase particles, highly misoriented regions within shear bands and deformation bands in very heavily deformed (> 90 % reduction in thickness) materials (Doherty et al 1997, Humphreys 2004, Humphreys and Hatherly 2004, Chan and Humphreys 1984, Humphreys 1977, Hansen and Bay 1981).

Solutes in general hinder recrystallization. Increasing the solute content of any solid-solution alloy raises the recrystallization temperature and decreases the rate of recrystallization, by reducing the mobility of the high-angle boundary which surrounds an expanding new grain (Mould and Cotterill 1967). Solutes in some cases may have a strong influence on the recovery process, which is an integral part of nucleation and which may affect the driving force for recrystallization. However, the majority of experimental work suggest that the main influence of solutes is on the grain boundary

mobility and hence on the growth rate of recrystallizing grains (Humphreys and Hatherly, 2004).

The effects of second phase particles on recrystallization are very complex. If the particles are present during deformation, they will affect the deformation microstructure and texture via increase in dislocation density, large heterogeneities at coarser particles, and changing the homogeneity of slip (i.e. shear bands). During annealing, closely spaced particles give pinning effect on the grain boundaries (also called "Zener pinning"), whereas the deformation heterogeneities at large particles are reported to act as nucleation sites via particles stimulated nucleation (PSN).

Dispersoid particles control the recrystallization kinetics by influencing nucleation rate and growth rate of new grains. The nucleation rate is affected through the pinning of the dislocation structure, while the growth rate is affected by pinning of grain boundaries through the Zener drag. The usefulness of dispersiods of course is determined by their sizes and volume fractions, which are in turn determined by the *concentration of the dispersoid-forming elements* and by the *homogenization temperature* (Humphreys and Hatherly 2004).

Large particles, typically larger than 2 microns in diameter, are known to be sites for nucleation of recrystallization by promoting Particle Stimulated Nucleation (Humphreys 1977, Sandstrom 1980). Most of the Al alloys of commercial purity and produced by ingot casting contain iron bearing phases in this size range. These phases originate from the solidification process. These phases are also known as constituents. Besides the iron bearing particles, all other large second phases such as Mg_2Si, can be

sites for PSN. Apart from the contribution of PSN to recrystallization, other mechanisms such as Persistent Cube Bands and grain boundary nucleation also contribute significantly to the recrystallization process (Weiland 2004).

Since most of the commercial alloys contain second phase particles and such particles have a strong influence on the recrystallization kinetics, microstructure and texture, a combination of alloying and materials processing will make it possible to control the distribution of second phase particles in the microstructure more accurately if the effects of second phase particles on recrystallization is fully understood.

As it is well established that the strain hardened condition of the 5xxx alloys is of commercial interest as it provides the highest strength possible to all non heat treatable Al alloys. Since strain hardened condition is a metastable state, there is a driving force for internal strain to relax through the process of static recovery. Recovery refers to changes in a deformed material which occur before the onset of recrystallization, and which partially restore the properties to their values before deformation (Humphreys and Hatherly 2004). The rate of property change is highest in the case of highly strain-hardened tempers as the driving force for recovery is greatest in this case. This behaviour, sometimes termed as "age softening", is a metallurgical recovery process dependent on both temperature and time.

The extent of recovery depends on the amount of strain, annealing temperature and nature of the material. For example, solutes may influence recovery by their effect on the stacking fault energy, by pinning dislocations, or by affecting the concentration and mobility of vacancies. Pinning of dislocations by solutes will inhibit the dynamic

recovery as well as the static recovery. Inhibition of dynamic recovery will result in a higher stored energy as compared to solute free material that, in turn, will promote the recovery whereas inhibition of dynamic recovery will obviously retard the recovery. This kind of interaction makes it difficult to predict the net effect (Humphreys and Hatherly 2004).

It must be understood that the stored energy is finite in magnitude and fixed for a given set of conditions such as material, temperature, mode of deformation, purity, and grain size. Therefore, it should be realized that recovery and recrystallization are competing processes as both are driven by the stored energy of deformed state and difficulty of these processes will determine whether or not both can occur and the temperature ranges in which either or both occur. Since recovery prior to the recrystallization lowers the driving force for recrystallization, there are high chances that a significant amount of prior recovery will influence the nature and the kinetics of recrystallization. It is sometimes difficult to differentiate between recovery and recrystallization because recovery mechanisms play an important role in nucleating recrystallization.

The heating rate of a specimen to the annealing temperature is another very important parameter that affects the rate of recrystallization (Ferry and Jones 1998, Bampton et al. 1982). If heating rate is such that it increases the amount of recovery before onset of recrystallization (i.e. slow heating), the driving force for recrystallization will be reduced resulting in retarded recrystallization. The required condition for

enhanced recovery at low heating rates is that activation energy of recovery should be lower than that of recrystallization.

During the annealing of cold rolled super saturated solid solutions, either or both precipitation and recrystallization are found to occur. The presence of a deformed microstructure is believed to affect the nature and kinetics of the precipitation due to the interference of precipitates with recovery and recrystallization (Zurob 2001, Zurob 2002, Wang 2002). If a supersaturated solid solution is deformed and annealed at a low heating rate, precipitation may occur before recrystallization and hinder it. In this case the particles are unlikely to be distributed uniformly and will form preferentially on the boundaries. The pinning pressure due to the particles will therefore be greater than for a random particle distribution. In case of rapid heating, recrystallization may be completed before any precipitation occurs and will not affect recrystallization significantly. Since interaction of precipitation and recrystallization is mainly governed by heating rate, it can be expected that heating rate have a strong effect on recrystallization.

Although this work does not deal with the mathematical formulation of kinetics of recrystallization explicitly, it would be interesting and informative to conclude this section with the seminal work by Russian mathematician **Andrei Nikolaevich Kolmogorov** *"On the statistical theory of crystallization of metals"* published in 1937. This text was translated from Russian to English by Dr. Dmitri V. Malakhov.

We shall be concerned with the process of the growth of a crystal when nucleation centers are formed randomly. A particular difficulty is that growing grains may interact with each other. A collision between grains impedes their further growth. It is intended to

calculate the probability $p(t)$ that an arbitrarily (randomly) taken point P within the parent phase will have been inside the recrystallized material by time t. This probability can be deemed as a fraction of old phase transformed during the period of time from 0 to t. In addition, it is intended to calculate a total number of crystallization centers formed during the whole transformation process.

Let us start with the mathematical formulation of the problem. In the beginning, *i.e.* at $t=0$, the whole volume V is occupied with a parent phase (*e.g.* deformed Al alloy). After time t, a part of the volume is occupied with a new phase; let us denote this part as $V_1(t)$. How does $V_1(t)$ increase with time? For answering this question, let us make two assumptions.

Firstly, new nuclei appear in the free volume $V-V_1$. For any volume $V' < V-V_1$, the probability that one nucleation center is formed from t to $t+\Delta t$ is equal to

$$\alpha(t)V'\Delta t + o(\Delta t)$$

where $o(\Delta t) \ll \Delta t$. The probability that more than one embryo is formed is equal to $o(\Delta t)$. These probabilities do not depend on a distribution of recrystallization centers formed prior to t if the distribution guarantees that the volume V' is free of pieces of the new phase by moment t.

Secondly, the new phase growths with the velocity

$$c(t,n) = k(t)\cdot c(n)$$

which depends on time t and direction n. It is assumed that the ends of vectors $c(n)$ built from the origin of the coordinate system and oriented in the direction n form a convex surface.

It is clear that $\dim(c(t,n)) = \text{cm/sec}$. In what units are $k(t)$ and $c(n)$? This question is irrelevant since neither k nor c can be found separately in all equations below. They always enter the expressions together as the product. For the sake of determinacy let us postulate that $\dim(c(n)) = \text{cm/sec}$ and $k(t)$ is dimensionless.

Although the rate of growth $c(t,n)$ may depend on the direction n, this dependence must be the same in all points. In other words, expressions derived below are valid if either the growth rate is the same in all directions or all particles composed of new phase are identically oriented in space.

In order to calculate the probability *p(t)*, let us introduce the entity c defined by the following equality:

$$c^3 = \frac{1}{4\pi}\int_S c^3(n)\,d\sigma$$

where the integration is carried out along the surface of the unit sphere (i.e. the sphere whose radius is equal to 1) whose center is in the origin of the coordinate system. Apparently, the volume of the crystal freely growing around a crystallization center formed at the moment t_0, at the moment t will become equal to

$$\frac{4\pi}{3}c^3\left(\int_{t_0}^{t} k(\tau)\,d\tau\right)^3$$

Now let us consider a randomly taken point P belonging to volume V, which is separated from the surface enveloping the volume by a distance greater than

$$\max(c)\int_0^t k(\tau)\,d\tau$$

For the point P to be situated inside the recrystallized substance, it is necessary and sufficient that at any moment $t' < t$ in any point P' separated from the point P by a distance lesser than

$$c(\bar{n})\int_{t'}^{t} k(\tau)\,d\tau$$

a nucleus is formed ($\bar{n}$ is the direction from P' to P).

For a fixed t', the volume $V'(t')$ occupied by points P' satisfying the just formulated condition is equal to

$$V'(t') = \frac{4\pi}{3}c^3\left(\int_{t'}^{t} k(\tau)\,d\tau\right)^3$$

The probability that during the period of time $\Delta t'$ a center of crystallization is formed within the volume $V'(t')$ is equal to

$$\alpha(t')V'(t')\Delta t' + o(\Delta t')$$

The probability that a center of crystallization is **not** formed is equal to

$$1-\alpha(t')V'(t')\Delta t' + o(\Delta t')$$

The probability that the point P will not be enclosed in the new phase by time t is equal to

$$q(t) = \prod_{i=1}^{s} \{1 - \alpha(t')V'(t')\Delta t'\} + o(1) \tag{3.2}$$

where $t = s\Delta t'$, $t_i = i\Delta t'$, $o(1)$ is infinitesimally small if $\Delta t'$ is infinitesimally small.

$$\begin{aligned} \ln q(t) &= \sum_{i=1}^{s} \ln\{1 - \alpha(t')V'(t')\Delta t'\} + o(1) \\ &\approx -\sum_{i=1}^{s} \alpha(t')V'(t')\Delta t' + o(1) \to -\int_0^t \alpha(t')V'(t')dt' \\ &= -\frac{4\pi}{3} c^3 \int_0^t \alpha(t') \left(\int_{t'}^{t} k(\tau)d\tau \right)^3 dt' \end{aligned} \tag{3.3}$$

The probability $p(t)$ that the point P will be within the new phase by time t is equal to $1 - q(t)$:

$$p(t) = 1 - \exp\left(-\frac{4\pi}{3} c^3 \Omega \right) \tag{3.4}$$

where

$$\Omega = \int_0^t \alpha(t') \left(\int_{t'}^{t} k(\tau)d\tau \right)^3 dt' \tag{3.5}$$

If the volume V is much greater than sizes of individual grains, then $V'(t') \approx Vp(t)$. By taking into account (3.4), one arrives at:

$$V_1(t) = V\left(1 - \exp\left(-\frac{4\pi}{3} c^3 \Omega \right)\right) \tag{3.6}$$

where Ω is given by (3.5).

If $\alpha(t)$ and $c(t,n)$ do not depend on time, then they can be takes as

$$\alpha(t)=\alpha, k=1$$

In this case

$$\Omega=\int_o^t \alpha\left(\int_{t'}^t d\tau\right)dt'=\alpha\int_0^t (t-t')^3\,dt'=-\alpha\int_0^t (t-t')^3\,d(t-t') \\ =-\alpha\frac{(t-t')^4}{4}\Bigg|_{t'=0}^{t'=t}=\frac{\alpha t^4}{4} \tag{3.7}$$

Subsequently, (3.6) results in

$$V_1(t)=V\left(1-\exp\left(-\frac{\pi}{3}c^3\alpha t^4\right)\right) \tag{3.8}$$

If the volume V is sufficiently large, then a number $N(t)$ of centers of crystallizations formed from 0 to t is equal to

$$N(t)=V\int_0^t \alpha(\tau)q(\tau)\,d\tau \tag{3.9}$$

For $\alpha(t)=\alpha$ and $k=1$, (3.9) gives:

$$N(t)=V\alpha\int_0^t \exp\left(-\frac{\pi}{3}c^3\alpha\tau^4\right)d\tau=V\frac{3^{\frac{1}{4}}}{\pi^{\frac{1}{4}}c^{\frac{3}{4}}\alpha^{\frac{1}{4}}}\int_0^t \exp\left(-\frac{\pi}{3}c^3\alpha\tau^4\right)d\left(\tau\frac{\pi^{\frac{1}{4}}c^{\frac{3}{4}}\alpha^{\frac{1}{4}}}{3^{\frac{1}{4}}}\right) \\ =V\sqrt[4]{\frac{3\alpha^3}{\pi c^3}}\int_0^{\sqrt[4]{\frac{\pi c^3\alpha}{3}}t} e^{-\xi^4}d\xi \tag{3.10}$$

If $t\to\infty$, then (3.9) and (3.10) give the total number of nucleation sites formed during the whole process. Since $\int_0^\infty e^{-\xi^4}d\xi=\frac{1}{4}\frac{\pi\sqrt{2}}{\Gamma(3/4)}\approx 0.9$ and $\sqrt[4]{3/\pi}\approx 1$, one can use the following approximation:

$$N(t \to \infty) = 0.9V\left(\frac{\alpha}{c}\right)^{\frac{3}{4}} \tag{3.11}$$

It is instructive to consider the case when all centers of crystallization are formed right in the beginning of the process, β centers per unit volume.

Instead of (3.5), one obtains:

$$\Omega = \beta\left(\int_0^t k(\tau)\,d\tau\right)^3$$

The expression (3.6) remains unchanged. For $\forall t > 0$, the expression (3.9) is replaced with a trivial equality $N = V\beta$. If one assumes that $k = 1$, *i.e.* that $c(t,n)$ is independent of time, then

$$\Omega = \beta t^3$$

$$V_1(t) = V\left(1 - \exp\left(-\frac{4\pi}{3}c^3\beta t^3\right)\right)$$

Chapter 4: Experimental strategies and their basis

A general scheme of experimental approach is shown in Figure 4.1 indicating the various steps involved in experimental procedure whereas the composition of alloys selected for this study has been indicated in Figure 4.1. The rationale behind adopting this scheme will be discussed in the following sections.

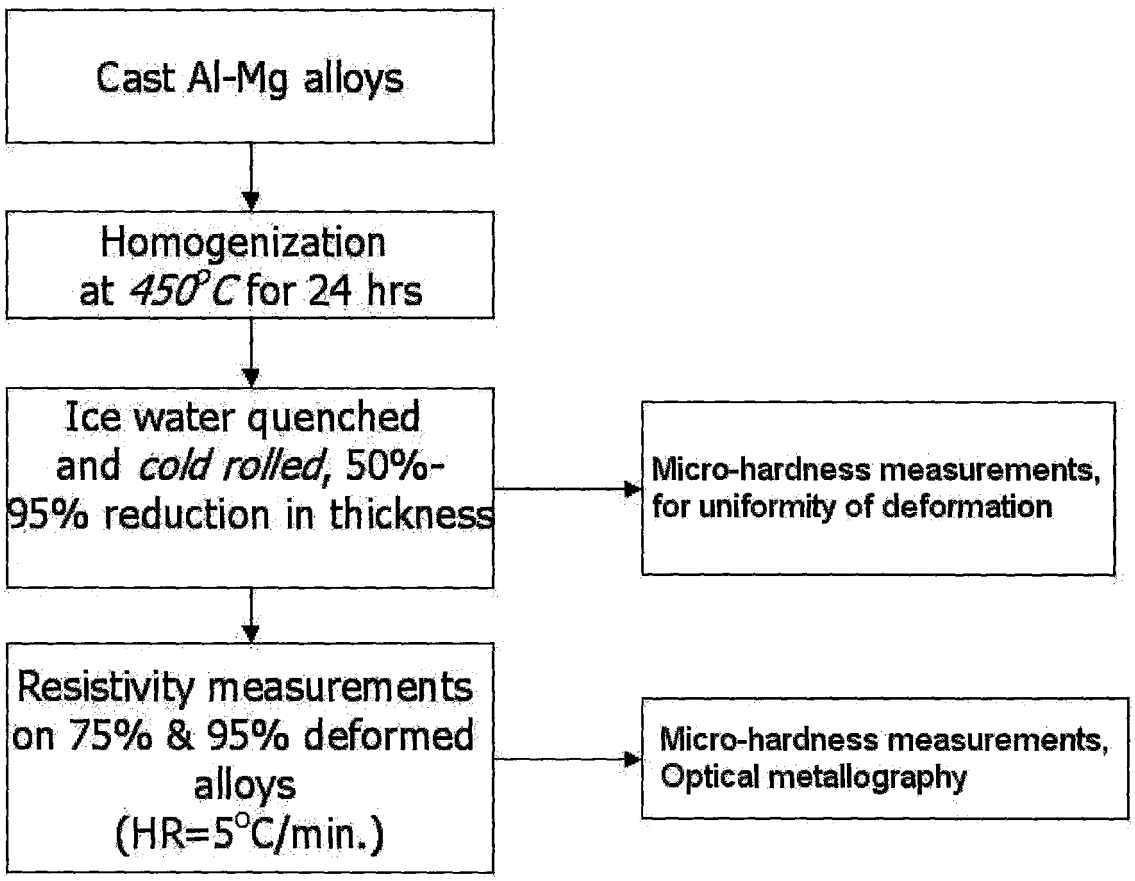

Figure 4.1: A schematic representation of experimental procedure

Table 4.1: Composition of alloys investigated

Alloy ID	Si (wt.%)	Fe (wt.%)	Mn (wt.%)	Mg (wt.%)	Al (wt%)
I-2	0.05	0.07	0.002	2.98	balance
I-5	0.05	0.51	0.65	3.1	balance

4.1: Thermodynamic modeling of the Al-Mg-Mn-Fe system

Since this work specifically deals with the characterization of recrystallization, precipitation needs to be kept separated to avoid its interference on resistivity response due to recrystallization. Therefore, this section deals with the problem of establishing a solutionizing scheme for the selected alloys in such a manner that precipitation does not interfere with the recrystallization process during annealing of the alloys. In addition, an estimation of accumulated amount of second phase particles formed during solidification has also been done along with the identification of these particles.

To deal with the issues mentioned above, computational thermodynamics has been considered as a viable tool. Calculations for thermodynamic modeling of the Al-Mg systems (compositions as mentioned in Table 4.1) have been carried out by Thermo-Calc using Origin. For assessing amount and nature of intermetallics formed in the course of solidification process of Al-Mg-Mn-Fe melts with composition specified in the Table 4.1, Scheil formalism was employed (Figure 4.2 and Figure 4.3). The nature of these accumulated second phase particles has been clarified by using sub-lattice model (Table 4.2).

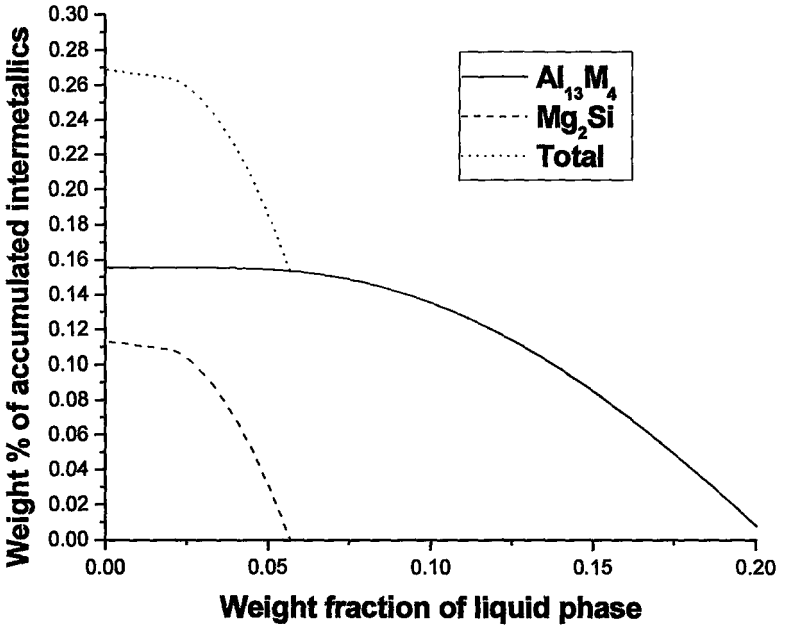

Figure 4.2: Accumulated amount of intermetallics in alloy I2 during solidification

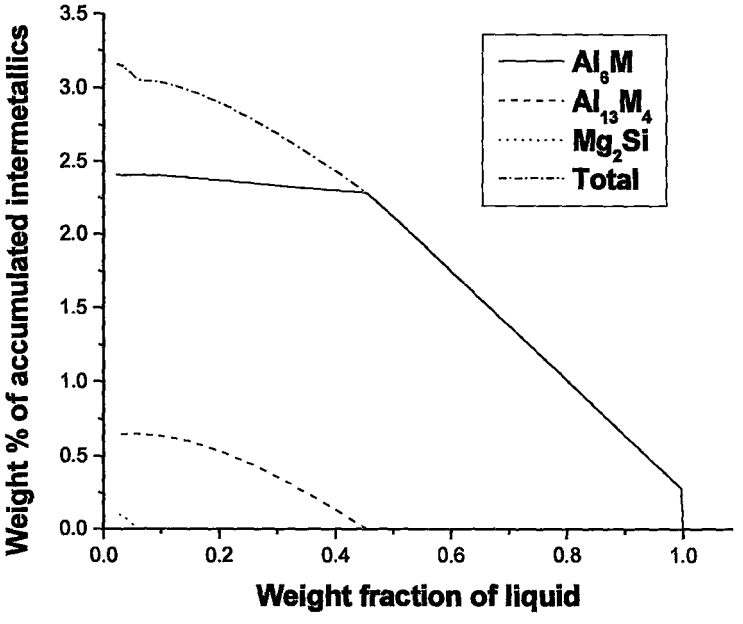

Figure 4.3: Accumulated amount of intermetallics in alloy I5 during solidification

Table 4.2: Sub-lattice model of the phases present in the given alloy systems

Name of phase	Sub-lattice model
Al_6M	$(Al)_6\ (Fe, Mn)_1$
$Al_{13}M_4$	$(Al)_{0.6275}\ (Fe, Mn)_{0.235}\ (Al, Si,Va)_{0.1375}$
Mg_2Si	$(Mg)_2\ (Si)_1$
AlM_β	$(Al, Zn)_{0.615}\ (Li, Mg)_{0.385}$

An analysis of figure Figure 4.2 and Figure 4.3 shows that in alloys containing negligible amount of Mn and Fe (i.e. I2), only $Al_{13}M_4$ phase is accumulated. There is no indication of accumulation of substantial amount of Al_6M phase in these alloys. On the other hand, in alloys with high Mn and Fe content, both $Al_{13}M_4$ and Al_6M phases are accumulated. The amount of accumulated $Al_{13}M_4$ phase in low Fe+Mn alloys is much smaller as compared to alloys with high Fe+Mn. It has been found that Mg_2Si is accumulated in all the alloys and amount of accumulation is not dependent on composition variation, which is not surprising. It was observed that Accumulated amount of Al_6M increases with increasing Fe+Mn content. Finally, based on the analysis it can be expected that if amount of Mg is not varied, total amount of accumulated second phase increases with increase in Fe+Mn content. Further calculations were carried out for these alloys to look at the stability of these accumulated second phase particles as well as the

possibility of formation of any other second phase precipitates at low temperatures when alloys are in solid state. The results of these calculations are presented in Figure 4.4 and Figure 4.5.

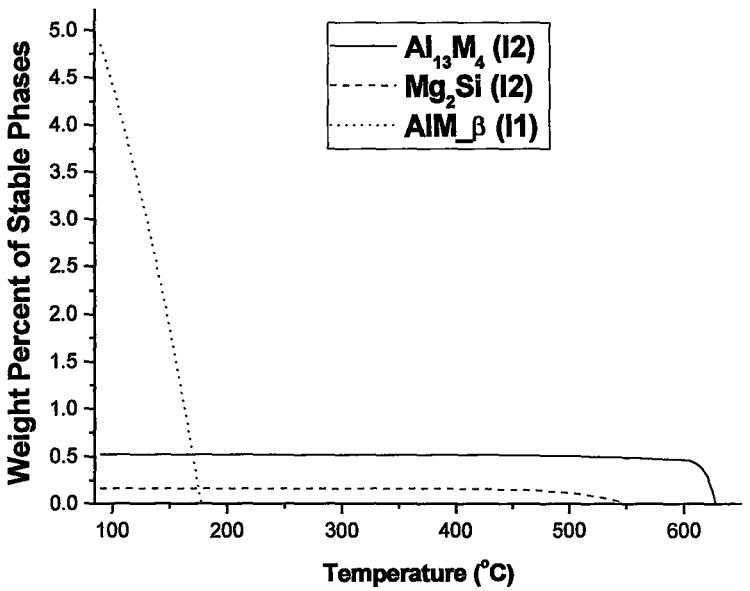

Figure 4.4: Stability of intermetallics as a function of temperature in alloy I2

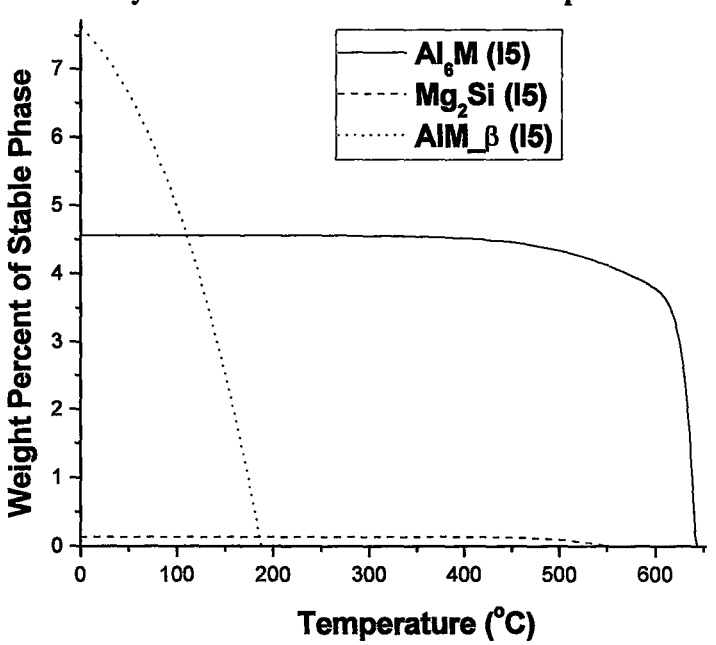

Figure 4.5: Stability of intermetallics as a function of temperature in alloy I5

Figure 4.4 and Figure 4.5 show the stability of various phases at different temperatures in systems with varying composition (alloys I2 and I5). An analysis of these calculations shows that in alloys with very low/ negligible Fe+Mn content (i.e. I2), only stable phases are $Al_{13}M_4$, Mg_2Si and AlM_β. However, when Fe+Mn content is higher (i.e. I5), there is no indication of stability of $Al_{13}M_4$ indicating to the possibility that $Al_{13}M_4$ is converted to Al_6M phase. It was observed that stability of phases like Al_6M, $Al_{13}M_4$ and Mg_2Si, is not affected much by temperature till 450°C but after 450°C, Al_6M and Mg_2Si start dissolving whereas $Al_{13}M_4$ remains stable (in very low Fe+Mn content alloys) till 600°C. At this point, it is important to mention that the presence of AlM_β phase, as shown in Figure 4.4 and Figure 4.5, is possible in the real 5xxx aluminum alloys but precipitation of AlM_β phase has sluggish kinetics.

The analysis presented in the preceding paragraph can be utilized to establish a homogenizing scheme for these alloys in such a manner that precipitation is avoided during recrystallization experiments. Since there is no indication of any significant dissolution of second phase particles upto 450°C, alloys can be solutionized at 450°C in order to be confident that all the precipitation is complete. However, it must be understood that for excluding the effect of precipitation, temperature of solutionizing must be equal to the highest temperature achieved in the experiment. Therefore, it is obvious to make sure that maximum temperature reached during annealing of deformed alloys for recrystallization experiments is not surpassing the 450°C barrier.

4.2: Uniformity of deformation

An essential part of study of recrystallization is to ensure that deformation during cold rolling is uniform throughout the specimens. During cold rolling of sheets, it is likely that the deformation is non-uniform throughout the cross section and more localized on the surface as compared to the center of the sheet. In this case, a situation may arise where recrystallization is complete at the surface whereas center of the specimen remains unrecrystallized during annealing of deformed specimen. In such a situation, results obtained will be biased and the study can not be considered as a true representative of a recrystallization process. To avoid such an unpleasant situation, uniformity of the deformation must be verified after cold rolling.

To determine the uniformity of deformation during cold rolling, micro-hardness tests were carried out on the L-T cross section (plane oriented perpendicular to the rolling plane and along the rolling direction) of the Al-Mg alloy specimens with different degrees of deformation (Figure 4.7). The Al-Mg alloy (composition (wt.%): Mg=2.98, Mn=0.002, Fe=0.07, Si=0.05) was first homogenized in salt bath at 450°C for 18 hours and then ice water quenched. The homogenized alloy was then cold rolled to different degrees of deformation i.e. 50%, 75%, 90%, 95% and 98% reduction in thickness as compared to original sample thickness. These samples were cut to small pieces using ISOMAT cutter. These small pieces were then mounted and manually polished in water to avoid any kind of heating of samples.

The micro-harness tests were carried out on these polished samples taking 10 measurements along each line near the edge and near the center of the specimen. In the

case of 98% deformed samples, hardness was measured near the center only due to the reason that sheet thickness was too small to take two measurements across the cross section. In this case, hardness measurements were done on two different samples and data were compared.

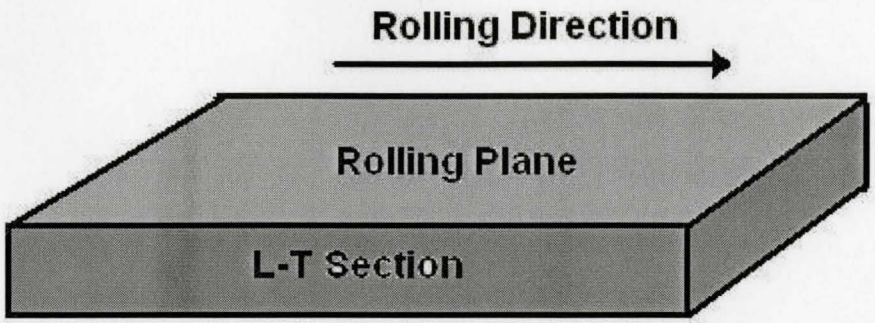

Figure 4.6: L-T section where hardness was measured

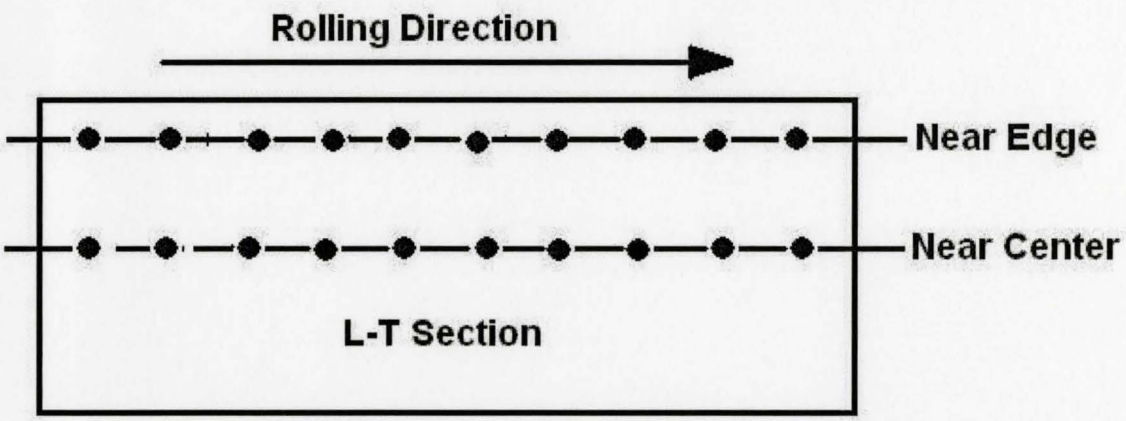

Figure 4.7: Positions of micro-hardness measurements on cold-rolled samples

To ensure the uniformity of deformation, following statistical hypotheses must be verified on the micro-hardness measurements along lines near the edge and near the center of the samples:

1) Are two variances corresponding to different lines equal to each other?
2) Are average hardness values along two different lines significantly different?

In order to verify the above-mentioned hypotheses, F-test (statistical test for equality of variance) and t-test (statistical test for the difference of means) were carried out.

t-test for Difference of Means:

Suppose we want to test that (a) two independent samples $x_i, i = 1,2,3.....,n_1$, and $y_j, j = 1,2,3.....,n_2$, have been drawn from the population with same means or (b) the two sample means $\bar{x}$ and $\bar{y}$ differ significantly or not.

Under the null hypothesis (H_o) that (a) samples have been drawn from the populations with same means, i.e., $\mu_X = \mu_Y$ or (b) the sample means $\bar{x}$ and $\bar{y}$ do not differ significantly, the statistic:

$$t = \frac{\bar{x} - \bar{y}}{S\sqrt{\left(\frac{1}{n_1} + \frac{1}{n_2}\right)}} \tag{4.1}$$

where, $\bar{x} = \frac{1}{n_1}\sum_{i=1}^{n_1} x_i$, $\bar{y} = \frac{1}{n_2}\sum_{j=1}^{n2} y_i$.

S^2 is the pooled variance which can be defined as: $S^2 = \frac{(n_1 - 1)S_x^2 + (n_2 - 1)S_y^2}{n_1 + n_2 - 2}$

where, $S_x^2 = \frac{1}{(n_1 - 1)}\sum_{i=1}^{n_1}(x_i - \bar{x})^2$, $S_y^2 = \frac{1}{(n_2 - 1)}\sum_{j=1}^{n_2}(y_j - \bar{y})^2$.

Here two following fundamental assumptions are made:

(i) Parent populations, from which the samples have been drawn are normal.

(ii) The population variances are equal, i.e., $\sigma_X^2 = \sigma_Y^2$.

Thus before applying t-test for testing the equality of means, it is theoretically desirable to test the equality of population variances by applying F-test.

F-test for Equality of Population Variances:

Suppose we want to test (a) whether two independent samples $x_i, i = 1,2,3.....,n_1$, and $y_j, j = 1,2,3.....,n_2$, have been drawn from the normal population with the same variance or (b) whether the two independent estimates of the population variances are homogeneous or not.

Under the null hypothesis (H_o) that (a) $\sigma_X^2 = \sigma_Y^2$ i.e., the population variances are equal or (b) two independent estimates of the population variances are homogeneous, the statistic F is given by:

$$F = \frac{S_1^2}{S_2^2} \tag{4.2}$$

where, S_1^2 is the larger of S_x^2 and S_y^2. If the variances are equal, this quantity has an F distribution with $n_1 - 1$ and $n_2 - 1$ degrees of freedom.

The statistical analysis of micro-hardness data is shown in Table 4.3. Statistical data analysis indicates that the variances and means of micro-hardness data, corresponding to position near edge and near center, are not significantly different at 95% confidence limit. The above conclusions have been drawn from the fact that computed **t** and **F** values for all the samples are less than the tabulated (critical) t and F values for given degrees of freedom at 95% confidence limit. In other words, there is no significant difference in the values of hardness in the cold rolled samples when the hardness near the

edge and at the center of the samples is compared. Therefore, it can be concluded that the deformation in the samples is uniform during the cold rolling deformation. A plot of mean hardness vs. true strain has been shown in Figure 4.8. Here, the true strain was calculated assuming the plain strain condition in the rolling process. Following formula was used to convert the percent reduction in thickness into true strain:

$$\varepsilon = \frac{2}{\sqrt{3}} \ln\left(\frac{t_o}{t}\right) \tag{4.3}$$

where, t_o = original thickness of sheet, t = thickness of sheet after deformation.

In order to calculate the standard error in measurements at a particular degree of deformation, following formula was used:

$$Er(\pm yEr) = \sqrt{\frac{\sum_{i=1}^{n}(\bar{h} - h_i)^2}{n(n-1)}} \bullet t_{0.95} \tag{4.4}$$

where n is the number of total measurements, $\bar{h}$ is the mean of total hardness measurements, h_i is the ith hardness value and $t_{0.95}$ is the critical tabulated t (student's t) value for (n-1) degrees of freedom at 95% confidence level. This equation has been used in this work to estimate standard error for all the hardness measurements and is shown as error bars on the graphs.

Table 4.3: Statistical data analysis of micro-hardness data (confidence level = 95%)

Degree of Deformation	50%	75%	90%	95%	98%
Sample #1	F-Test F = 4.13 FCritical = 6.39	F-Test F = 1.58 F Critical = 5.05	F-Test F = 2.99 F Critical = 3.18	F-Test F = 2.42 F Critical = 3.18	F-Test F = 2.18 F Critical = 3.18 t-Test t Stat = 0.54 t Critical = 1.73
	t-Test t Stat = 0.6 t Critical = 1.86	t-Test t Stat = 0.81 t Critical = 2.76	t-Test t Stat = 0.63 t Critical = 1.73	t-Test t Stat = 0.48 t Critical = 1.73	
Sample #2	F-Test F = 4.78 FCritical = 6.39	F-Test F = 1.68 F Critical = 3.44	F-Test F = 1.53 F Critical = 3.18	F-Test F = 1.49 F Critical = 3.18	
	t-Test t Stat = 1.1 t Critical = 1.86	t-Test t Stat = 0.28 t Critical = 1.75	t-Test t Stat = 1.04 t Critical = 1.73	t-Test t Stat = 0.54 t Critical = 1.73	

Figure 4.8 shows that during initial stages of deformation (50% to 90% reduction in thickness), hardness is increasing almost linearly but in the large deformations region a leveling off trend is observed. These results can be interpreted in terms of storage of amount of dislocations or dislocation density. It can be predicted from these results that in the initial stages of deformation (50% -90% reduction in thickness), dislocation density keeps on increasing with increasing degree of deformation significantly whereas in the region of high deformations a level of saturation of dislocation density is attained.

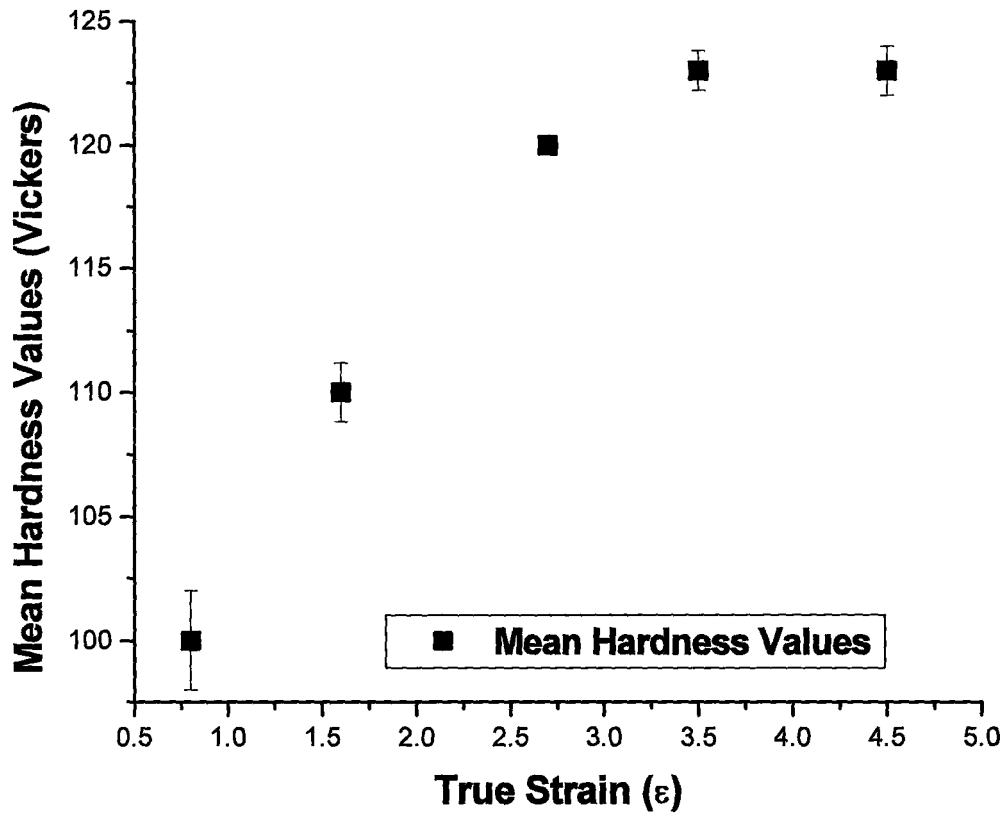

Figure 4.8:Mean hardness values as compared to true strain in cold rolled samples

4.3: Electrical Resistivity Measurements

The resistivity is a characteristic of metals and alloys, and depends on the temperature and pressure at any instant as well as on the chemical and physical state (Meaden 1965). The chemical state can be defined by the type and relative amount of the foreign impurity atoms present. The effect of impurity atoms on resistivity depends on quality, quantity and distribution within the lattice. On the other hand, physical state can be defined by the large strains in the lattice from dislocations, vacancies or interstitial atoms. The physical state depends on the previous history of the metal, which includes cold work, irradiation and annealing treatment etc.

The electrical resistivity of a metal is a property which is sensitive to changes of structure brought about by cold working and, therefore, a study of resistance changes during deformation and during annealing is capable of yielding information about the structure of plastically deformed metals (Broom 1954). To explain the large increase in resistivity due to deformation, it has been suggested that stacking faults associated with dislocations make an important contribution to the scattering of conduction electrons (Broom and Barrett 1953). However, a study on pure Al (Maeta 1968) showed that the dislocation resistivity due mainly to the core of a dislocation and to the strain field rather than a stacking fault ribbon.

According to Matthiessen's rule, the total resistivity of a crystalline metallic specimen is the sum of the resistivity due to thermal agitation of the metal ions of the lattice and the resistivity due to the presence of imperfections in the crystal. In other words, "The scattering of conduction electrons due to lattice vibrations is independent of

that due to lattice defects when these are present in small concentration" (Broom 1954). Thus, the measured resistivity can be expressed in the following way:

$$\rho_T = \rho_o + \rho_{iT} \tag{4.5}$$

The measured resistivity (ρ_T) is a function of temperature. On absolute zero, the resistivity approaches a value called residual resistivity (ρ_0, constant). The residual resistivity (ρ_0) arises from the presence of impurities, defects and strains in the metal lattice. Subtraction of residual resistivity from the measured resistivity, gives a value of the resistivity appropriate for a perfectly pure strain-free specimen. For a nonmagnetic metal, the temperature dependent resistivity thus obtained is called the ideal or intrinsic resistivity (ρ_{iT}). The intrinsic resistivity arises from interaction of the conduction electrons with the thermal vibrations of the ions of the lattice (Meaden 1965). The Matthiessen's rule is valid only if the impurity and phonon scattering are independent and relaxation time is isotropic. At room temperature or above, ρ_{iT} term dominates since scattering due to the lattice vibration is more than that due to the defect, but as temperature decreases scattering due to the thermal vibration becomes insignificant as compared to the defects.

The physical processes that determine the electrical resistivity of a concentrated metallic alloys are not easy to understand because of large number of possible contributions involved. The conduction electron scattering from thermally induced atomic displacements is not the only contribution. The other direct contributions may arise from atomic and magnetic disorder, strain and band structure effects. The magnitude

of such effects will be influenced by the homogeneity of the microstructure. It will depend specifically upon whether the spatial extent or 'scale' of the homogeneity is greater or less than the conduction electron mean free path.

Electrical resistivity is very sensitive to the dislocation density, small-scale precipitates and solute content (Verdier 1997, Barghout 1996). Therefore, it is possible to figure out the change in solute content from measured changes in resistivity. Very small-scale precipitates increase the resistivity whereas larger precipitates decrease the resistivity due to depletion of the solid solution.

In case of Al-Mg alloys, it is believed that the largest contribution to the extra resistivity comes from the solute Mg atoms and the dislocations. The resistivity contribution due to Mg atoms is sensitive to the position of Mg atoms depending upon whether they are segregated to the core of dislocations in the form of solute atom clusters or released in the Aluminum matrix. In contrast, the resistivity contribution due to dislocations is sensitive to overall dislocation density rather than arrangement of the dislocations (Schrank 1980). Since it has been found that majority of the Mg atoms remain dissolved in the matrix and only a slight fraction (approx. 0.05) of the total Mg concentration is segregated to dislocations, it can be assumed that changes in the resistivity during annealing of deformed material reflect the changes in the dislocation density predominantly (Verdier 1997).

Electrical resistivity changes from the cold worked state to annealed state are frequently employed to follow recrystallization. The normal experimental approach involves isothermal and isochronal annealing of deformed samples and then prompt

quenching (Maeta 1968, Yang 1982, Mathew 1984, Inakazu 1987, Gaber 1993, Verdier 1997, Esmaeili 2000, Khan 2003, Esmaeili 2005, Sarkar 2006). Then electrical resistivity of the specimens is measured at either room (Maeta 1968,Yang 1982, Inakazu 1987, Verdier 1997, Sarkar 2006) or liquid N_2 temperature (Maeta 1968, Esmaeili 2000, Esmaeili 2005). Resistivity data are usually presented in the form of ρ vs. T curves (Maeta 1968, Mathew 1984, Inakazu 1987, Gaber 1993, Verdier 1997, Khan 2003, Esmaeili 2000, Esmaeili 2005, Sarkar 2006). In some cases, data are represented as $\left(\frac{\Delta\rho}{\rho_o}\right)$ vs. T curves (Nes 1976, Yang 1982, Janecek 2004). Where $\Delta\rho(T) = \rho_d(T) - \rho_o(T)$, $\rho_d(T)$= resistivity of deformed specimen at temperature T, $\rho_o(T)$= resistivity of annealed specimen at temperature T

It is normally found that the fractional difference in resistivity $\Delta\rho$ from the completely annealed value will remain constant at low annealing temperatures before the onset of recovery In the case where $\Delta\rho$ is correlated with the stored energy released, it is usually found that $\Delta\rho$ decreases as the stored energy release begins. If the recovery process is slow, $\Delta\rho$ change may appear like plateau type or a gradually increasing type. If recovery is fast with the increase in temperature, a sharp decrease in $\Delta\rho$ is generally observed. With the occurrence of a stored energy release peak during recrystallization, $\Delta\rho$ decreases rapidly and becomes zero at the completion of recrystallization.

In contrast to the conventional resistivity measurements, a new and much simpler approach was devised for this work. Resistivity of a long sample with a small cross

section area (usually, $70 \times 2 \times 0.2\ mm^3$ strips were employed) was continuously measured while the sample was heated from room temperature to 400°C. Data obtained from *in-situ* resistivity measurements were treated to extract information about the onset and completion of recrystallization.

Specimens of dimension of 70mm x 2mm x 0.2mm were prepared from deformed samples for electrical resistivity measurements using ISOMAT cutter. However, the length and thickness of individual samples varied somewhat. Four-point resistivity measurement method was used to measure resistivity of these specimens. The circuit diagram of experimental set-up for 4-point resistivity measurements is shown in Figure 4.9. Resistivity of these specimens was measured under the condition of constant heating rate in the temperature range from room temperature to 400°C. Data were collected at the heating rate 5°C/min.

For resistivity measurements, molybdenum wire was chosen as potential measuring wire whereas tungsten wire was chosen as current supplying wire. Choice of these wires was based on their excellent heat-resistant properties. These wires, along with the thermocouple wires, were passed through 6-bore ceramic tube to form a resistivity-measuring probe. One end of the Mo and W wires was spot welded on the sample and the other end soldered to connectors as shown in Figure 4.10 and Figure 4.11. The thermocouple was positioned in such a way that it was touching the sample surface for real time temperature measurement.

The reason for introducing a 0.1 ohm resistor to the circuit was to measure the current flowing in the circuit based on the following equation:

$$I = \frac{V_{0.1\Omega}}{0.1} \tag{4.6}$$

Therefore, the resistance of the sample can be calculated as:

$$R = \frac{V_{sample}}{I} \tag{4.7}$$

where, $V_{0.1\Omega}$ is the potential drop across the resistor (Volts), V_{sample} is the potential drop across the sample (Volts), R is the resistance of the given sample (Ohm), and I is the current flowing through the circuit (Amp). Thus, the resistivity of the sample can be calculated as:

$$\rho = \frac{RA}{l} \tag{4.8}$$

where, R is the resistance of the sample (Ohm), A is the cross-sectional area of the sample (m^2), ρ is the resistivity of the sample (ohm-m) and l is the length between potential electrodes (m).

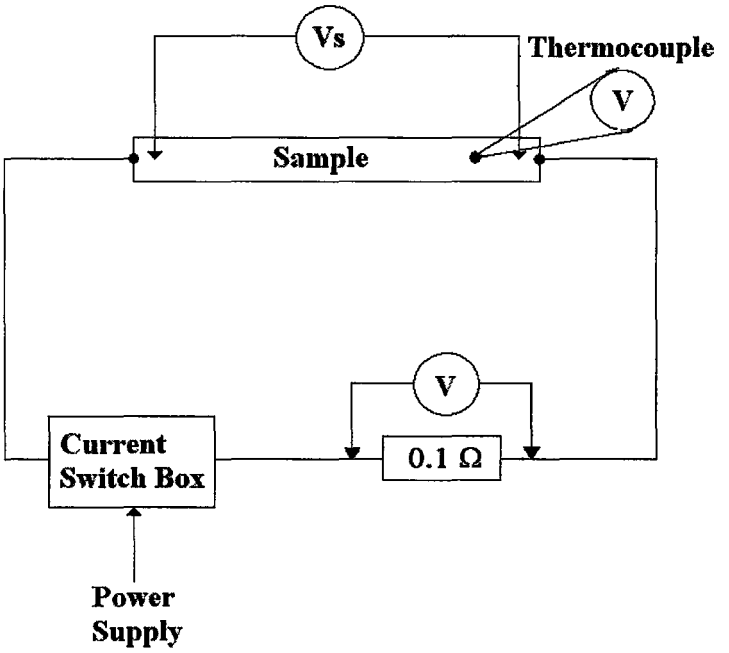

Figure 4.9: Circuit diagram of the experimental set-up for 4-point resistivity measurements

Since the resistivity measurement was aimed to find the onset and finish point of recrystallization, the deformed sample was first heated from room temperature to 400°C at a constant heating rate and then cooled to room temperature by furnace cooling. A thermal emf will be generated during this process and affect the accuracy of resistivity measurements, which is supposed to contribute to the error in the determination of desired characteristic temperatures. For canceling out this thermal emf, the current was reversed during each potential measurement. In order to eliminate the thermal effects, a current switch box was provided in the setup to change the current direction in the circuit.

If the voltage measured in the forward current direction is V1, and in the reverse current direction is V2, then

$$V1 = V_R + V_{th} \tag{4.9}$$

$$V2 = -V_R + V_{th} \tag{4.10}$$

where, V_R is the voltage drop across the sample and V_{th} is the thermal emf. Sign of thermal emf is not changed in the above equations because of the fact that it is independent of the direction of the current.

From the equations (4.9) and (4.10), we get:

$$V1 - V2 = 2V_R \quad \text{And} \quad \frac{V_R}{I} = \frac{V1 - V2}{2I} \tag{4.11}$$

Thus, the actual sample resistance in one reading can be calculated as:

$$R = \frac{V1 - V2}{2I} \tag{4.12}$$

Current, potential and temperature data were collected automatically in a PC by using LABVIEW software. The frequency of data collection was 20 readings/second. The standard deviation of the data was in the order of 1E-6 indicating the high accuracy of the resistance measurements. The uncertainty in temperature measurements (ΔT) was estimated around 2°C. The complete experimental setup and interface of the data collection software is shown in Figure 4.12, Figure 4.13 and Figure 4.14. This instrument was developed and programmed by Dr. Marek Niewczas, Department of Materials Science and Engineering, McMaster University. He is the person who introduced such kind of *in-situ* resistivity measurement technique in the department for the first time.

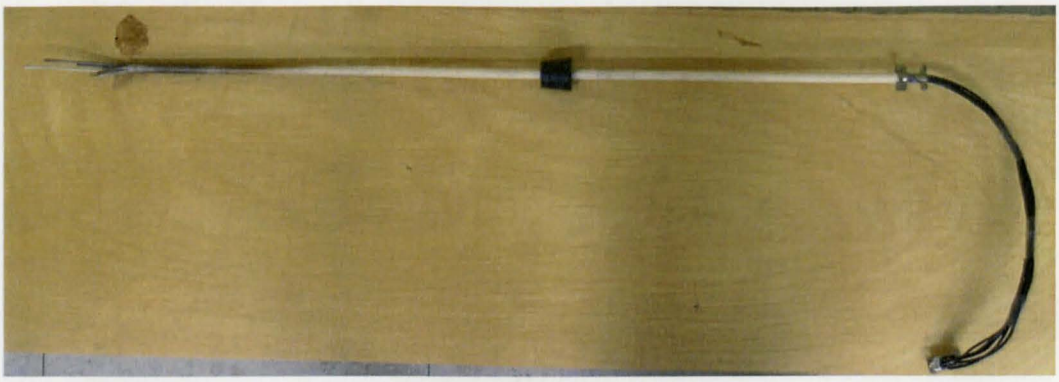

Figure 4.10: Resistivity measuring probe

Figure 4.11: Sample mounting on the probe

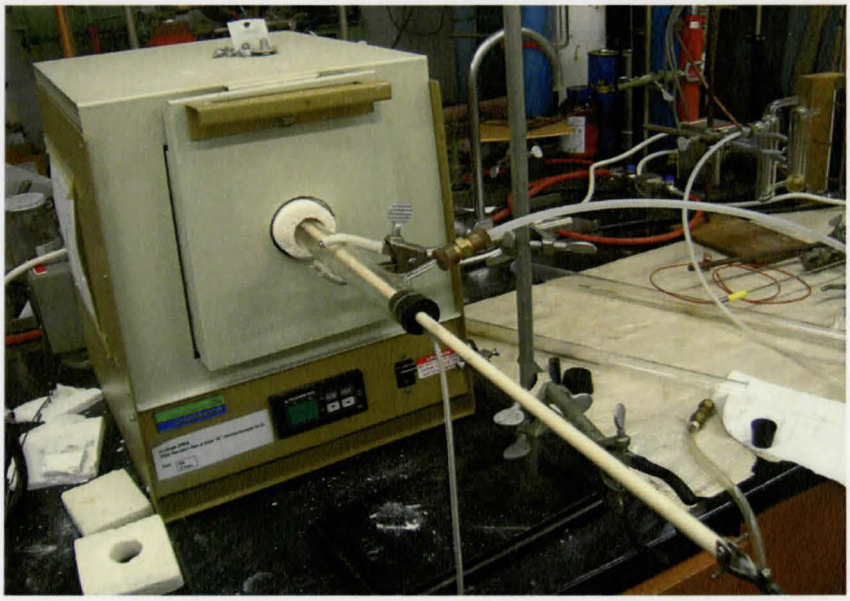

Figure 4.12:Furnace loaded with resistivity probe

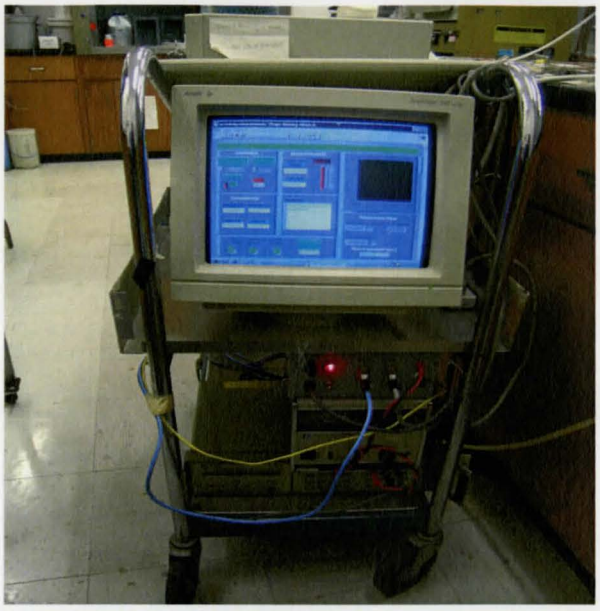

Figure 4.13: Data acquisition unit including controllers and PC

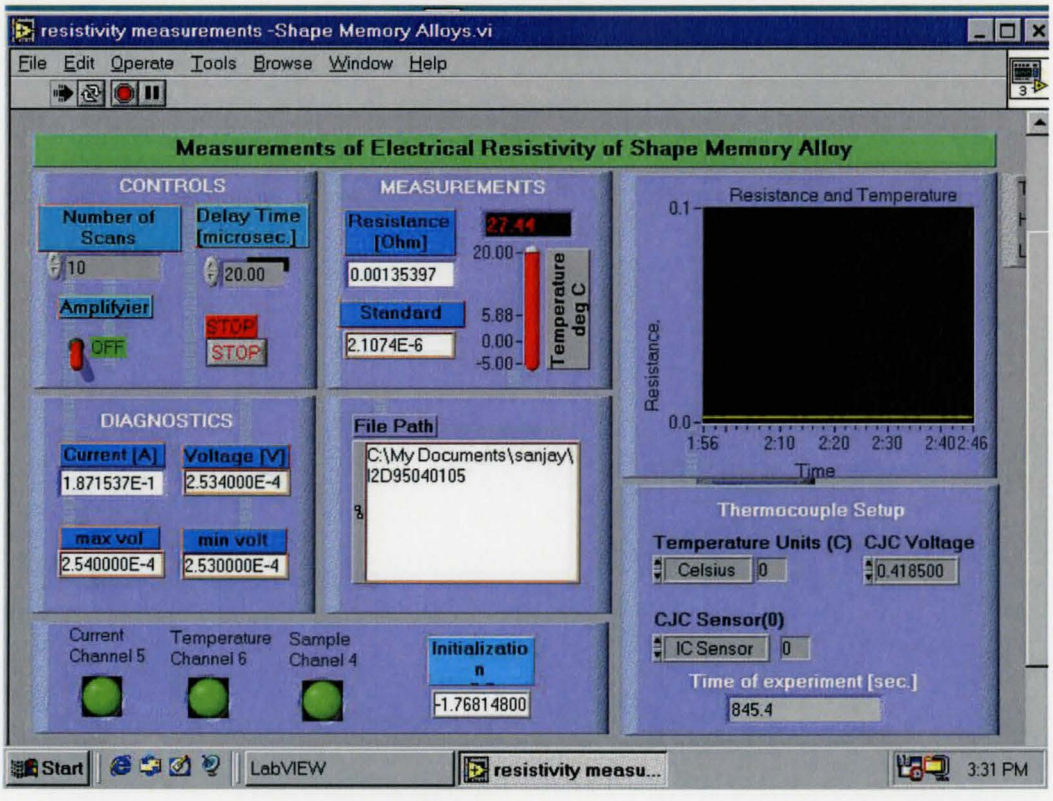

Figure 4.14: Resistance data collection interface (LabView)

Chapter 5: Spline filtering

Raw data obtained from *in-situ* electrical resistivity measurements increase with temperature almost linearly. However, it is intended to extract useful data about recrystallization from these almost straight lines. If there is any change in the material property during heating of the samples, these changes will be reflected as a deviation of slope. Since these data are not smooth and continuously differentiable, it is impossible to differentiate these raw resistivity data ($R(T)$) profiles. Therefore, some smoothing of these $R(T)$ profiles is required to make these profiles differentiable in order to observe the change in slope with temperature. For smoothing and robust numerical differentiation of experimentally obtained $R(T)$ profiles, a spline-based smoothing and robust numerical differentiation procedure is required. Although detailed processing and interpretation of these $R(T)$ profiles will be discussed and explained in the next chapter, some fundamental concepts of spline filtering of noisy experimental data have been presented in this chapter keeping in mind the importance of spline-based data filtering in this work.

In this section, a problem of a robust numerical differentiation is considered. More specifically, it is assumed that there is a table representing experimental results:

$$x_i, \Delta x_i, y_i, \Delta y_i, i = 1, \ldots, n \tag{5.1}$$

where x_i and Δx_i characterize experimental conditions (in the case of in situ measurements of electrical resistance, x is temperature T), y_i and Δy_i are observed quantities and their uncertainties (in our case, y is resistance R). It is assumed that $x_i < x_{i+1}$. Let us assume that the most important features of the process under

investigation can be understood not from the experimental response per se (i.e. not from how y changes with x) but from its derivative (i.e. from how the slope of the experimental dependency changes with x). At first glance, the problem of estimating the derivatives of the function known at discrete points is trivial since nothing refrains one from trying divided differences. Having, for instance, x_i, y_i and x_{i+1}, y_{i+1}, one can calculate the derivative in the point $(x_i + x_{i+1})/2$ as

$$(y_{i+1} - y_i)/(x_{i+1} - x_i) \tag{5.2}$$

If due to some reasons, the derivatives must be evaluated not between the experimental points but directly at these points, one can easily do this except for the first and the last point. Let us consider three points x_{i-1}, y_{i-1}, x_i, y_i and x_{i+1}, y_{i+1}, $i \neq 1$ and $i \neq n$. Knowing that the derivative at the point $(x_i + x_{i-1})/2$ is equal to $(y_i - y_{i-1})/(x_i - x_{i-1})$ and that the derivative at the point $(x_{i+1} + x_i)/2$ is equal to $(y_{i+1} - y_i)/(x_{i+1} - x_i)$, one easily arrives at the expression for the derivative in x_i:

$$\frac{\dfrac{y_{i+1} - y_i}{x_{i+1} - x_i} - \dfrac{y_i - y_{i-1}}{x_i - x_{i-1}}}{\dfrac{x_{i+1} + x_i}{2} - \dfrac{x_i + x_{i-1}}{2}}\left(x_i - \frac{x_i + x_{i-1}}{2}\right) + \frac{y_i - y_{i-1}}{x_i - x_{i-1}}$$

Many other schemes can be invented. For example, one can estimate the derivative at x_i by using two adjacent points with numbers $i-1$ and $i+1$ for building a quadratic polynomial and then associating the value of the derivative with a corresponding coefficient. In reality, however, a majority of methods will never work. For understanding why, let us compare Figure 5.1 and Figure 5.2. The first one represents

simulated experimental results, which are free of random noise. It can be seen that the estimation of derivative based on (5.2) is quite reasonable. The second picture represents the case when a slight Gaussian noise is added to data points. While the changes in the function are hardly noticeable, the derivative values (which, again, are computed by making use of (5.2)) change dramatically. Inevitable noise in experimental data is a hangman for all unsophisticated methods (i.e. ones based on common sense rather than on an rigorous mathematical and algorithmic analysis) of numerical differentiation.

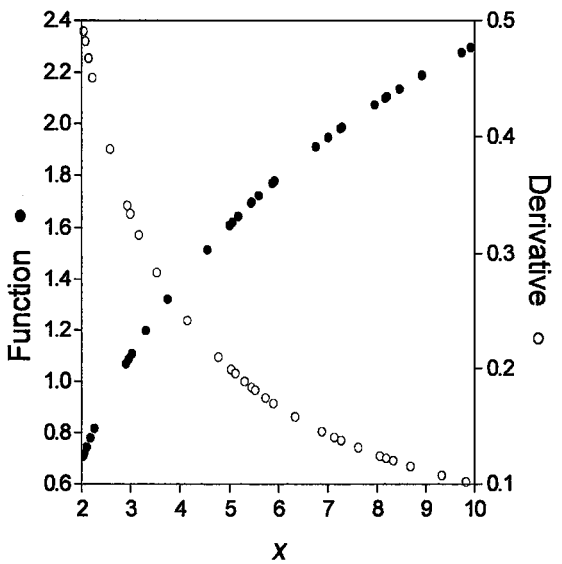

Figure 5.1: Simulated experimental results, free of noise

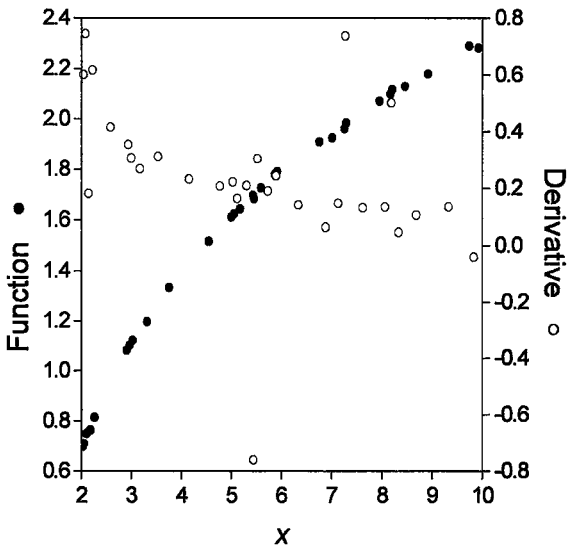

Figure 5.2: Simulated experimental results burdened with Gaussian noise and estimation of their first derivative.

Although it is intuitively clear that the derivative in Figure 5.2 is poorly evaluated, the following argument can be put forward. It can be declared that everything is fine with the derivatives merely because a noisy nature of experimental data is reflected in their values. This line of reasoning cannot be rejected if it is believed that the

table (5.1) is the ultimate and final characterization of the $y(x)$ dependency investigated. This table is a quantitative representation of what was studied, indeed. However, one should realize that although the results of measurements are presented in a discrete form, there is no doubt that y is a continuous (and maybe continuously differentiable or maybe even twice continuously differentiable) function of x. As such, it is characterized not only by its values at points at which the experiment was conducted. It is also characterized by such fundamental properties as its sign as well as by signs of its first and second derivative. Let us realize that even if data points shown in Figure 5.2 are burden with experimental errors, there is little doubt that this function increases with time (i.e. that $dy/dx > 0$) and that it is upwardly convex (i.e. that $d^2y/dx^2 < 0$). Something is awfully wrong with the estimation of the derivative shown in Figure 5.2 not because they behave erratically but because at two values are negative. As Figure 5.3 stipulates, the situation will become even more intolerable if it is attempted to evaluate the second derivative by using divided differences.

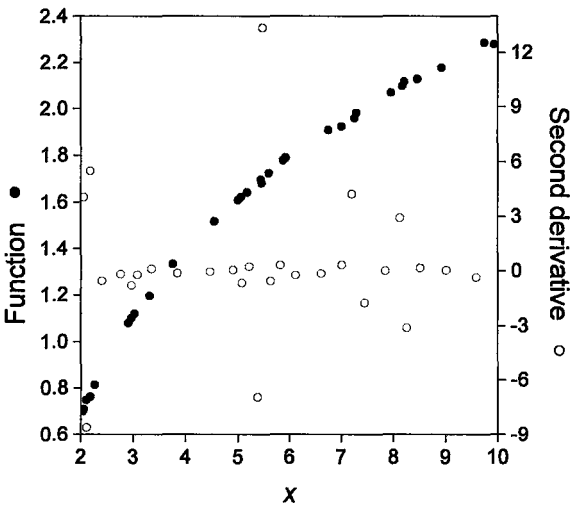

Figure 5.3: Estimation of second derivative of simulated noisy data

Now it is time to remember that the dependency under investigation is a smooth one. A degree of smoothness is determined by how many times this dependency can be continuously differentiated. It seems reasonable not to employ the experimental quantities (5.1) directly, but to utilize them for building an analytical expression describing the discrete observations. Needless to mention that this problem is not a new one and usually it is dealt via the least-squares technique. Either a physically feasible or mathematically convenient function f containing unknown parameters $\vec{C}$ is chosen. Then statistically optimal values of these adjustable parameters are found by solving the following minimization problem:

$$\sum_{i=1}^{m} \omega_i \left(y_i - f\left(x_i, \vec{C}\right) \right)^2 \rightarrow \min\left(\vec{C}\right) \tag{5.3}$$

where the statistical weight ω_i can be identified (at least approximately) with the experimental error: $\omega_i = 1/\left(\Delta y_i\right)^2$. It should be realized that the criterion "a sum of weighted deviations must be minimal" minimization of (5.3) is based upon is related only and exclusively to the accuracy of fitting of experimental data. It does not guarantee that the function $f\left(x, \vec{C}_{\text{optimal}}\right)$ will posses a shape implied by experimental data. Let us consider a particular example when polynomial is chosen as $f\left(x, \vec{C}\right)$:

$$f\left(x, \vec{C}\right) = P_n\left(x, \vec{C}\right) = \sum_{i=0}^{n} C_i x^i \tag{5.4}$$

Even though a noise level is moderate, it is quite possible that there is one or several "bad points" (this case can be modeled by adding a mixture of two Gauss noises

with very different variances to experimental data). It is methodologically incorrect to eliminate outstanding observations since for the normal distribution $P\left(\frac{|x-\mu|}{\sigma} \geq 3\right) \approx 0.01$, and 0.01 is definitely not a very small number. Trying to satisfy the accuracy-based criterion, one will try to increase n, i.e. a number of coefficients in (5.4). The polynomial will be badly affected by these "abnormal" (actually quite normal!) experimental data points. For understanding what will happen, let us recall that polynomials are global approximants. From the mathematical angle, this means the following. Let us solve (in a statistical sense, indeed) an over determined system of linear equations:

$$\begin{cases} C_0 + C_1 x_1 + \ldots + C_n x_1^n = y_1 \\ C_0 + C_2 x_2 + \ldots + C_n x_2^n = y_2 \\ \ldots \\ C_0 + C_1 x_m + \ldots + C_n x_m^n = y_m \end{cases} \tag{5.5}$$

The system (5.5) can be written in the matrix form as:

$$\underbrace{\begin{pmatrix} 1 & x_1 & \cdots & x_1^n \\ 1 & x_2 & \cdots & \vdots \\ \vdots & \cdots & \ddots & \vdots \\ 1 & x_m & x_m^2 & x_m^n \end{pmatrix}}_{[m\times(n+1)]} \times \underbrace{\begin{pmatrix} C_0 \\ C_1 \\ \vdots \\ C_n \end{pmatrix}}_{[(n+1)\times 1]} = \underbrace{\begin{pmatrix} y_1 \\ y_2 \\ \vdots \\ y_m \end{pmatrix}}_{[m\times 1]}$$

or simply as

$$\mathbf{A}C = y \tag{5.6}$$

where $\mathbf{A}$ is the so-called fundamental matrix. Before solving (5.6), let us account for statistical weights. This can be done if both sides are multiplied by a diagonal $[m \times m]$ matrix of weights:

$$\mathbf{W}\mathbf{A}C = \mathbf{W}y \tag{5.7}$$

Now let us multiply both sides of (5.7) by the transposed matrix $\mathbf{A}^T$:

$$\mathbf{A}^T\mathbf{W}\mathbf{A}C = \mathbf{A}^T\mathbf{W}y$$

The symmetric matrix $\mathbf{A}^T\mathbf{W}\mathbf{A}$ is a dense matrix, in which non-diagonal zeros may happen only occasionally. In other words, it does not possess the band structure, which allows one to call a polynomial a global approximant. In contrast to polynomials, splines are local approximants. An outstanding point will badly affect the shape of the polynomial not only because it will gravitate to this point, but because its influence will be felt in a wide region. Consequently, a "wavy" polynomial will have a shape resulting in a dubious estimation of the first derivative.

It can be attempted to help a polynomial to have a shape prompted by experimental data. Let us imagine that the signs of the slope and curvature at each point are known. In this case, the minimization problem

$$\sum_{j=1}^{m} \omega_i \left(y_j - \sum_{i=0}^{n} C_i x_j^i \right)^2 \rightarrow \min(\vec{C})$$

should be solved under the following "topological conditions":

$$\sum_{i=1}^{n} i C_i x_j^{i-1} \text{ is } > 0 \text{ or } < 0 \text{ depending on slope's sign} \tag{5.8}$$

$$\sum_{i=1}^{n} i(i-1)C_i x_j^{i-2} \text{ is } >0 \text{ or } <0 \text{ depending on curvature's sign} \tag{5.9}$$

It seems that such an amendment is somewhat doable since here one is dealing with a linear objective function and linear inequality constraints. However, it is too laborious to analyze an array of experimental data and assign correct signs to slopes and curvatures. Moreover, one seldom knows exact locations of extrema and inflection points, which may make such assignment impossible. It should also be realized that polynomials are not a panacea, that they cannot be applied to describing many dependencies encountered in practice. If, for instance, a dependency demonstrates an asymptotic behavior at $x \to \infty$, a polynomial is not useful since when the argument tends to infinity, $P_n(x) \to \infty C_n/|C_n|$. For dependencies with asymptotes and for many other cases, a polynomial fractional function $P_m(x)/P_n(x)$ is frequently used. Building of such a function is a non-linear least-squares problem. Needless to mention that for polynomial fractional functions conditions similar to (5.8) and (5.9) become non-linear inequalities! In contrast to their exact location, numbers of extrema and inflection points are relatively easy to deduce from experimental observations if the observations are not too noisy. For clarifying the last point, let us analyze Figure 5.4.

Sixty four uniformly distributed random values were generated with the $(0,10)$ interval. At these points, the values of the function $x^2 \exp(-x^2/8) + x/8$ were calculated. These quantities are presented by filled circles in Figure 5.4. Although it is difficult to judge where exactly extrema and inflection points are located, there is little or no doubt that the "experimental dependency" has two extrema (one maximum and one minimum)

and two inflection points. If an analytical representation reproduces the shape of the experimental dependency, i.e. these known numbers, it can be hoped that the analytical expression will provide us with a reasonable estimation of the first derivative. An approximation reproducing known numbers of extrema (let us denote it as E) and inflection points (B) can be named isogeometric approximation.

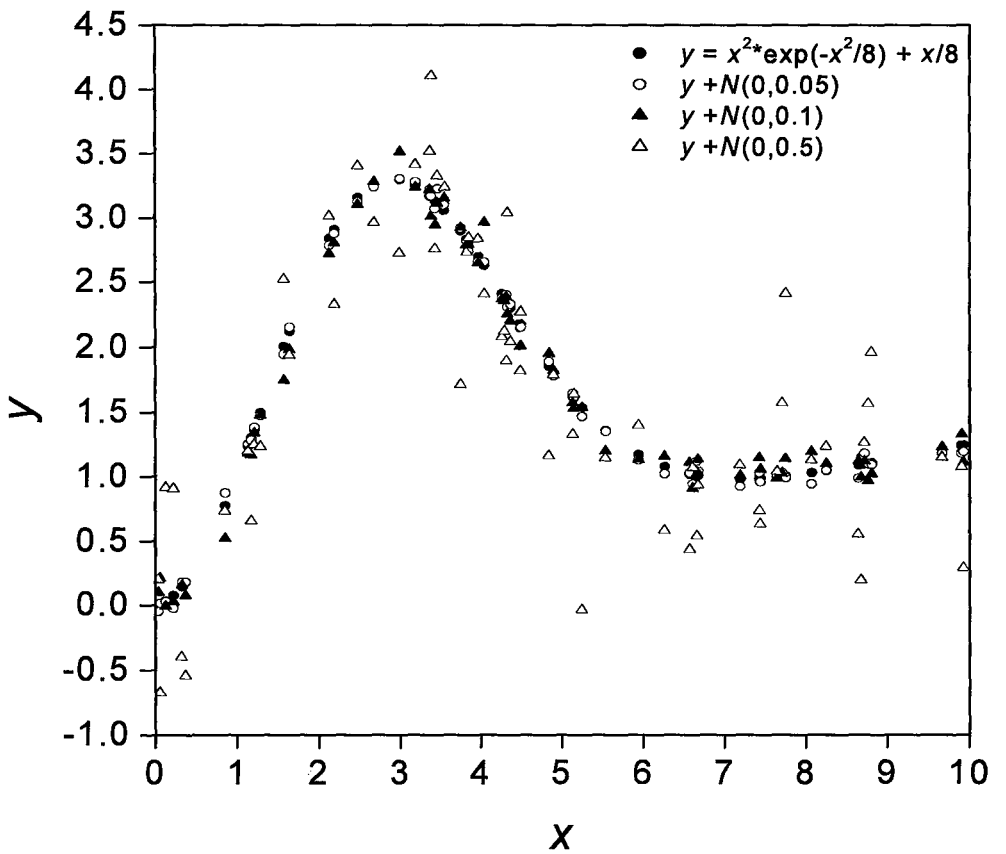

Figure 5.4: Showing that even with considerable amount of noise in data, number of inflection points and extrema can still be deduced.

Let us return to the problem (5.3) and imagine that $f\left(x,\vec{C}_{\text{optimal}}\right)$ has an excessive number of extrema and/or inflection points, i.e. that it is too wavy. Clearly, the function $f\left(x,\vec{C}\right)$ must be smoothed. Imagine a piece of copper wire. If it is bent, then it is clear what to do, is it not? The same method can be utilized for "straightening" the function if the following optimization problem is solved instead of (5.3)

$$(1-p)\sum_{i=1}^{n}\omega_i\left(y_i-f\left(x_i,\vec{C}\right)\right)^2+p\int_{x_1}^{x_n}\left(f''\left(z,\vec{C}\right)\right)^2dz\rightarrow\min\left(\vec{C}\right) \tag{5.10}$$

where p is a dimensionless smoothing parameter, $0\le p<1$

Before making the next step, let us notice a shortcoming in (5.10). While the first summands in the LHS of (5.10) is dimensionless, the second summand is in general not. For addressing this complication, let us build the function with $p=0$ and rewrite (5.10) as follows:

$$(1-p)\sum_{i=1}^{n}\omega_i\left(y_i-f\left(x_i,\vec{C}\right)\right)^2+p\frac{\int_{x_1}^{x_n}\left(f''\left(z,\vec{C}\right)\right)^2dz}{\left(\int_{x_1}^{x_n}\left(f''\left(z,\vec{C}\right)\right)^2dz\right)_{p=0}}\rightarrow\min\left(\vec{C}\right) \tag{5.11}$$

If the integral in the denominator of (5.11) is equal to 0, then $f\left(x,\vec{C}\right)$ is a straight line, which cannot be straightened.

The second summand in the LHS of (5.11) can be identified with an elastic energy of the function. If $p=0$, then only an accuracy of fitting is important; a severity of function bending is immaterial and is not accounted for. By increasing p, one is

constructing increasingly smooth functions. Ultimately, when $p \to 1$, the function degenerates into an almost straight line. It is instructive to notice that p cannot be equal to unity. If $p = 1$, then the solution is not unique since any straight line (regardless of its slope!) will be a solution of the optimization problem (5.11).

It can be hoped that by manipulating with p one can find such a smoothing parameter that minimization of (5.11) will result in isogeometric approximation. However, before starting playing with p, it is necessary to point to a class of suitable functions used as $f(x, \vec{C})$. Actually, it is much easier to outline types of functions, which are not suitable for this purpose. Both polynomials and polynomial fraction functions are examples of such "inconvenient" functions because their utilization in (5.11) will result in a non-linear problem. An analysis of literature reveals that cubic splines is the only one class of functions, which can seamlessly be used.

Two types of cubic splines are known – interpolating and smoothing. Although interpolating splines are not used in the present work, it is instructive to start with them for getting a better understanding of what splines are and for introducing a specific terminology.

A spline $Sp(x)$ is defined on a mesh of knots $x_1, x_2, \ldots, x_n$, $n \geq 2$, $x_i < x_{i+1}$. On each interval $[x_i, x_{i+1}]$, $i = 1, \ldots, n-1$, the spline is a cubic polynomial:

$$Sp_i(x) = C_{i1} + C_{i2}x + \frac{C_{i3}}{2}x^2 + \frac{C_{i4}}{6}x^3 \qquad (5.12)$$

Totally, there are $4(n-1)$ coefficients to be calculated. Since the spline interpolates data, one has $2(n-1)$ equations:

$$Sp_i(x=x_i)=y_i, Sp_i(x=x_{i+1})=y_{i+1}, i=1,\ldots,n$$

In fact polynomials are "glued" in inner knots in such a way, that both the first and second derivatives are continuous brings additional $2(n-2)$ equations. Totally, one has $2(n-1)+2(n-2)=4(n-1)-2$ equations, from which $4(n-1)$ are to be calculated. Various boundary conditions can be used for providing two missing equations. If there are reliable estimations of the first or second derivative in two knots, they can be used directly. However, it is advantageous to use the values of derivatives in the first and last knots since in this case a corresponding matrix of a system of equations is tridiagonal with diagonal dominance. If it is impossible or too computationally expensive to estimate the derivatives, then the following so-called "not-a-knot" conditions:

$$Sp_1'''(x=x_2^-)=Sp_2'''(x=x_2^+) \tag{5.13}$$

$$Sp_{n-2}'''(x=x_{n-1}^-)=Sp_{n-1}'''(x=x_{n-1}^+) \tag{5.14}$$

Employing the conditions (5.13) and (5.14) again result in a tridiagonal matrix with diagonal dominance, which is exceptionally convenient computationally.

Although ready-to-use subroutines for building interpolating splines can be found in many software libraries including IMSL and HSL, it seems necessary to present a simple and very elegant algorithm of constructing interpolating cubic splines for readers who do not want to rely upon a black box mercy.

The second derivative of the cubic spline is a linear function on $[x_i, x_{i+1}]$:

$$Sp''(x) = m_{i+1}\frac{x - x_i}{h_i} + m_i\frac{x_{i+1} - x}{h_i}, i = 1,...,n-1 \tag{5.15}$$

where m_i and m_{i+1} are the second derivatives in knots x_i and x_{i+1}, correspondingly, and $h_i \equiv x_{i+1} - x_i$. Expression (5.15) automatically provides the continuity of the second derivative in the inner knots $x_2,...,x_{n-1}$. To obtain the expression for spline itself, Expression (5.15) has to be integrated twice:

$$Sp(x) = \frac{m_{i+1}}{6h_i}(x - x_i)^3 + \frac{m_i}{6h_i}(x_{i+1} - x)^3 + \frac{C_{i+1}}{h_i}(x - x_i) + \frac{C_i}{h_i}(x_{i+1} - x) \tag{5.16}$$

where C_i and C_{i+1} are integration constants. They can be determined using known values of function in knots x_i and x_{i+1}:

$$Sp(x_i) = f_i = \frac{m_i h_i^2}{6} + C_i \Rightarrow C_i = f_i - \frac{m_i h_i^2}{6} \tag{5.17}$$

$$Sp(x_{i+1}) = f_{i+1} = \frac{m_{i+1} h_i^2}{6} + C_{i+1} \Rightarrow C_{i+1} = f_{i+1} - \frac{m_{i+1} h_i^2}{6} \tag{5.18}$$

Substituting expressions (5.17) and (5.18) into (5.16) and then differentiating the expression obtained, one arrives at the following representation of the first derivative on $[x_i, x_{i+1}]$:

$$Sp'(x) = \frac{m_{i+1}}{2h_i}(x - x_i)^2 - \frac{m_i}{2h_i}(x_{i+1} - x)^2 + \left(\frac{f_{i+1}}{h_i} - \frac{m_{i+1} h_i}{6}\right) - \left(\frac{f_i}{h_i} - \frac{m_i h_i}{6}\right) \tag{5.19}$$

The requirement that the first derivative of spline must be continuous in the inner knots leads to the following system of linear equations with respect to $\vec{m}$:

$$m_{i-1}\frac{h_{i-1}}{6} + m_i\left(\frac{h_{i-1}}{3} + \frac{h_i}{3}\right) + m_{i+1}\frac{h_i}{6} = \frac{f_{i-1}}{h_{i-1}} - f_i\left(\frac{1}{h_{i-1}} + \frac{1}{h_i}\right) + \frac{f_i}{h_i}, i = 2,...,n-1 \tag{5.20}$$

While the total number of unknowns is equal to *n*, the system (expression (5.20)) contains only *n-2* equations. It depends on the nature of the problem as to which two additional conditions are to be added. In a case where accurate estimations of the first and second derivatives are available, a pair of their values is used as such conditions. Otherwise, the so-called "not-a-knot" conditions are employed.

$$\begin{aligned} Sp'''(x_2-0) &= Sp'''(x_2+0) \Rightarrow m_1-2m_2+m_3=0 \\ Sp'''(x_{n-1}-0) &= Sp'''(x_{n-1}+0) \Rightarrow m_{n-2}-2m_{n-1}+m_n=0 \end{aligned} \tag{5.21}$$

In both cases of known derivatives or "not-a-knot" conditions, two equations can be added to the system (equation (5.20)) in such a manner that its matrix remains tridiagonal and with diagonal dominance. The latter means that it is positive definite which, in turn, prompts that an extremely simple, fast and robust algorithm can be used for building the cubic spline.

Now let us turn our attention to smoothing splines. A smoothing cubic spline is also defined on a mesh of knots $x_1, x_2, \ldots, x_n$, $n \geq 2$, $x_i < x_{i+1}$. Again, within each interval $[x_i, x_{i+1}]$ spline is a cubic polynomial, which means that a total number of coefficients to be determined is equal to $4(n-1)$. Continuity of spline and its first and second derivatives in inner knots $x_2, \ldots, x_{n-1}$ results in $3(n-2)$ equations. For understanding where additional equations can be taken from, let us recall that the smoothing spline is calculated via solving the following minimization problem:

$$F=(1-p)\sum_{i=1}^{n}\omega_i\left(y_i-Sp(x_i)\right)^2+p\frac{\int_{x_1}^{x_n}\left(Sp''(z)\right)^2dz}{\left(\int_{x_1}^{x_n}\left(Sp''(z,\vec{C})\right)^2dz\right)_{p=0}}\rightarrow\min \tag{5.22}$$

At each knot x_i, an experimentally measured quantity y_i is known, but in contrast to an interpolating spline, a value of smoothing spline $f_i\equiv Sp(x_i)$ at this knot is unknown and has to be found. Since the vector $f_1,f_2,\ldots,f_n$ must minimize the function F, partial derivatives of (5.22) must be equal to zero i.e. $\frac{\partial F}{\partial f_i}=0$. Condition $\frac{\partial F}{\partial f_i}=0$ provides us additional n equations giving a total $4n$-6 equations. We still need two more equations to be able to determine required $4(n\text{-}1)$ i.e. $4n$-4 coefficients. These two equations are obtained by employing following conditions called "natural boundary conditions"

$$Sp''(x_1)=Sp''(x_n)=0 \tag{5.23}$$

In some cases, the smoothing spline should pass exactly through certain given points even if the function values at these points are determined with a specific error. Therefore, the function where a spline describing a certain set of point should necessarily pass through some of these points and smooth remaining ones is called mixed spline. Available existing algorithms for constructing mixed splines are usually oriented exclusively to accuracy criteria of spline construction, which can not provide identical geometrical description. Moreover, these method are much more complex than traditional methods used to construct approximating splines. Therefore, algorithm for constructing

smoothing splines is changed to construct mixed spline in order to preserve all the advantages of smoothing splines as well as to get an adequate geometric approximation.

Let us first discuss the algorithm of constructing mixed splines because of its versatility and then discuss about the conditions under which mixed spline converges to smoothing spline. This algorithm can be used to construct smoothing splines by relaxing restriction of "hard point". Hard points are those points through which a mixed spline must pass and smooth the other point called "soft points". Therefore, mixed splines can be considered as generalization of smoothing splines. The proposed simple algorithm for constructing mixed splines can easily be used for constructing smoothing splines.

The problem of constructing a mixed spline reduces to the minimization of the functional:

$$F = (1-p)\sum_{i \in S} \omega_i \left[Sp(x_i) - y_i \right]^2 + p \int_{x_1}^{x_n} \left[Sp''(t) \right]^2 dt \to \min \tag{5.24}$$

under the condition that

$$Sp(x_j) = y_j, \forall j \in I \tag{5.25}$$

where I is the set of points through which the spline passes rigorously and S is the set of points smoothed by this spline; $0 \le p < 1$ is the smoothing parameter; i and j are the numbers of experimental points; $\omega_i > 0$ is the statistical weight of the function value at the ith point; x_k, $k = i, j$ are the spline points arranged in an increasing order (the total number of these points is $n \ge 2$); and y_k are the experimental values of the function.

Within the $[x_k, x_{k+1}]$ segment, where $k = 1,...,n-1$, the spline can be represented in the form

$$Sp(x) = C_{k1} + C_{k2}(x - x_k) + \frac{C_{k3}}{2}(x - x_k)^2 + \frac{C_{k4}}{6}(x - x_k)^3 \tag{5.26}$$

In the above expression, coefficient C_{kl} approximates the (l-1)th derivative of the function at point x_k. Below, we confine ourselves to the consideration of splines with the so-called natural boundary conditions $Sp''(x_1) = Sp''(x_n) = 0$. The values of $Sp(x_k)$ are denoted by f_k. Note also that if the set S is empty, the mixed spline is, in fact, a conventional interpolating spline; if the set I contains no elements, we arrive at the classical smoothing spline.

The use of the method of Lagrange factors to solve problem (5.24) under condition (5.25) allows us to reduce the problem to unconditioned minimization of the functional Φ

$$\Phi = (1-p)\sum_{i \in S} \omega_i [f_i - y_i]^2 + p \int_{x_1}^{x_n} [Sp''(t)]^2 dt + \sum_{j \in I} \lambda_j [f_j - y_j]^2 \to \min \tag{5.27}$$

To find the minimum of (5.27), we have to set the corresponding partial derivatives at zero

$$\begin{aligned} \frac{\partial \Phi}{\partial f_i} &= 2(1-p)\omega_i (f_i - y_i) + 2p\left(H^T m\right)_i = 0, \forall i \in S \\ \frac{\partial \Phi}{\partial \lambda_j} &= (f_j - y_j) = 0, \forall j \in I \end{aligned} \tag{5.28}$$

or

$$\begin{aligned} &(1-p)\omega_i f_i + p\left(H^T m\right)_i = (1-p)\omega_i y_i, \forall i \in S \\ &f_j = y_j, \forall j \in I \end{aligned} \tag{5.29}$$

Formula (5.28) includes vector ***m*** consisting of (*n-2*) elements whose components are the second derivatives of the spline at points $x_2,...,x_{n-1}$ and the $\left[(n-2)\times n\right]$ dimensional matrix H with elements $H_{ii} = h_i^{-1}, H_{i,i+1} = -\left(h_i^{-1} + h_{i+1}^{-1}\right)$, and $H_{i,i+2} = h_{i+1}^{-1}$, where $i = 1,...,n-2$; $H_{ij} = 0$ if $j > i+2$. Here, $h_i = x_{i+1} - x_i, i = 1,...,n-1$ and h_i is a vector of the steps of the nodal net comprising $n-1$ elements.

Let us also consider quantity $p^* = 0$ and rewrite (5.29) in the form

$$(1-p^*)\omega_j f_j + p^*\left(H^T m\right)_j = (1-p^*)\omega_j y_j, \forall j \in I \tag{5.30}$$

where ω_j are any nonzero numbers. Note that equations (5.30) are similar to (5.28). We determine a diagonal $\left[n\times n\right]$ matrix P as $P_{ii} = p, \forall i \in S$, and $P_{jj} = p^* = 0, \forall j \in I$. By definition, $U = I_n - P$, where I_n is the unit matrix of order *n*. The system of equations (5.28) and (5.30) can be written in matrix form as

$$U \times W \times f + p \times H^T \times m = U \times W \times y \tag{5.31}$$

where W is the diagonal matrix of rank $\left[n\times n\right]$ with the elements $W_{ii} = \omega_i$ and $W_{jj} = \omega_j$. Multiplying the left-hand side of (5.31) by $H \times W^{-1} \times U^{-1}$ (matrix U at $0 \le p < 1$ is nondegenerate), we obtain

$$H \times f + H \times W^{-1} \times U^{-1} \times p \times H^T \times m = H \times y \tag{5.32}$$

as is known, $H \times f = A \times m$, where A is the $\left[(n-2)\times(n-2)\right]$ tridiagonal symmetric positively defined matrix with elements $A_{ii} = \frac{h_i + h_{i+1}}{3}, i = 1,...,n-2; A_{i,i+1} = A_{i+1,i} = \frac{h_{i+1}}{6}, i = 1,...,n-3$, $A_{ij} = 0$ if $|i-j| \geq 2$. Using this relationship, we can write (5.32) as a system of linear equations in terms of m (recall that $m_1 = m_2 = 0$ by virtue of the above stipulated boundary conditions):

$$\left(A + H \times W^{-1} \times U^{-1} \times P \times H^T\right) \times m = H \times y \tag{5.33}$$

The matrix of system (5.33) is pentadiagonal, symmetric, and positively defined. This allows us to solve the system by the effective monotonic sweep method. The values of the spline at the nodes can easily be determined from the formula

$$f = y - W^{-1} \times U^{-1} \times P \times H^T \times m \tag{5.34}$$

This solves the problem of conditional minimization of (5.24), i.e., the problem of constructing a mixed spline.

Finally, let us examine the effect of variation of smoothing parameter on the geometry of smoothing splines . When smoothing parameter p is large ($p \rightarrow 1$), this places a premium on smoothness. Conversely, a small value of p (near zero) corresponds to more emphasis on goodness-of-fit. A smoothing spline at the smoothing parameter p=0 is a conventional interpolating spline precisely describing the data in question with the possibility of having some spurious singularities resulting in a large number of extrema and inflection points (Figure 5.5 and Figure 5.6).

is quite clear from the discussion done so far in this section that the isogeometric approximation by using smoothing splines can be used for robust numerical differentiation.

This idea of isogeometric approximation by using smoothing splines for robust numerical differentiation of experimental data has been implemented in a program and a software has been developed for treating raw $R(T)$ profiles to deduce the required information from them. For developing this program, codes were written in FORTRAN. Dr. Dmitri V. Malakhov, Department of Materials Science and Engineering, McMaster University, has been instrumental in the development of this software. This software has been used in this work for revealing elusive features of $R(T)$ measurements.

We know that choosing an appropriate smoothing parameter, p, is the key factor, which actually controls the accuracy of isogeometric approximation procedure. Therefore, it is very important to develop such a method of finding appropriate smoothing parameter, which is accurate, simple and unambiguous.

It has been mentioned earlier in this section that numbers of extrema and inflection points are relatively easy to deduce from experimental observations if the observations are not too noisy. In our case, $R(T)$ data are not too noisy and it is quite possible to find number of extrema and inflection points directly from the experimental observations. Now, this information can be used to find an appropriate smoothing parameter resulting correct isogeometric approximation. This idea has been incorporated in the software for finding an appropriate smoothing parameter. Let us have a look on the

procedure used in the program for finding a suitable smoothing parameter This procedure has been illustrated in the Figure 5.7

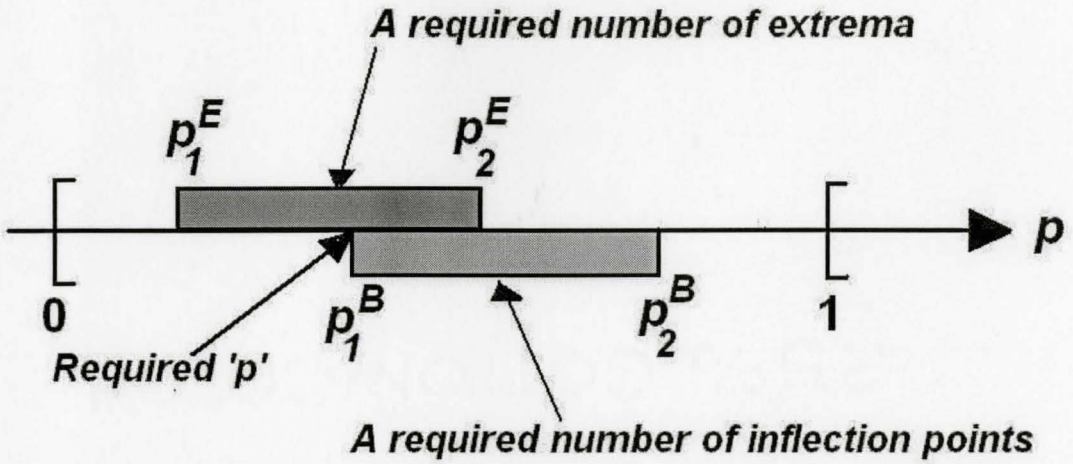

Figure 5.7: Illustration of procedure for finding suitable smoothing parameter

In Figure 5.7, p_1^E and p_2^E can be defined in the following way·

$$p_1^E \quad \forall p < p_1^E, e(p) > E$$
$$p_2^E \quad \forall p > p_1^E, e(p) \le E-1$$

where, E is the required number of extrema, B is the required number of inflection points, $e(p)$ is the number of extrema for the given p, and $b(p)$ is the number of inflection points for the given p. p_1^B and p_2^B can be defined in the similar way From the Figure 5.7, it can be deduced that the condition $\forall p \in \left[\max\left(p_1^E, p_1^B\right), \min\left(p_2^E, p_2^B\right)\right]$ will result in a spline with required number of E and B. Here, it must be understood that we have to take the minimal p because in this case the accuracy of description is the best. It must also be clear that both the regions of E and B must have a common point for the feasibility of isogeometric approximation otherwise isogeometric spline smoothing will not be possible.

Chapter 6: R-data and their interpretation

If a deformed polycrystalline alloy system containing second phase particles is annealed at a constant heating rate, interpretation of resistivity data ($R(T)$-data) from *in-situ* measurements can be done in the following way. In such a system, various contributions to electrical resistivity at temperature T can be expressed by the following equation:

$$\rho(T) = \rho_o(T) + \rho_d(T) + \rho_{solute}(T) + \rho_{ppt}(T) \tag{6.1}$$

where, $\rho(T)$ is the measured resistivity, $\rho_o(T)$ is contribution from base matrix, $\rho_d(T)$ is contribution from defects (primarily from dislocations), $\rho_{solute}(T)$ contribution due to solutes in the solid solution and $\rho_{ppt}(T)$ is the contribution due to second phase precipitates in the system.

If there is a dissolution or precipitation of second phase particles in the course of experiments, resistivity contribution of solutes and precipitates to the total measured resistivity will keep on changing due to variation in their amount in the alloy system. If the resistivity contribution due to solutes and second phase particles can be made constant somehow, the variation in the measured resistivity can be considered due to temperature variation (phonons) and annihilation of defects (e.g. dislocations) only. As shown in Figure 6.1, electrical resistivity is increasing with increase in temperature for pure annealed Al and Al-1%Mg alloy. Therefore, during annealing of deformed polycrystalline samples, resistivity will increase with temperature while annihilation of

dislocations will try to decrease the resistivity. These two contributions will act as balancing forces and the shape of the measured resistivity vs. T curve will be guided by the effects of these balancing forced.

As discussed in chapter 4, contribution due to phonons is very large large as compared to defects (i.e. dislocations) at high temperatures. Because of the domination of phonon contribution ($\rho_o(T)$) at high temperatures, effect of annihilation of dislocations on measured resistivity becomes elusive and can not be observed on the $\rho(T) vs. T$ profile. To prove this point, let us have a look at the $\rho(T) vs. T$ profile from *in-situ* measurements of electrical resistivities at constant heating rate as shown in Figure 6.2. In this case, it can be observed that $\rho(T) vs. T$ profile is *almost* straight line and there is no visible direct evidence of deviation of curve to estimate the onset and completion of recrystallization.

In Figure 6.2, resistivity values are shown in *red* whereas *corridor of error* is shown in *blue* color. In order to calculate the corridor of error, two types of error have been taken into account. First, error involved in resistance measurements and second, error involved in measurement of dimensions of the sample used for converting resistance to resistivity. The procedure involved in the calculation of corridor of error can be explained in the following way.

$$\rho = R \times \left(\frac{w \times t}{l} \right) = f(R, w, t, l)$$

where, ρ =Electrical resistivity, R = Resistance, w = width of the sample, t =thickness of the sample, and l = length of the sample.

Therefore, total error can be calculated by using the following expression:

$$\Delta\rho = \sqrt{\left\{\left(\frac{\partial f}{\partial R}\Delta R\right)^2 + \left(\frac{\partial f}{\partial w}\Delta w\right)^2 + \left(\frac{\partial f}{\partial t}\Delta t\right)^2 + \left(\frac{\partial f}{\partial l}\Delta l\right)^2\right\}}$$

$$= \sqrt{\left\{\left(\frac{w\times t}{l}\Delta R\right)^2 + \left(\frac{R\times t}{l}\Delta w\right)^2 + \left(\frac{R\times w}{l}\Delta t\right)^2 + \left(\frac{R\times w\times t}{l^2}\Delta l\right)^2\right\}}$$

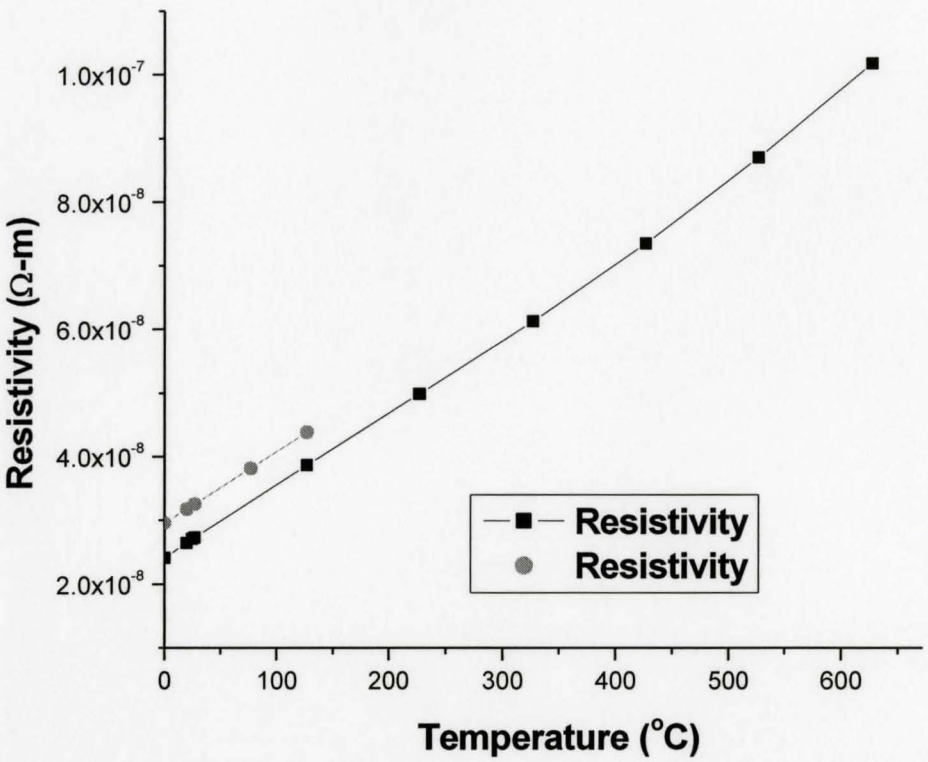

Figure 6.1: Resistivity variation w.r.t. temperature for pure Al and Al-1%Mg (Data from CRC handbook of physics and chemistry 2005)

In order to overcome this problem, a different approach has been applied to analyze these profiles for estimating the temperature range of the onset and the completion of recrystallization. As shown in Figure 6.1, slope of the $\rho(T).vs.T$ profile is expected to remain constant or increase with increase in temperature. On the other hand, slope must decrease with increase in temperature due to disappearance of dislocations during recrystallization. If these two ideas are put together, it can be expected that occurrence of events can be identified by the change in slope of the $\rho(T)vs.T$ profile i.e. a decrease in the slope of $\rho(T)vs.T$ profile in the range of temperatures where recrystallization are expected to occur. Thus, it would necessitate to analyze a $\frac{d(\rho)}{dT}vs.T$ profile rather than $\rho(T)vs.T$ profile to reveal the occurrence of required events from *R*(*T*) measurements.

Since raw data obtained from *in-situ* *R*(*T*) measurements are mixed with Gaussian noise, $\rho(T)vs.T$ profile can not be differentiated directly to get $\frac{d(\rho)}{dT}vs.T$ profile (Figure 6.3). Therefore, a very efficient and accurate method of smoothing and robust numerical differentiation is required to treat these data.

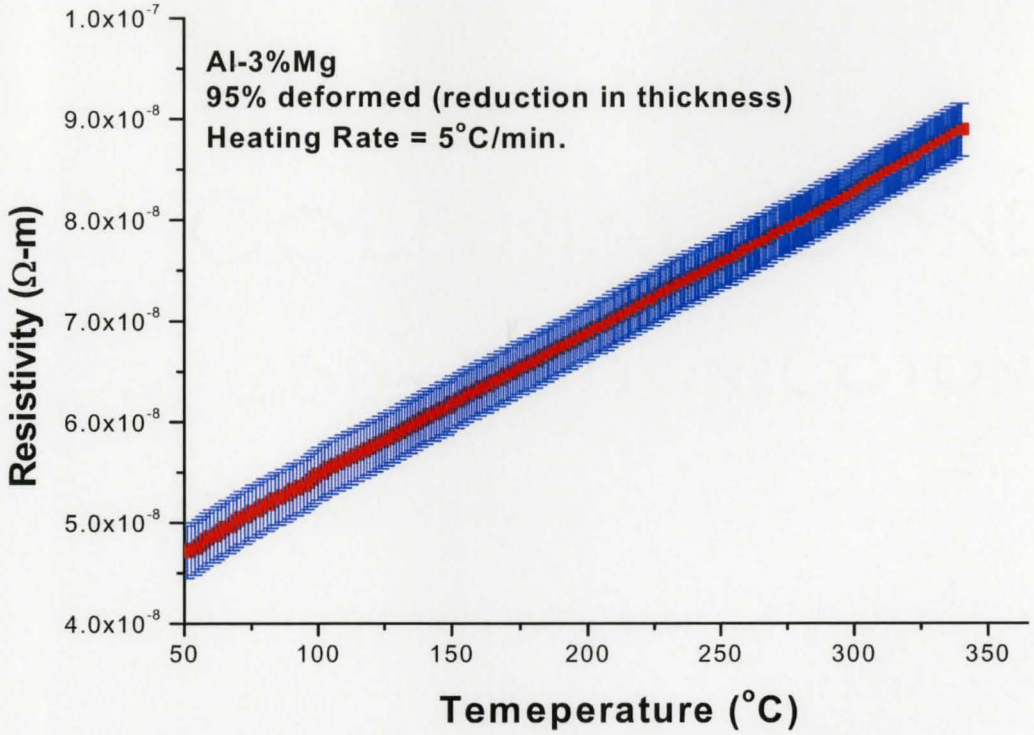

Figure 6.2: Resistivity vs. T profile for 95% deformed Al-3%Mg

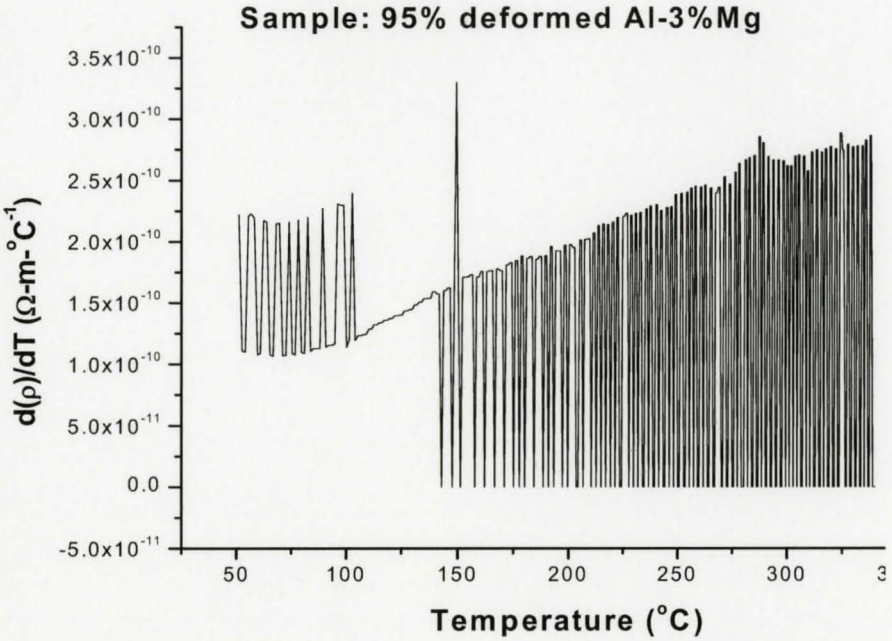

Figure 6.3: Differentiation of R(T) vs. T profile without smoothing data

In this work, a spline based method of smoothing and robust numerical differentiation has been employed to treat these data successfully In order to analyze the data from $R(T)$ measurements using spline based method, following strategy has been adopted. First, the measured data points from $R(T)$ measurements were used to build a replica of the $R(T)$ profile using smoothing splines (Figure 6.4). Later on, this smooth replica of $R(T)$ measurements was used for robust numerical differentiation to build the $\frac{d(\rho)}{dT} vs. T$ profile for the given $R(T)$ measurements (Figure 6.5).

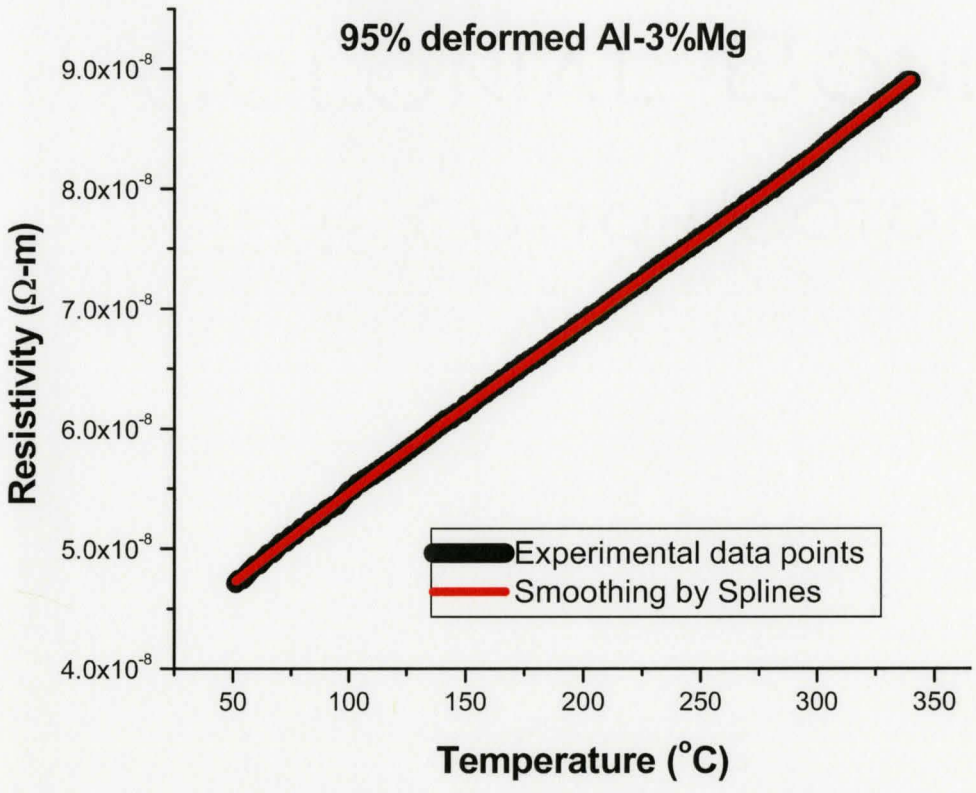

Figure 6.4: Smoothing of experimental data points by Splines

Let us analyze $\frac{d(\rho)}{dT} vs. T$ profile, as shown in Figure 6.5, to identify the positions where one can expect events (recrystallization) to occur. While characterizing recrystallization, we have to bear in mind that rate of disappearance of dislocations is maximum during the course of the structure change. Therefore, we should look for the region in the $\frac{d(\rho)}{dT} vs. T$ profile where maximum decrease in slope is observed as resistivity is directly related with the dislocation density in the material. The starting point of beginning of this change can be identified as temperature of onset of recrystallization whereas the point where minimum value is attained can be identified as the maximum rate of transformation.

The whole region of temperature can be characterized as the region where recrystallization is expected to occur and extent (onset to finish) of reaction can be estimated accordingly. After reaching the minimum, slope again starts to increase. This increase in slope can be attributed to the grain growth region. However, depending upon the kinetics' of the reaction, the downward peak may not be as sharp as shown in Figure 6.5. In such cases, interpretation of $R(T)$ data should be based on the physical nature of the material, keeping in mind the expected kinetic behavior of the particular material under investigation.

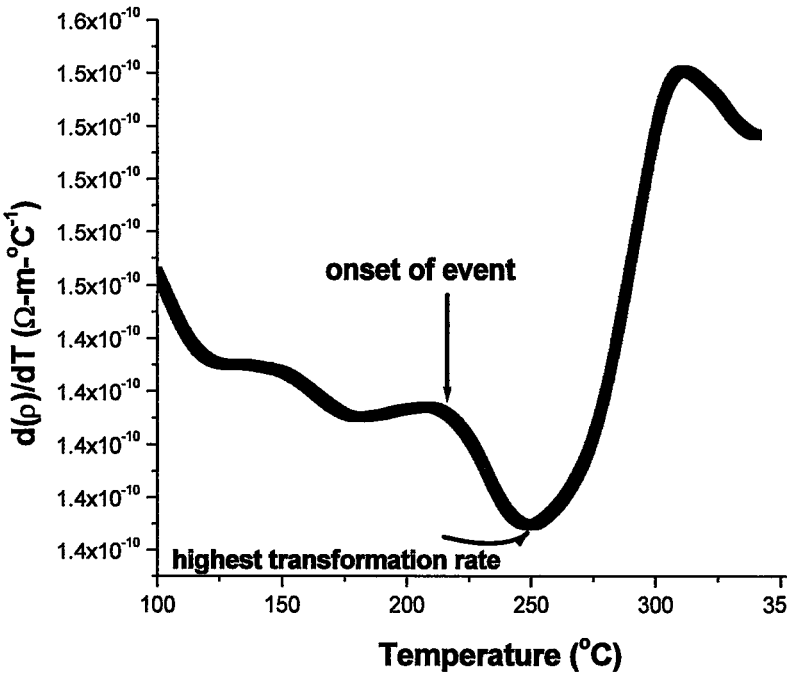

Figure 6.5: Robust numerical differentiation of smoothed R(T) data

Although arguments made regarding the interpretation of *in-situ* resistivity data seem logical in view of the evidence provided, however, it is necessary to confirm that these are not the artifacts of the experiments or data processing procedure. If the methodology explained in the preceding paragraphs is valid then the slope of $\rho(T) vs. T$ profile of a pure and annealed metal (e.g. Al) should either remain constant or increase. In other words, $\frac{d(\rho)}{dT} vs. T$ profile of the pure and fully annealed Al must remain constant or increase with increasing temperature. To substantiate this argument, *in-situ* electrical resistivity measurement experiments were carried out for pure Al (99.9995% purity) and data were collected while heating the Al sample at a constant heating rate of 5°C/minute. A change of slope of resistivity profile as a function of temperature i.e. $\frac{d(\rho)}{dT} vs. T$ profile

of pure Al is shown in Figure 6.6. It can be seen that slope is constant until approximately 125°C after that there is a gradual increase in slope with increasing temperature. There is no trace of existence of any inverted peak. Therefore, it can be accepted as a confirmation of the hypothesis that the presence of an inverted peak is related with some "event" or transformation going on in the material. The nature of the transformation or "event" can also be inferred from the presence of an inverted peak. Presence of an inverted peak indicates that the transformation is actually decreasing the resistivity of the material as opposed to increasing temperature. Therefore, if a comparison of Figure 6.5 and Figure 6.6 is made, it can be confidently stated that the presence of inverted peak in deformed alloy can be either related to disappearance of dislocations (i.e. recrystallization) and/or precipitation of second phase particles.

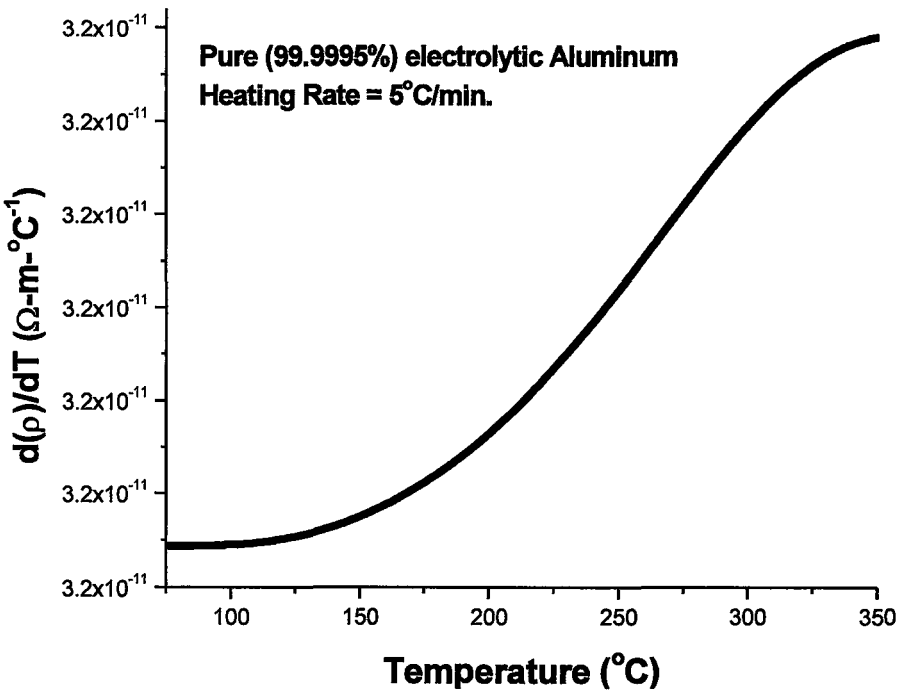

Figure 6.6: Showing continuous increasing slope of resistivity as a function of temperature

Chapter 7: Results and discussion

7.1: Analysis of resistivity measurements for 95% deformed Al-3%Mg alloy

This section is devoted to the analysis of results obtained by *in-situ* electrical resistivity measurements for 95% deformed Al-3%Mg alloy samples. As it is clear from the previous discussion that our intention is to characterize recrystallization and identify the temperature range of occurrence of this event from $R(T)$ measurements. The observations made by resistivity measurements were verified by optical metallography as well as micro-hardness measurements to establish that new approach of characterizing recrystallization is reliable. Apart from that, it is also intended to comment on the kinetics of recrystallization qualitatively.

Let us first analyze the data obtained for 95% deformed samples heated upto 400°C at a constant heating rate of 5°C/min. The $\frac{d(\rho)}{dT} vs. T$ profile obtained is shown in Figure 7.1. As discussed in the previous chapter, the point where we observe a sudden drop in the profile can be identified as beginning of event or recrystallization to be precise. For sample-1, such a point is observed at around 220°C and the curve touches the minimum point at around 260°C. Therefore, the range of occurrence of recrystallization can be estimated between 220°C and 260°C. However, there is a slight difference between the finishing point of 1st and 2nd second samples. This difference can be attributed to the possibility of slight difference in the physical state of the material and

experimental errors involved during measurements. Despite these slight differences, resistivity measurements have very good reproducibility of results.

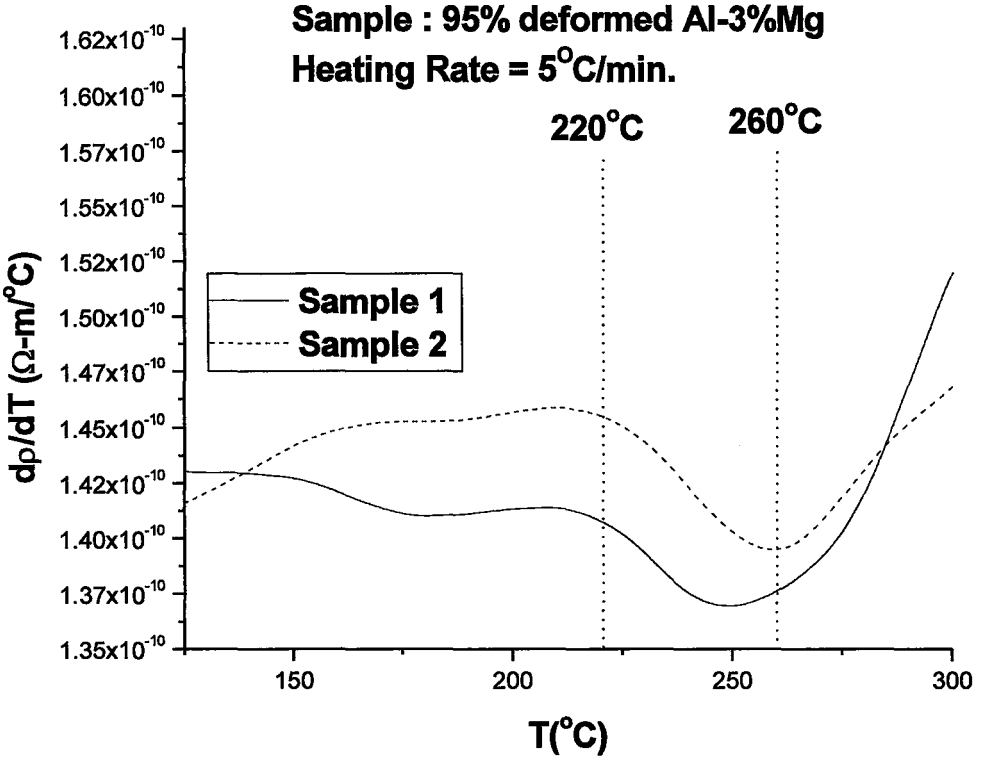

Figure 7.1: Change of slope of resistivity curves as a function of temperatures for 95% deformed Al-3%Mg alloy

In order to verify our hypothesis regarding these profiles, optical metallographic studies were conducted at various points corresponding to profile shown in Figure 7.1. In this particular case, samples were heated from room temperature upto 220°C, 240°C, 260°C, and 300°C at the heating rate of 5oC/min and quenched in ice water. Samples were electro-etched using Barker's solution whereas Nomarski surface profiling technique was used to look at the microstructures. The microstructures corresponding to

deformed state and these points are shown in Figure 7.2 to Figure 7.6. All the microstructures belong to the *L-T* (longitudinally-transverse section) of the material.

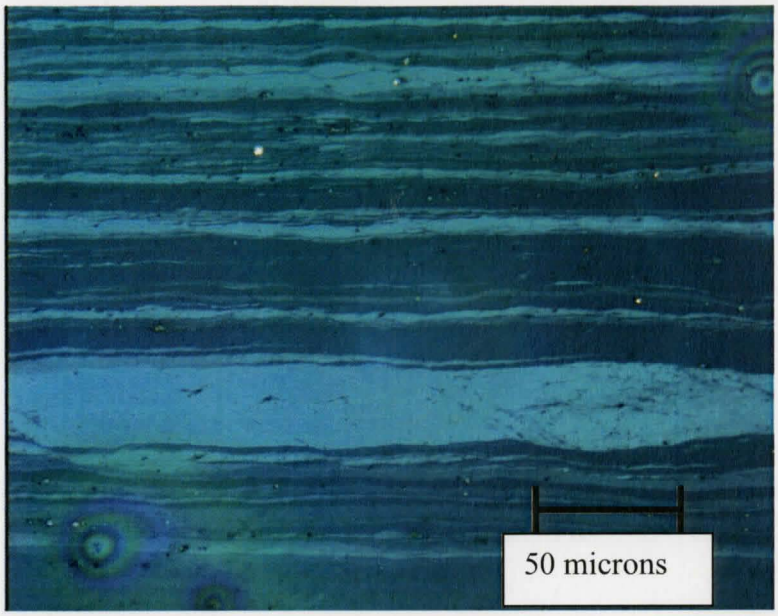

Figure 7.2: Microstructure of 95% deformed Al-3%Mg alloy on L-T section, showing layered structure and deformation bands

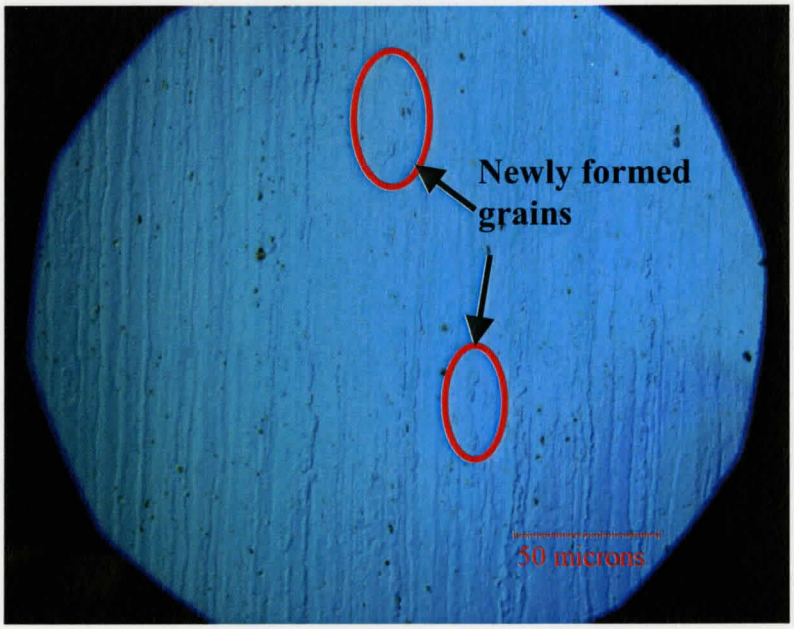

Figure 7.3:Microstructure of 95% deformed Al-3%Mg alloy, quenched from 220 deg. C, early stages of recrystallization

Figure 7.4:Microstructure of 95% deformed Al-3%Mg alloy, quenched from 240 deg.C, partial recrystallization

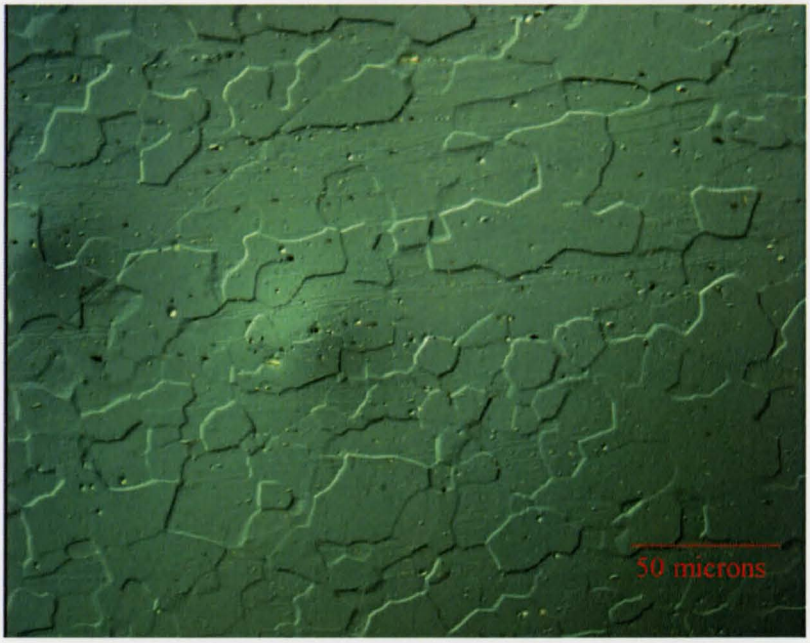

Figure 7.5:Microstructure of 95% deformed Al-3%Mg alloy, quenched from 260 deg. C, complete recrystallization

Figure 7.6:Microstructure of 95% deformed Al-3%Mg alloy, quenched from 300 deg. C, s grain growth.

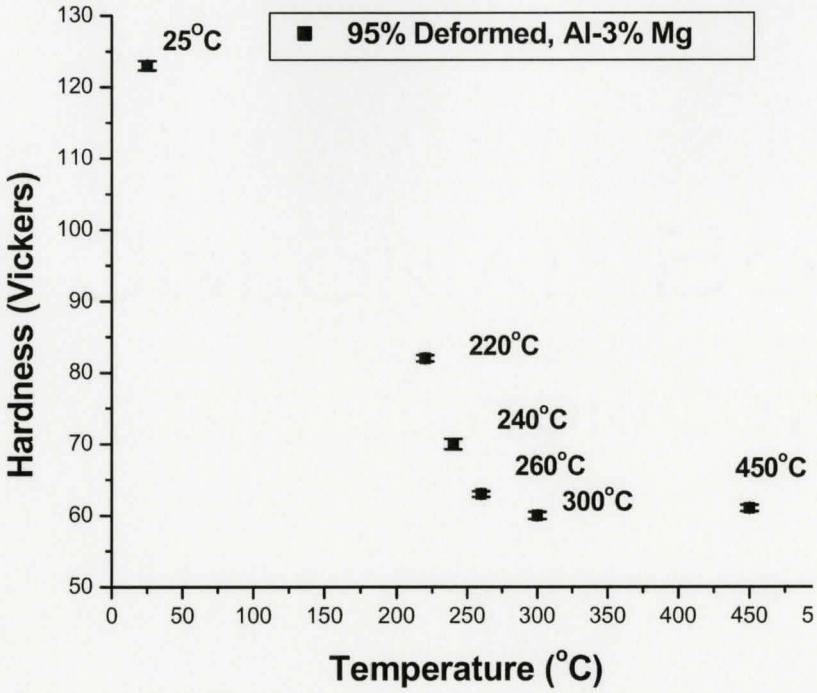

Figure 7.7: Micro-hardness as a function of temperature for 95% deformed Al-3%Mg alloy, mean of 50 measurements for each sample

The series of the micrographs shown above support the observations made by resistivity measurements. Micro-hardness measurements were done on the samples corresponding to 220°C, 240°C, 260°C, 300°C and 450°C. Hardness of deformed sample and fully annealed sample (solutionized at 450°C for 7 hours) has been taken as reference data. The hardness measurements, as shown in Figure 7.7, also confirm the behavior observed by resistivity measurements indicating a sharp decrease in hardness starting at 220°C whereas slight decrease after 260°C. Since a few newly formed grains are visible at 220°C, it can be confidently concluded that temperature of onset of recrystallization exists at some lower temperature than 220°C ($T_{beg}^{95}(I2) \leq 220^{o}C$) whereas completion of recrystallization was established at 260°C i.e. $T_{end}^{95}(I2) \geq 260^{o}C$.

7.2: Analysis of resistivity measurements for 75% deformed Al-3%Mg alloy

The resistivity data for 75% deformed and annealed samples are shown in Figure 7.8.

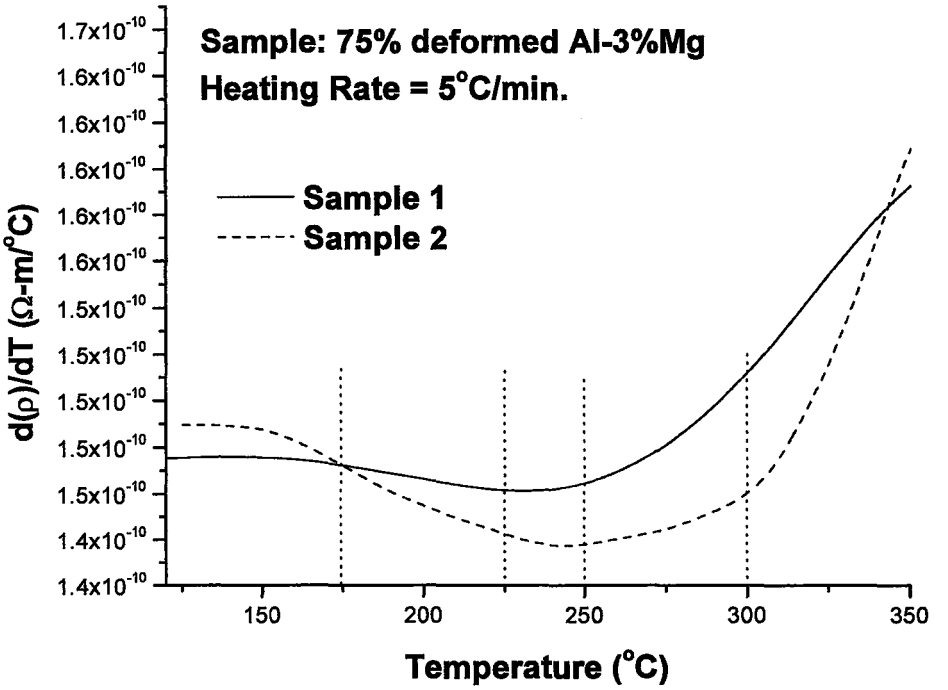

Figure 7.8: Change of slope of resistivity curve as a function of temperature for 75% deformed Al-3%Mg.

From Figure 7.8, range of recrystallization can be estimated between 175°C and 250°C. However, it is clear from the profile that decrease in slope is not very sharp and the peaks are relatively less pronounced as compared to 95% deformed samples. Let us analyze a series of micrographs corresponding to 75% deformed sample as well as samples annealed upto 175°C, 250°C and 300°C temperatures as shown in Figure 7.9 to Figure 7.13.

No visible differences between the microstructures of deformed and 175°C annealed samples can be observed. However, a very small degree of recrystallization is observed in the microstructure belonging to sample annealed upto 225°C. Further annealing upto 250°C shows a partial recrystallization, whereas almost complete recrystallized state is attained in the sample annealed upto 300°C. The variation of hardness with increase in temperature, as shown in Figure 7.14, is quite similar to resistivity analysis. However, sharp decrease in hardness was observed at 225°C, which is in the accordance of metallographic and resistivity observations. There is a decrease in resistivity profile at 175°C but no evidence of recrystallization was found at 175°C by the metallographic observations.

Hardness measurements also show a gradual decrease between 175°C and 225°C but it becomes very sharp only after 225°C. This sharp decrease indicates a very fast transformation of the deformed structure, which can be related with recrystallization. Based on the analysis of the results of electrical resistivity, optical metallography and hardness measurements, range of recrystallization can be estimated between 225°C and 300°C. In addition, it can be confidently established that onset of recrystallization is occurring at a temperature below 225°C i.e. $T_{beg}^{75}(I2) \leq 225^{o}C$ whereas completion occurs at around 300°C i.e. $T_{end}^{75}(I2) \geq 300^{o}C$

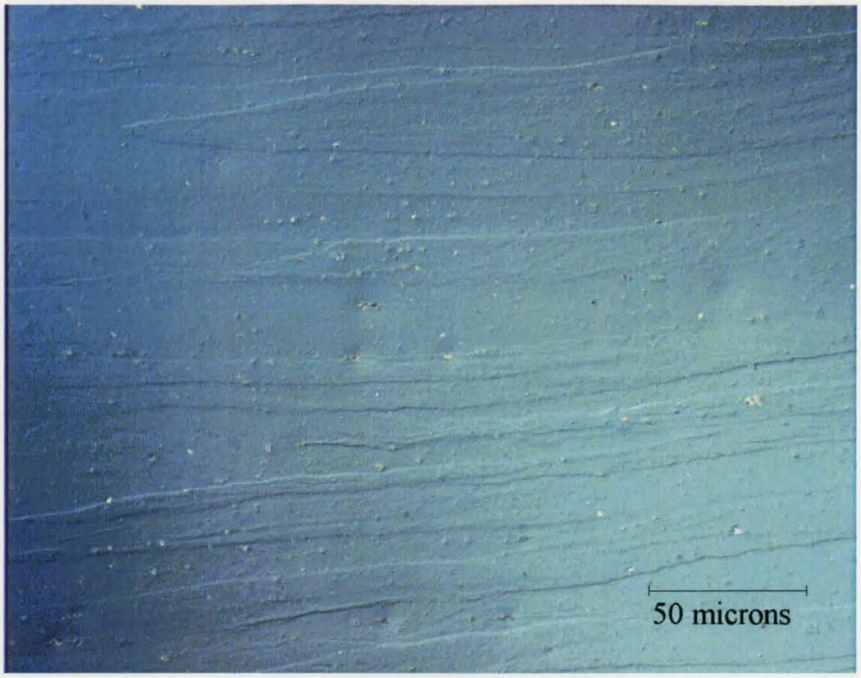

Figure 7.9:Microstructure of 75% deformed Al-3%Mg

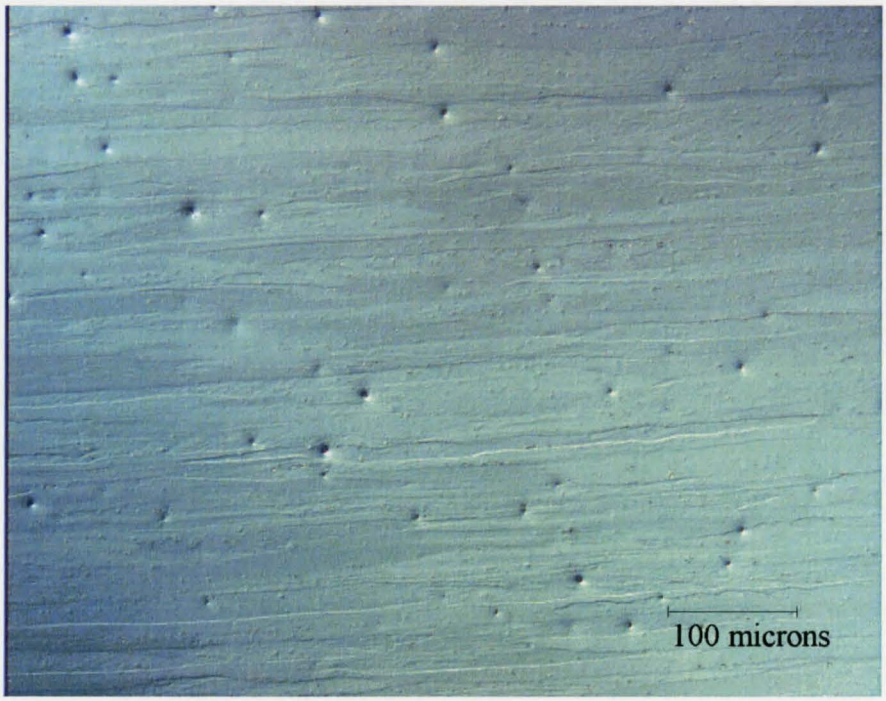

Figure 7.10:Microstructure of 75% deformed Al-3%Mg, annealed and quenched from 175 deg.C

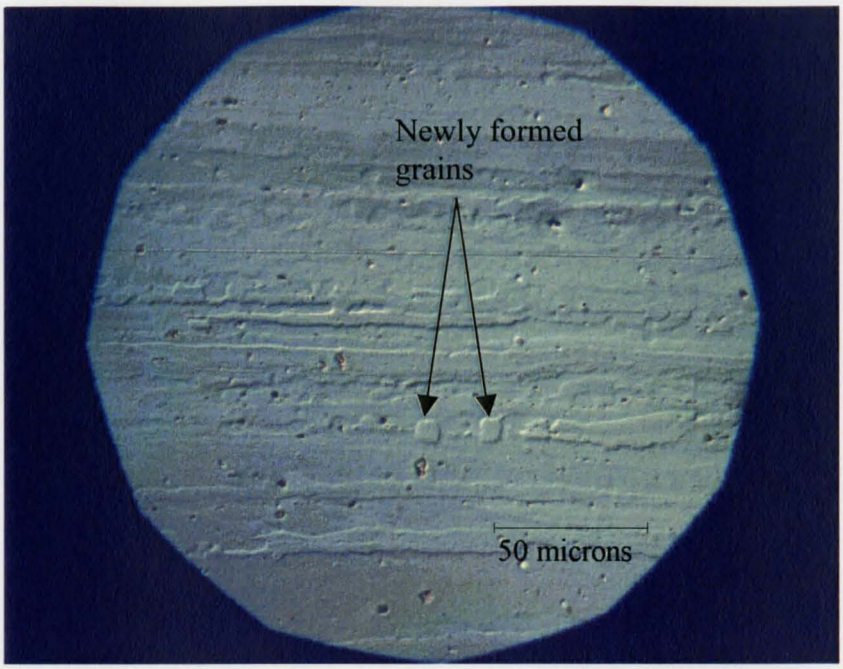

Figure 7.11:Microstructure of 75% deformed Al-3%Mg, annealed and quenched from 225 deg.C

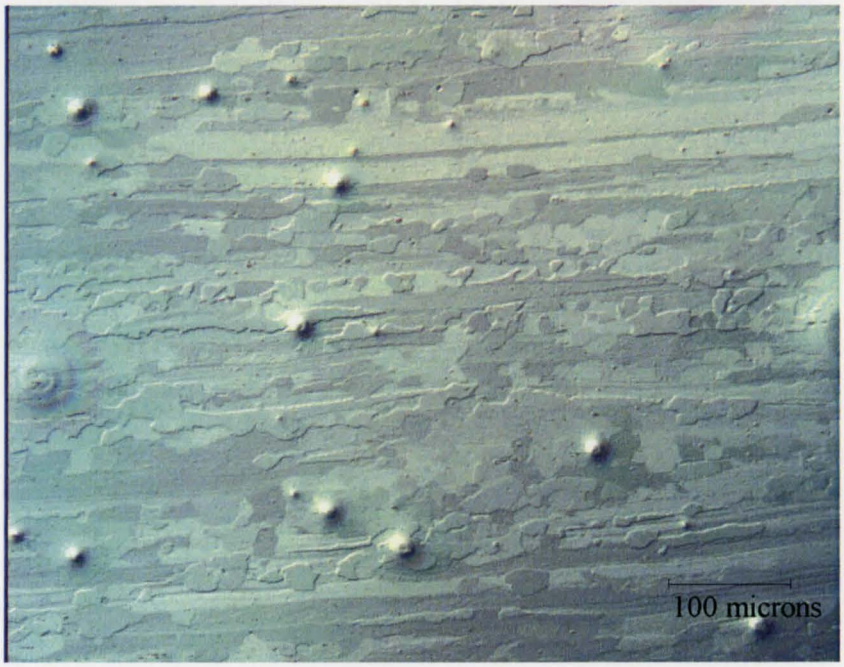

Figure 7.12:Microstructure of 75% deformed Al-3%Mg, annealed and quenched from 250 deg.C

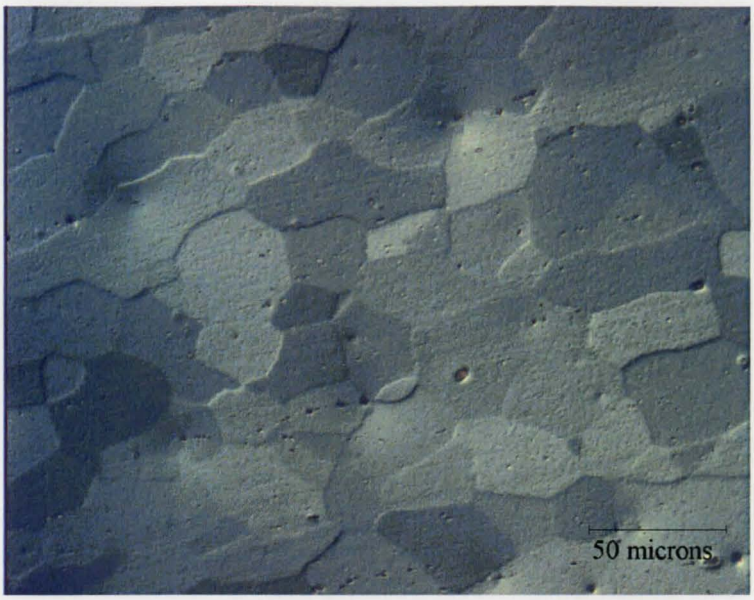

Figure 7.13:Microstructure of 75% deformed Al-3%Mg, annealed and quenched from 300 deg.C

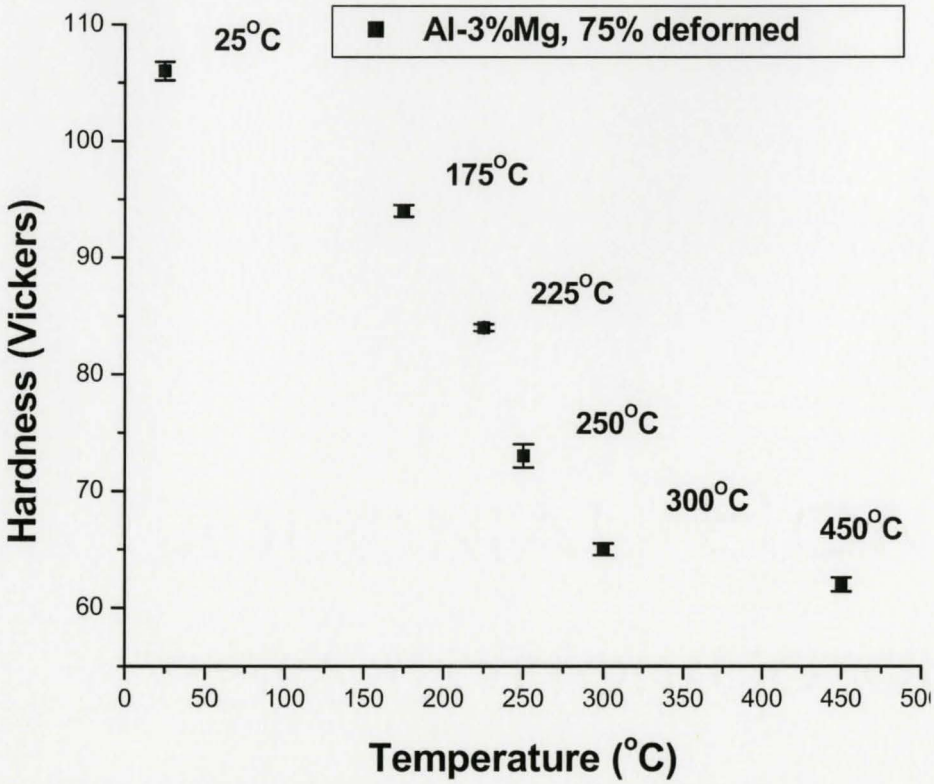

Figure 7.14: Micro-hardness measurements as a function of temperature for 75% deformed Al-3%Mg, mean of 50 measurements for each sample

7.3: Analysis of resistivity measurements for 95% deformed Al-Mg-Fe-Mn (I5) alloy

The *in-situ* resistivity measurements for 95% deformed and annealed samples are shown in Figure 7.15.

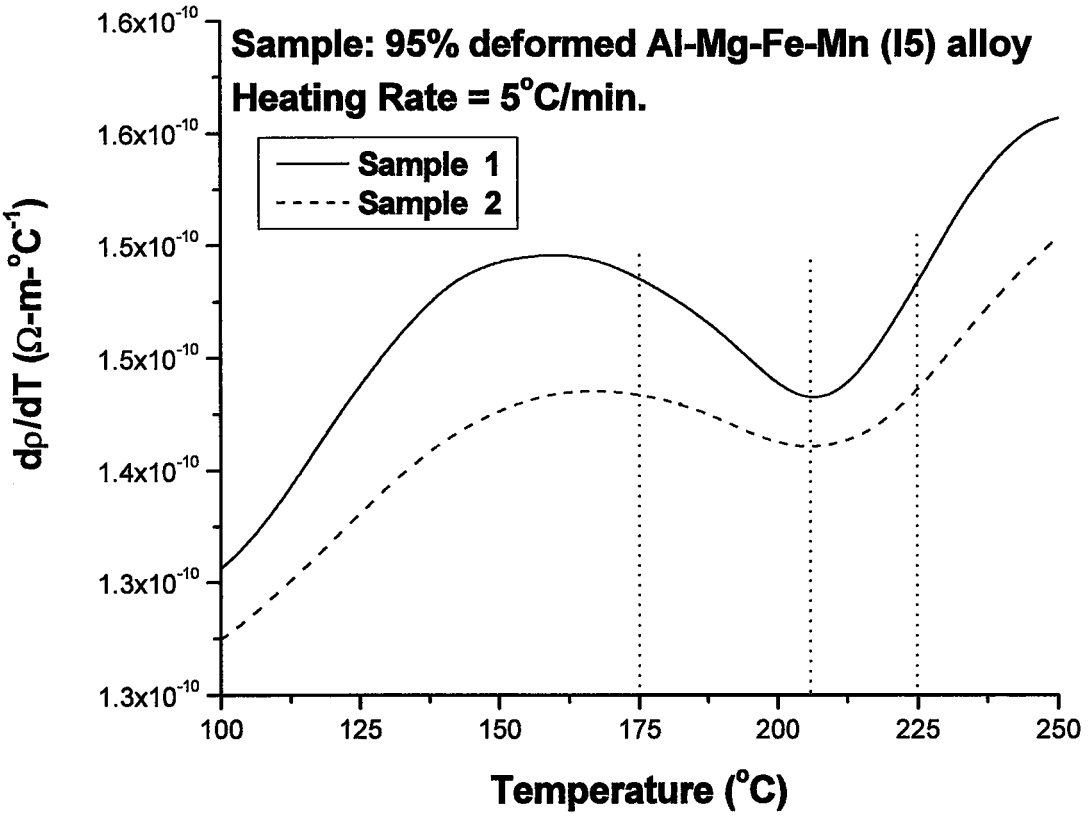

Figure 7.15: Change of slope of resistivity curve as a function of temperature for 95% deformed Al-Mg-Fe-Mn (I5) alloy

From Figure 7.15, estimation for range of temperature of recrystallization suggests the recrystallization must occur between 175°C and 225°C approximately. The resistivity measurements for two different samples again indicate reproducibility of results. In this case, peaks are sharp which means reaction is occurring very fast. In order to verify our predictions regarding the events, optical metallography and micro-hardness

studies were carried out. For optical metallographic observations, samples were heated from room temperature upto 175°C, 206°C and 225°C at the heating rate of 5°C/min and then ice water quenched subsequently Metallographic observation included the deformed sample also. For hardness measurements, samples with the heat-treat conditions similar to metallography were used. In addition, deformed sample and fully annealed sample (solutionized at 450°C for 7 hours) were used as reference.

Let us analyze the optical micrographs, shown in Figure 7 16 to Figure 7 19, corresponding to the positions mentioned in the previous paragraph as well as results of micro-hardness measurements shown in Figure 7.20.

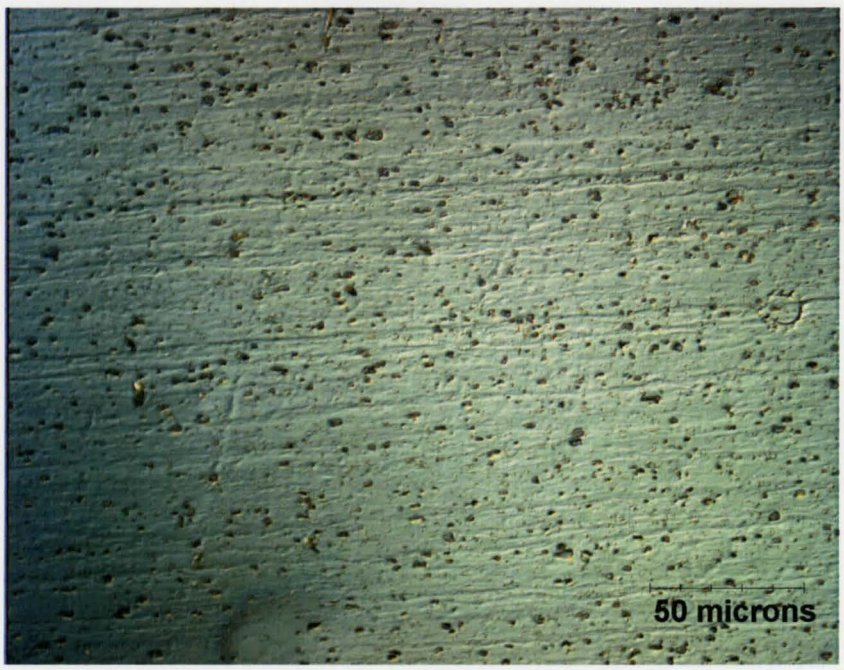

Figure 7.16:Microstructure of 95% deformed Al-Mg-Fe-Mn (I5) alloy

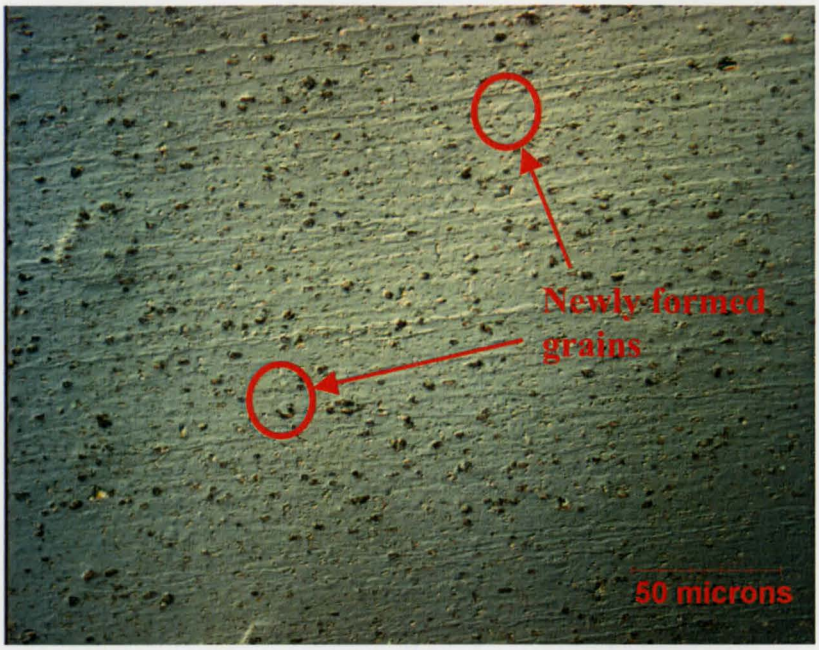

Figure 7.17:Microstructure of 95% deformed Al-Mg-Fe-Mn (I5) alloy, annealed and quenched from 175 deg.C

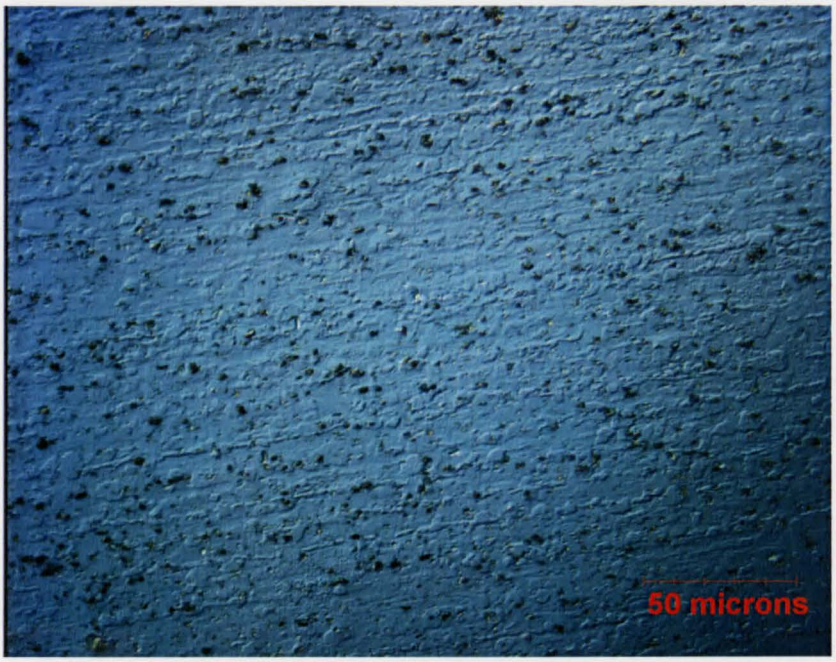

Figure 7.18:Microstructure of 95% deformed Al-Mg-Fe-Mn (I5) alloy, annealed and quenched from 206 deg.C, partial recrystallization

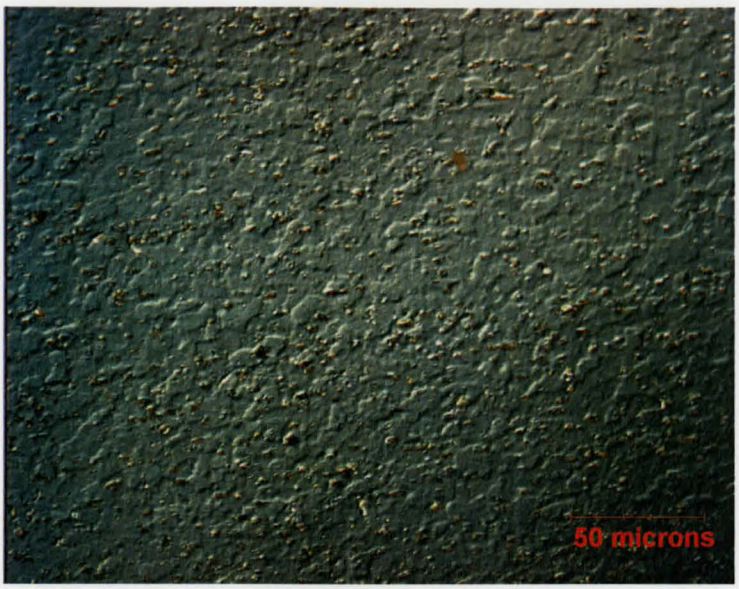

Figure 7.19:Microstructure of 95% deformed Al-Mg-Fe-Mn (I5) alloy, annealed and quenched from 225 deg.C

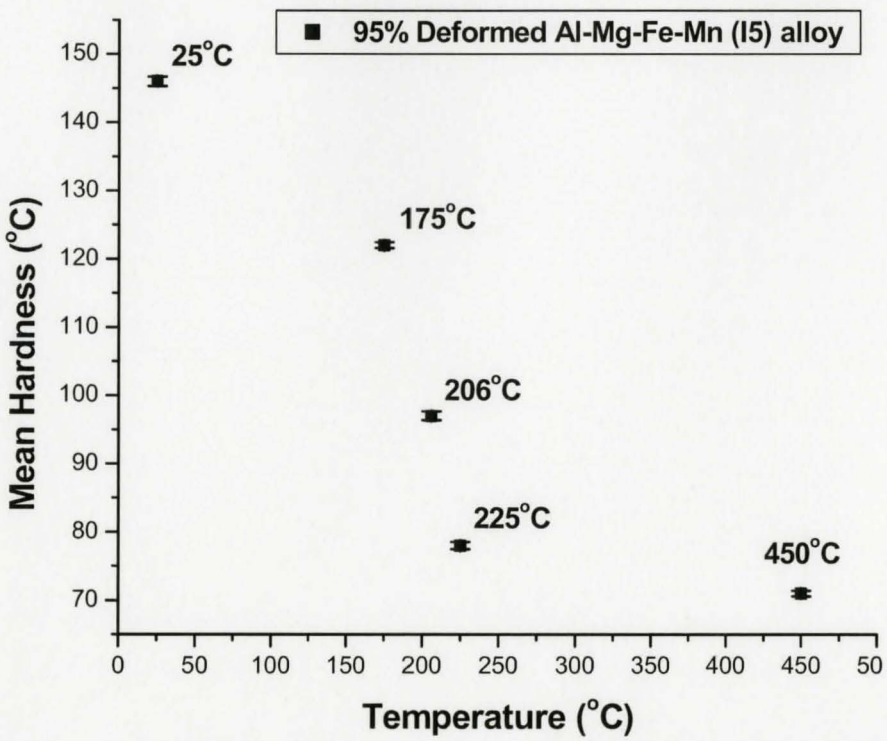

Figure 7.20: Micro-hardness measurements as a function of temperature for Al-Mg-Fe-Mn (I5) alloy, mean of 50 measurements for each sample

The common feature of these micrographs is the presence of large number of second phase particles because of high Fe and Mn content in the alloy. Large particles out of these particles are expected to provide additional nucleation sites for recrystallization whereas fine particles are believed to restrict grain growth after nucleation. However, such kind of high amount of alloying additions makes the system complex resulting in extremely difficult situation for characterizing and predicting the trend of recrystallization accurately.

The optical micrographs do not show appreciable difference in the microstructure of deformed and 175°C annealed samples except appearance of a few very fine newly formed grains. But, such prediction about the point of onset of recrystallization are not confidently substantiated by microstructural observations as these newly formed fine grains are not fully resolved due to presence of large number of second phase particles. However, analysis of micro-hardness measurements (Figure 7.20) reveals that hardness start decreasing at 175°C, which is in agreement with the resistivity measurements. However, a sharp decrease is observed at 206°C where a significant amount of recrystallization is observed by metallographic investigation. Therefore, it can be safely concluded from the microstructural observations that the onset of recrystallization exits below 206°C i.e. $T_{beg}^{95}(I5) \leq 206$.

According to the estimations from resistivity measurements, 206°C is the point of almost complete recrystallization. However, microstructural observations at this point show a partial recrystallization. In contrast, almost fully recrystallization is observed at 225°C. These observations are supported by hardness measurements also. Therefore,

analysis of resistivity measurements must be carried out keeping in mind the physical nature and complexity of alloys. As far as almost fully recrystallized state is concerned, hardness measurements on fully recrystallized (solutionized at 450°C for 7 hours) and 225°C annealed samples indicate that there is no significant difference in the mean hardness values for the two above measurements. This information reveals the fact that 225°C annealed samples are almost completely recrystallized i.e. $T_{end}^{95}(I5) \approx 225$. In conclusion, it can be confidently stated that recrystallization temperature range lies between 175°C and 225°C.

7.4: Analysis of resistivity measurements for 75% deformed Al-Mg-Fe-Mn (I5) alloy

The resistivity measurements for 75% deformed Al-Mg-Fe-Mn alloy is shown in Figure 7.21. An analysis of this profile shows that the temperature of onset of recrystallization can be expected at 175°C. Based on the resistivity measurements profile, while considering the analysis and results of 95% deformed Al-Mg-Fe-Mn alloy, a significant recrystallization can be expected at 212°C whereas almost complete recrystallization can be expected at around 225°C.

In order to verify that the region between 175°C and 225°C can be associated with recrystallization, a series of optical metallographic observations were carried out pertaining to the deformed state and desired annealed states. For this purpose, samples were heated upto 175°C, 212°C and 225°C and then ice water quenched. Micro-hardness measurements were also done on these samples. In addition, micro-hardness measurements were carried out on fully annealed (solutionized at 450°C for 7 hours) in

order to ascertain that the estimation of almost complete recrystallization is correct. If the estimation is correct, hardness value at 225°C should be comparable to the hardness value of fully annealed sample. Optical micrographs corresponding to the points of interest (i.e. deformed state, 175°C, 212°C, and 225°C) are shown in Figure 7.22 to Figure 7.25, whereas hardness measurement data are shown in Figure 7.26.

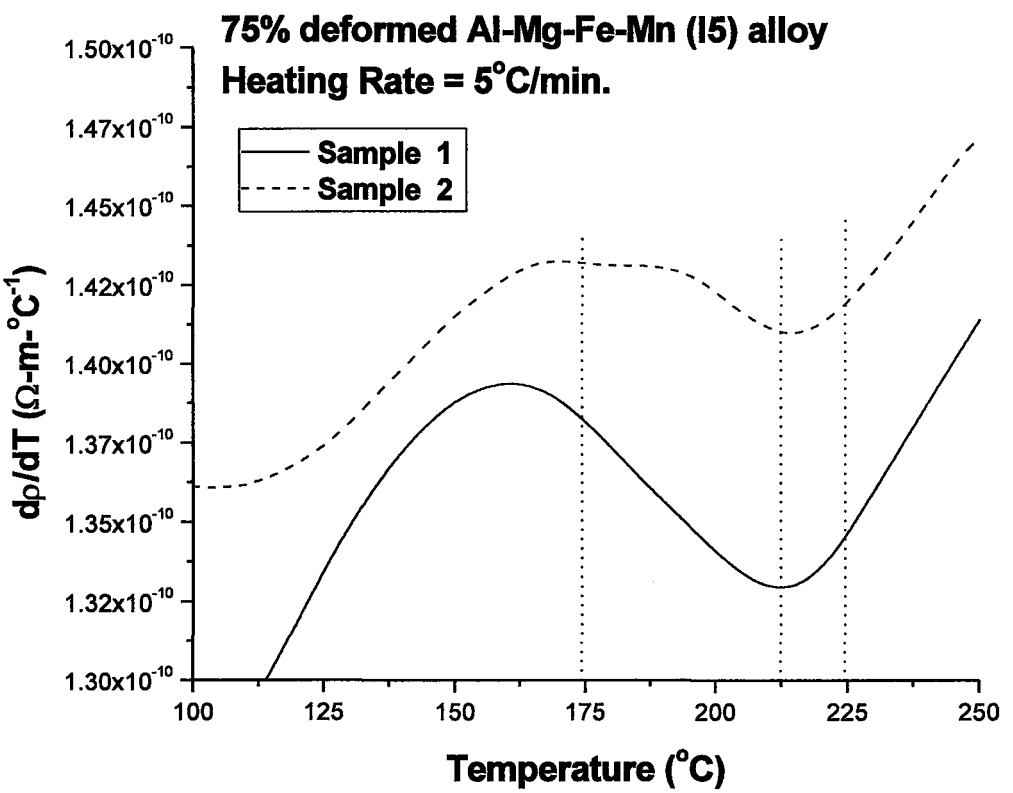

Figure 7.21: Change of slope of resistivity curves as a function of temperature for 75% deformed Al-Mg-Fe-Mn (I5) alloy

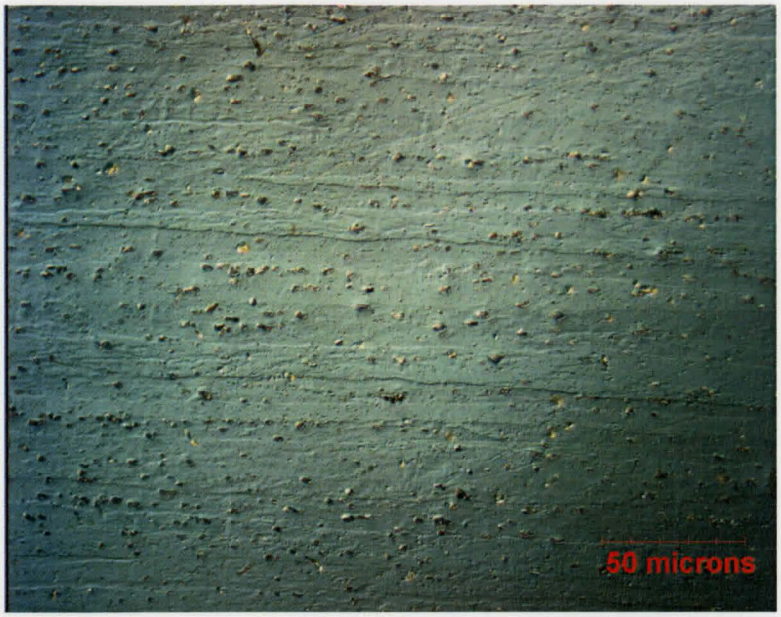

Figure 7.22:Microstructure of 75% deformed Al-Mg-Fe-Mn (I5) alloy

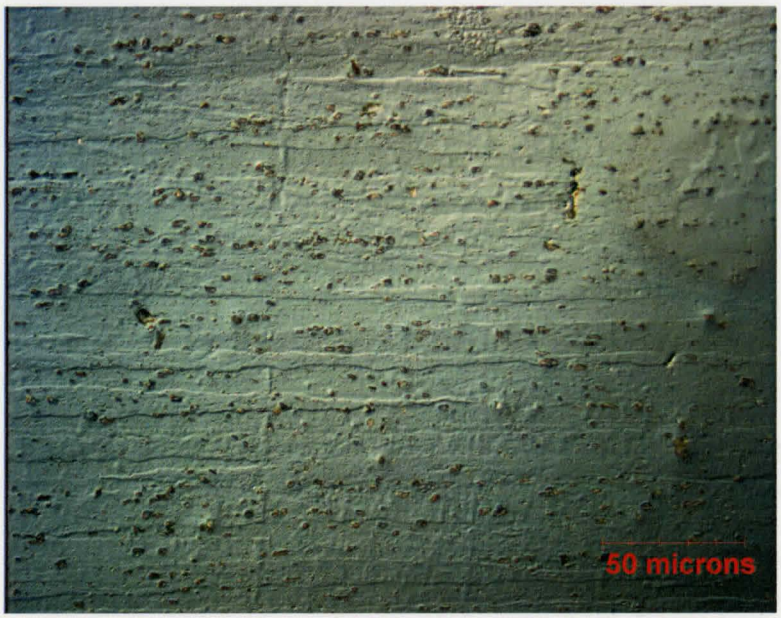

Figure 7.23:Microstructure of 75% deformed Al-Mg-Fe-Mn (I5) alloy, annealed and quenched from 175 deg.C

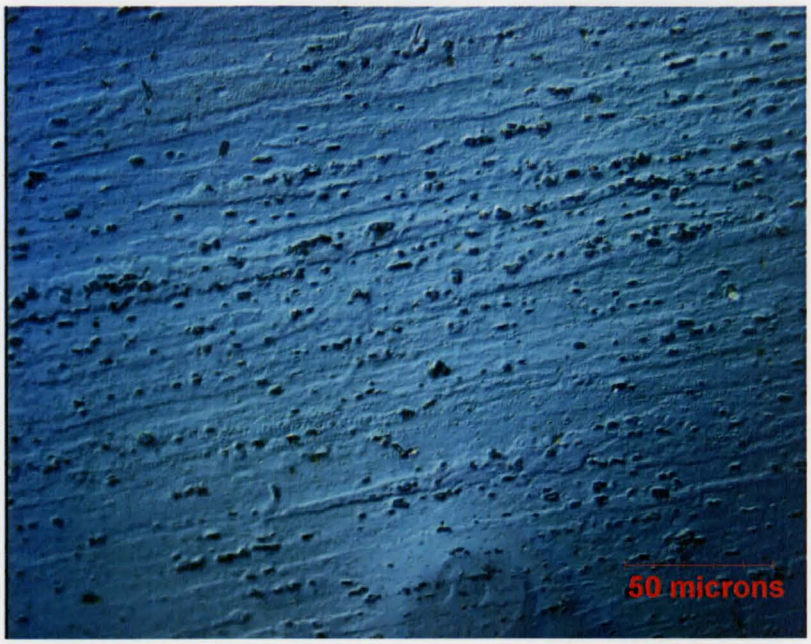

Figure 7.24:Microstructure of 75% deformed Al-Mg-Fe-Mn (I5) alloy, annealed and quenched from 212 deg.C

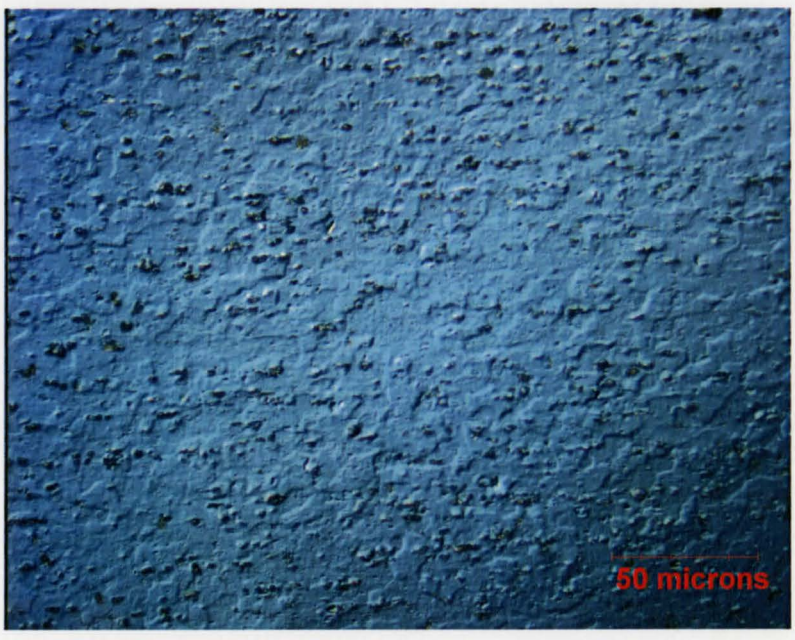

Figure 7.25:Microstructure of 75% deformed Al-Mg-Fe-Mn (I5) alloy, annealed and quenched from 225 deg.C

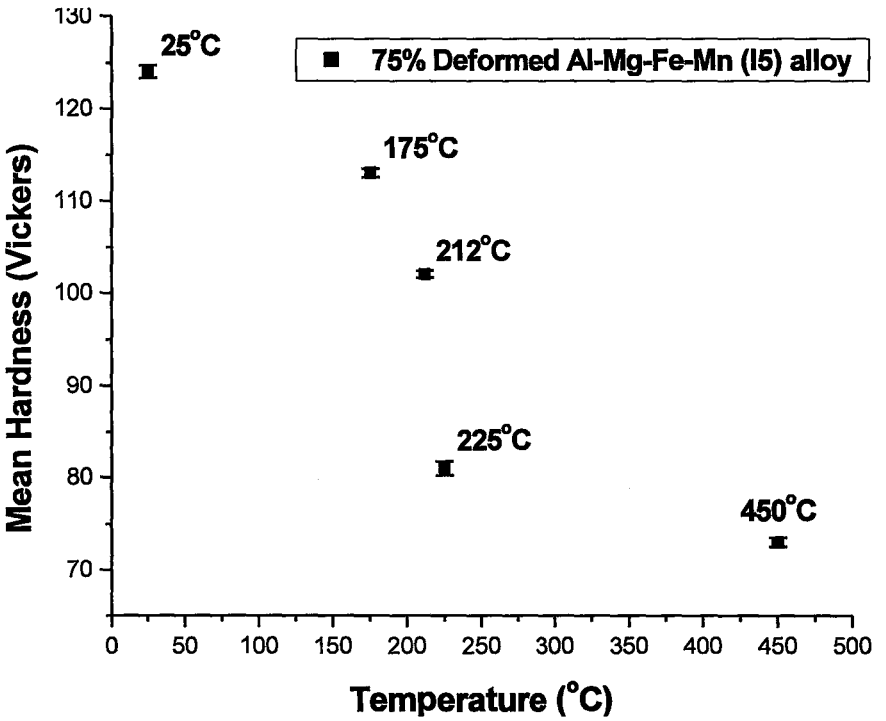

Figure 7.26: Micro-hardness measurements as a function of temperature for 75% deformed Al-Mg-Fe-Mn (I5) alloy, mean of 50 measurements for each sample

An analysis of optical micrographs shows that there is no appreciable recrystallization observed at 175°C. However, there is a very small extent of visible partial recrystallization in the micrograph pertaining to 212°C, where significant recrystallization was predicted based on resistivity measurements. Almost complete recrystallization was observed at 225°C. Therefore, it can be stated without any ambiguity that onset of recrystallization exists at some temperature below 212°C whereas recrystallization is almost complete at around 225°C. These observations were verified by hardness measurements.

Figure 7.26 shows the results obtained from micro-hardness measurements. It was noticed that there is a significant decrease in the hardness between 175°C and 212°C

whereas a sudden and sharp decrease in hardness was observed between 212°C and 225°C. This sudden and sharp decrease indicates that a significant amount of deformed structure is undergoing transformation. These observations also indicate that point of onset of recrystallization exists between 175°C and 212°C. Further analysis of hardness measurements shows that there is no significant difference in the hardness for fully recrystallized sample and sample pertaining to 225°C. This observation confirms that 225°C is the point of completion of recrystallization.

Therefore it could be confidently concluded from the results obtained so far that onset of recrystallization is occurring before 212°C i.e. $T_{beg}^{75}(I5) \leq 212^{o}C$ whereas almost complete recrystallized state is achieved at around is completed at around 225°C i.e. $T_{end}^{75}(I5) \approx 225^{o}C$.

7.5: Discussion

This section is devoted to the discussion on the results obtained for Al-3%Mg (I2) and Al-Mg-Fe-Mn (I5) alloys. Let us first discuss the results obtained for Al-3%Mg alloy. It has been already proved that results obtained from electrical resistivity measurements; micro-hardness measurements and optical metallography are self-consistent and lead to the same conclusions. The results obtained from experimental work are summarized in Table 7.1.

Table 7.1: Summery of the results obtained from experimental work

Alloy	Degree of Deformation	Onset of Recrystallization (T_{beg})	Completion of Recrystallization (T_{end})	Rate of Reaction $\left(\frac{df}{dt}\right)$
Al-3%Mg (I2)	75%	$\leq 225^{o}C$	$\geq 300^{o}C$	$\left(\frac{df}{dt}\right)_{I2}^{75} < \left(\frac{df}{dt}\right)_{I2}^{95}$
	95%	$\leq 220^{o}C$	$\geq 260^{o}C$	
Al-Mg-Fe-Mn (I5)	75%	$\leq 212^{o}C$	$\geq 225^{o}C$	$\left(\frac{df}{dt}\right)_{I5}^{75} \approx \left(\frac{df}{dt}\right)_{I5}^{95}$
	95%	$\leq 206^{o}C$	$\geq 225^{o}C$	

A summery of results, as shown in Table 7.1, indicates that the temperature of onset of recrystallization decreases with increase in degree of deformation for both the alloys (i.e. Al-3%Mg and Al-Mg-Fe-Mn). In addition, it was also observed that the positions of T_{beg} and T_{end} are shifted to lower temperatures for Al-Mg-Fe-Mn alloy as compared to Al-3%Mg alloy for the same level of deformation. Therefore, it can be

concluded that additions of alloying elements such as Fe and Mn essentially lower down the temperature of onset and completion of recrystallization. These results lead to the conclusion that the presence of second phase particles is indeed aiding the recrystallization process.

It was possible to make a qualitative assessment of the rate of reaction based on these results. It provided an opportunity to comment on the kinetics of recrystallization. These estimations of the kinetics of recrystallization are based on the comparison of estimated temperature range of occurrence of recrystallization i.e. span between T_{beg} and T_{end} (Table 7.1) and hardness measurements (Figure 7.27 and Figure 7.28). In the case of Al-3%Mg alloy, the kinetics of recrystallization was estimated much faster for 95% deformation level as compared to 75% deformation level. For the Al-Mg-Fe-Mn alloy, the kinetics of recrystallization was estimated slightly faster for 95% deformation level as compared 75% deformations. However, this difference is so small that the kinetics can not be considered drastically different.

A comparison of the recrystallization kinetics for the two alloys is essential for revealing the effect of alloying additions, such as Fe and Mn, on the recrystallization behavior of Al-Mg alloys. It was deduced that the kinetics of recrystallization is much faster in the Al-Mg-Fe-Mn alloy as compared to the Al-%3Mg alloy for the same level of deformations. Therefore, it can be concluded that Fe and Mn additions are resulting in the faster recrystallization kinetics. This effect can be explained by the fact that these additions are resulting in the formation of large number of second phase particles, which are eventually aiding the recrystallization kinetics by Particle Stimulated Nucleation

(PSN). A complete comparison of the recrystallization kinetics can be represented by the following expression:

$$\left(\frac{df}{dt}\right)_{I5}^{95} \approx \left(\frac{df}{dt}\right)_{I5}^{75} > \left(\frac{df}{dt}\right)_{I2}^{95} > \left(\frac{df}{dt}\right)_{I2}^{75} \tag{7.1}$$

An explanation of the trends of these results can be found by invoking the concept of stored energy due to plastic deformation, which provides necessary driving force for recrystallization at elevated temperatures. Since amount of stored energy is dependent on the several factors including degree of deformation, chemistry of alloys and mode of deformation. Therefore, variations in recrystallization behavior can be attributed to the variations in these factors. It is a well-known fact that increasing degrees of deformation result in generation of increasing number of dislocations, which provide the driving force for recrystallization. However, retention of these generated dislocations defines the stored energy and driving force for recrystallization rather than the generation of dislocations itself. The dislocation retention power of an alloy is usually increased by alloying additions, as is the case of Al-Mg alloys.

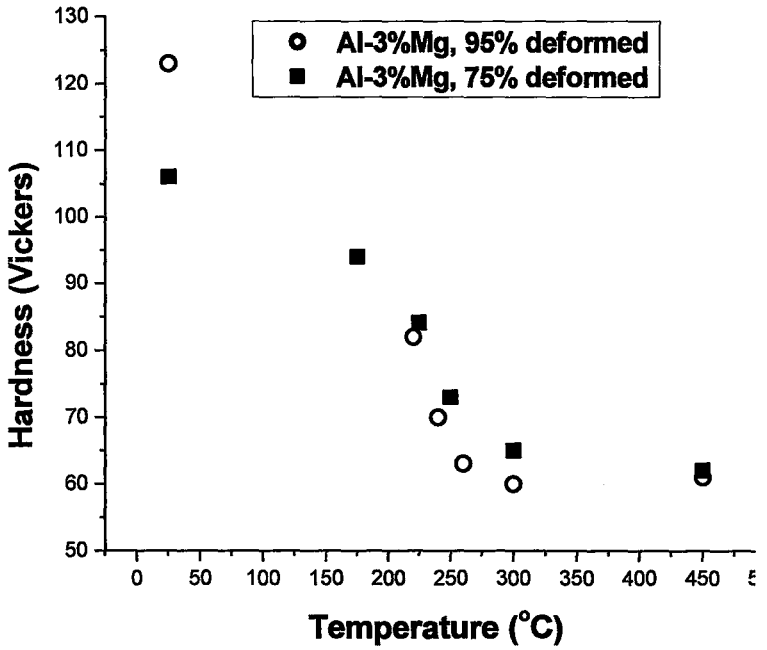

Figure 7.27: Comparison of hardness variation during annealing for two samples of Al-3%Mg with different degree of deformation

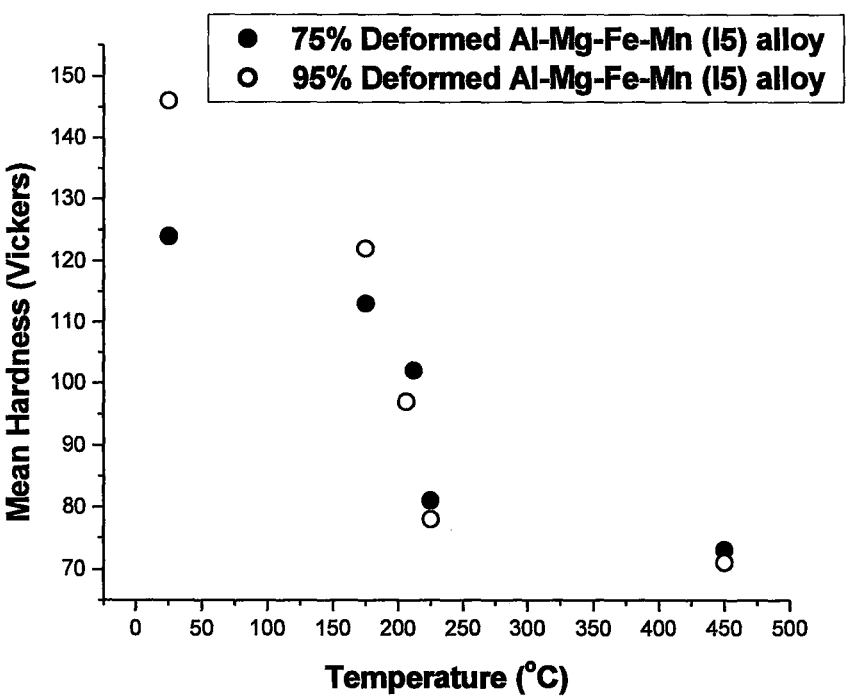

Figure 7.28: Comparison of hardness variation during annealing for two samples of Al-Mg-Fe-Mn (I5) alloy with different degree of deformation

In order to support our argument regarding higher driving force because of high stored energy due to higher amount of retained dislocation, mean micro-hardness values as a function of degree of deformation have been compared as shown in Figure 7.29. It can be seen in Figure 7.29 that mean hardness values are increasing with increasing degree of deformation for both I2 and I5 alloys. If mean hardness values can be related to the total stored energy, it can be asserted that total stored energy is increasing with increasing degree of deformation resulting in higher driving force for recrystallization. Further analysis of the mean hardness values, as shown in Figure 7.29, indicate that the micro-hardness of Al-3%Mg alloy is increasing with the alloying additions of Fe and Mn for the same level of deformation. Therefore, the stored energy is increased with increasing amount of alloying additions (Fe and Mn) indicating that the driving force for recrystallization will be higher in Al-Mg-Fe-Mn alloys as compared to Al-3%Mg for same level of deformation.

One interesting point to note in Figure 7.29 is the relative hardness values of 95% deformed Al-3%Mg and 75% deformed Al-Mg-Fe-Mn. It was found that mean micro-hardness values for these two samples are almost equal. It indicates that amount of stored energy due to plastic deformation is almost equal in these two samples meaning almost same driving force for the two alloys with different deformed conditions. A very important, yet simple, conclusion can be drawn from these observations. It can be now confidently stated that the presence of second phase particles enhances the ability of materials to retain more amount of dislocations during deformation. Therefore, increasing amount of stored energy due to higher degree of deformation and alloying additions

result in greater driving force available for the accelerating the kinetics of recrystallization. This explains the acceleration of recrystallization kinetics due to increasing degree of deformation and alloying additions.

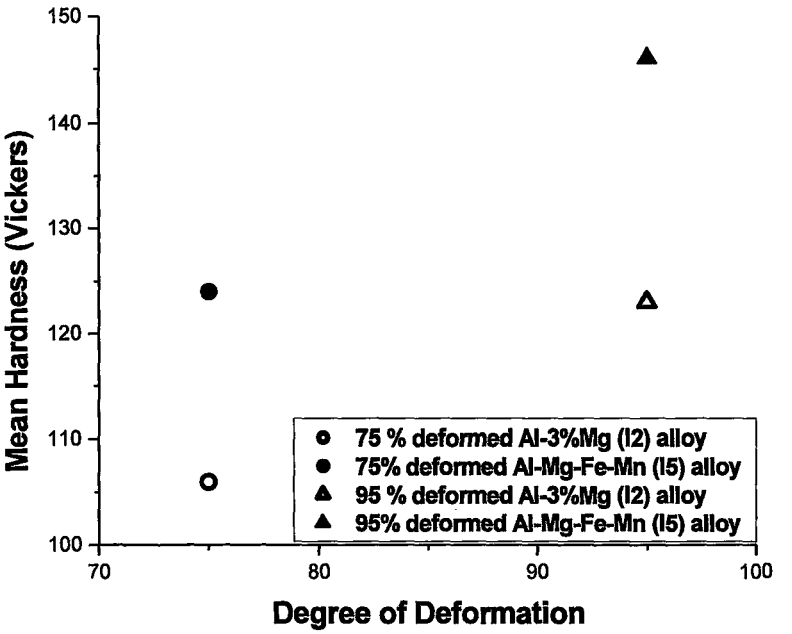

Figure 7.29: Variation of hardness values as function of degree of deformation for I2 and I5 alloys

Chapter 8: Conclusions

1. A new method, based on *in-situ* electrical resistivity measurements, has been originated and employed for characterization of recrystallization. This method has proved to be sensitive, reliable, accurate and efficient.
2. A novel method of isogeometric approximation by cubic splines has been developed. This method is able to reveal the elusive effects of recrystallization from the *in-situ* measurements of electrical resistivity, which has linear dependency on temperature.
3. A data filtering software was developed by implementing a spline based data smoothing and robust numerical differentiation procedure. The codes of data filtering program were written in Fortran.
4. In order to separate precipitation and recrystallization, a new annealing cycle was proposed through thermodynamic modeling.
5. The onset and extent of recrystallization seen in resistivity measurement experiments were confirmed by optical metallography and micro-hardness measurements.
6. With increasing degree of deformation, onset of recrystallization is shifted to the lower temperature regime.
7. For the same degree of deformation, onset of recrystallization occurs at lower temperatures for Al-Mg-Fe-Mn alloy as compared to Al-3%Mg. It shows that alloying additions, such as Fe and Mn, decrease the onset temperature.

8. Increasing degree of deformation and alloying additions (Fe and Mn) accelerate the kinetics of recrystallization. The reasons behind this trend have been explained by invoking the concept of total stored energy. An evidence of the variation of stored energy with varying degree of deformation and alloying additions has been provided by hardness measurements.
9. Although a sophisticated technique of a robust numerical differentiation was employed in this work, it is still difficult to point to the exact beginning of the peak. However, the method does allow a confident detection of the peak. Its position and extent suggest a region of temperatures for additional investigations using various experimental techniques.
10. Additions of Fe and Mn were found to decrease the average recrystallized grain size.

Bibliography

Azari 2004: H.N. Azari, S.X. Girard, D.S. Wilkinson and D.J. Lloyd, Metall. and Mater. Trans A, vol. 35A, June 2004, pp. 1839-1851.

Bacroix 1995: B.Bacroix, and Z.Hu, Metall. Trans., Vol.26A (1995), p. 601.

Baczynski 1996: J.Baczynski, and J.J.Jonas, Acta Mater., Vol. 44 (1996) p.4273.

Baker and Martin 1983: I.Baker, and J.W.Martin, Metal Science 17 (1983) p.469.

Bampton et al 1982: C.C. Bampton, J.A. Wert, and M.W. Mahoney, Metall. Trans. A, Vol. 13A, Feb., 1982, pp. 193-198.

Barghout 1996: J. Y. Barghout, G. W. Lorimer, R. Pilkington and P. B. Prannell, Materials Science Forum, Vols. 217-222, 1996, pp.975-980.

Broom 1954: Broom T, "Lattice defect and the electrical resistivity", Advances in Physics, 3, No-9, (1954) pp-26.

Broom and Barrett 1953: T. Broom and C. S. Barrett, Acta metallurgica, Vol. 1, May 1953, pp. 305-309.

Burger 1995: G.B. Burger, A.K. Gupta, P.W. Jeffrey and D.J. Lloyd, Mater. Charact., 35, 23-39 (1995).

Chan and Humphreys 1984: H.M. Chan and F.J. Humphreys, Acta Metall. Vol. 32, No.2, pp.235-243, 1984.

Doherty et al 1997: R.D.Doherty, D.A.Hughes, F.J.Humphreys, J.J.Jonas, D.Juul Jensen, M.E.Kassner, W.E.King, T.R.McNelley, H.J.McQueen and A.D.Rollett, Mater. Science and Engineering A238(1997) 219-274.

Esmaeili 2000: S.Esmaeili, D.J.Lloyd, and W.J.Poole, Mater. Letters, 59(2005)575-577.

Esmaeili 2005: S.Esmaeili, D.J.Lloyd, and W.J.Poole, Mater. Sc. Forum, vols. 331-337 (2000) pp. 995-1000.

Ferry and Jones 1998: M. Ferry and D. Jones, Scripta Mater., Vol. 38, No. 2, pp. 177-183, 1998.

Gaber 1993: A. Gaber, N.Afify, A.Y.Abdel-Lateif, and M.S.Mostafa, Solid State Communications, vol.86, No. 10, pp.679-683, 1993.

Hansen and Bay 1981: N. Hansen and B.Bay, Acta Metall. Vol 29, pp. 65-77, 1981.

Higginson 2002: Higginson, R.L., MacGregor and Palmiere, Materials Science Forum, vols. 396-402 (2002) pp. 303-308.

Hirsch 1997: J. Hirsch, Mater. Sc. Forum, Vol. 242 (1997) pp. 33-50.

Hohne 2003: G. W. H. Hohne, W. F. Hemminger and H. J. Flammersheim, in "Differential Scanning Calorimetry", 2nd edition, Springer-Verlag, NY, 2003.

Humphreys 2004: F.J.Humphreys, Mater. Sci. Fourm, Vols 467-470 (2004) pp.107-116.

Humphreys 1977: F.J. Humphreys, Acta Metallurgica, Vol. 25 (1977) pp. 1323-1344.

Humphreys and Hatherly 2004: F.J. Humphreys and M. Hatherly, Recrystallization and Related Annealing Phenomena, Second Edition, Elsevier, 2004.

Inakazu 1987: Naotsugu Inakazu and Yasuyuki Kaneno, J. Japan Inst. Metals, vol. 51, No. 12 (1987) pp. 1116-1124.

Janecek 2004: Miloš Janeˇcek, Margarita Slámová, and Michal Hájek, Journal of Alloys and Compounds, 378 (2004) 316–321.

Khan 2003: Abdul Faheem Khan, Anwar Manzoor Rana and M. Iqbal Ansari, Materials and Design, 24 (2003) 151-155.

Korbel 1986: A. Korbel, J.D. Embury, M. Hatherly, P.L. Martin, and H.W. Erbsloh, Acta Metall. Mater, 1986, vol.34, p.1999.

Lindh 1993: Lindh, E., Hutchinson, and Ueyama, S., Scripta Metall.Mater Vol.29 (1993)p.347.

Maeta 1968: Hiroshi Maeta, J. Physical Soc. Japan, vol. 24, No. 4, April 1968.

Mathew 1984: E.V.Mathew, T.R.Ramchandran, K.P.Gupta and S. Das, J. of Mater. Sc. Letters,3(1984) 605-610.

Meaden 1965: George Terence Meaden, in "Resistance of Metals", Plenum Press N.Y., 1965.

Mondolfo 1976: L.F. Mondolfo, Aluminum Alloys: Structure and Properties, Butterworths, London, 1976.

Morri 1985: K. Morii, M. Mecking, and Y. Nakayama, Acta Metall. Mater., 1985, Vol. 33, p.379.

Mould and Cotterill 1967: P.R. Mould and P. Cotterill, Journal of Materials Science 2(1967) 24-1-255.

Mughrabi 1983: H. Mughrabi, Acta Metall. Mater., 1983, vol. 31, p. 1367.

Nakayama 1987: Y. Nakayama and K. Morii, Acta Metall. Mater., 1987, Vol. 35, p.1747.

Nes 1976: Erik Nes, Acta Metallurgica, vol 24, pp. 391-398 (1976).

Sanders 1989: R.E. Sanders, Jr., S.F. Baumann, and H.C. Stumpf, in "Treatise on Materials Science and Technology", vol.31, eds.Vasudevan, A.K. and Doherty, R.D., Academic Press, pp.65-105.

Sandstrom 1980: Rolf Sandstrom, Z. Metallkde, Bd. 71(1980) H 10, pp. 681-688.

Sarkar 2006: S.Sarkar, M.A.Wells and W.J.Poole, Mater. Sc. And Engg., A421 (2006) 276-285.

Schrank 1980: J. Schrank, M. Zehetbauer, W. Pfeiler and L. Trieb, Scripta Metallurgica, Vol. 14, 1980, pp. 1125-1128.

Starink 2004: M.J. Starink, International Materials Reviews, 2004, Vol. 49, No. 3-4, 191-226.

Verdier 1997: M. Verdier, I. Groma, L. Flandin, J. Lendvai, Y. Brechet and P. Guyot, Scripta Materialia, Vol. 37, No. 4, pp. 449-454, 1997.

Wang 2002: Y.J. Wang and H.S. Zurob, Appl. Phys. A 74 (suppl.), 2002, S1213-S1215.

Weiland 2004: Hasso Weiland, Materials Science Forum, Vols. 467-470 (2004) pp. 349-356.

Yang 1982: S.W.Yang and J.E.Spruill, J.Mater.Sc., 17(1982)677-690.

Zurob 2001: H.S. Zurob, Y. Brechet and G. Purdy, Acta mater., 49(2001) 4183-4190.

Zurob 2002: H.S. Zurob, C.R. Hutchinson, Y. Brechet, and G. Purdy: Acta Materialia, 50 (2002) 3075–3092.